Spring 2006

Study of propagation and detection methods of terahertz radiation for spectroscopy and imaging

Aparajita Bandyopadhyay
New Jersey Institute of Technology

ABSTRACT

STUDY OF PROPAGATION AND DETECTION METHODS OF TERAHERTZ RADIATION FOR SPECTROSCOPY AND IMAGING

by
Aparajita Bandyopadhyay

The applications of terahertz (THz, 1 THz is 10^{12} cycles per second or 300 μm in wavelength) radiation are rapidly expanding. In particular, THz imaging is emerging as a powerful technique to spatially map a wide variety of objects with spectral features which are present for many materials in THz region. Objects buried within dielectric structures can also be imaged due to the transparency of most dielectrics in this regime. Unfortunately, the image quality in such applications is inherently influenced by the scattering introduced by the sample inhomogeneities and by the presence of barriers that reduces both the transmitted power and the spatial resolution in particular frequency components. For continued development in THz radiation imaging, a comprehensive understanding of the role of these factors on THz radiation propagation and detection is vital.

This dissertation focuses on the various aspects like scattering, attenuation, frequency filtering and waveguide propagation of THz radiation and its subsequent application to a stand-off THz interferometric imager under development. Using THz Time Domain spectroscopic set-up, the effect of scattering, guided THz propagation with loss and dispersion profile of hollow-core waveguides and various filtering structures are investigated. Interferometric detection scheme and subsequent agent identification is studied in detail using extensive simulation and modeling of various imaging system parameters.

STUDY OF PROPAGATION AND DETECTION METHODS OF TERAHERTZ RADIATION FOR SPECTROSCOPY AND IMAGING

by
Aparajita Bandyopadhyay

A Dissertation
Submitted to the Faculty of
New Jersey Institute of Technology and
Rutgers, The State University of New Jersey-Newark
in Partial Fulfillment of the Requirements for the Degree of
Doctor of Philosophy in Applied Physics

Federated Physics Department

May 2006

APPROVAL PAGE

STUDY OF PROPAGATION AND DETECTION METHODS OF TERAHERTZ RADIATION FOR SPECTROSCOPY AND IMAGING

Aparajita Bandyopadhyay

Dr. John F. Federici, Dissertation Advisor — Date
Professor of Physics, NJIT, NJ

Dr. Robert B. Barat, Committee Member — Date
Professor of Chemical Engineering, NJIT, NJ

Dr. Dale E. Gary, Committee Member — Date
Professor of Physics, NJIT, NJ

Dr. James A. Harrington, Committee Member — Date
Professor of Materials Science and Engineering, Rutgers, The State University of New Jersey-New Brunswick, NJ

Dr. Richard Mendelsohn, Committee Member — Date
Professor of Chemistry, Rutgers, The State University of New Jersey-Newark, NJ

Dr. Pradumnya K. Swain, Committee Member — Date
Technical Manager, Sarnoff Imaging Systems, Princeton, NJ

BIOGRAPHICAL SKETCH

Author: Aparajita Bandyopadhyay

Degree: Doctor of Philosophy

Date: May 2006

Undergraduate and Graduate Education:

- Doctor of Philosophy in Applied Physics,
  New Jersey Institute of Technology, Newark, NJ, 2006

- Master of Science in Physics,
  Indian Institute of Technology Delhi, New Delhi, India, 2002

- Bachelor of Science in Physics,
  Indira Gandhi National Open University, Delhi, India, 2000

Major: Applied Physics

Presentations and Publications:

A. Bandyopadhyay, A. Sengupta, A. M. Sinyukov, R. B. Barat, D. E. Gary, Z. H. Michalopoulou and J. F. Federici,
"Artificial neural network analysis in interferometric THz imaging for detection of lethal agents," *Int. J. Infrared Millimeter Waves*, 2006 (accepted).

A. M. Sinyukov, A. Bandyopadhyay, A. Sengupta, R. B. Barat, D. E. Gary, Z. H. Michalopoulou, D. A. Zimdars and J. F. Federici,
"Terahertz interferometric and synthetic aperture imaging," *Proc. SPIE* **6212**, 2006 (in press).

A. Bandyopadhyay, A. M. Sinyukov, A. Sengupta, R. B. Barat, D. E. Gary, Z. H. Michalopoulou and J. F. Federici,
"Interferometric terahertz imaging for detection of lethal agents using artificial neural network analyses," *Proceedings of the IEEE Sarnoff Symposium*, Princeton, NJ, 28 March 2006 (in press).

A. Sengupta, A. Bandyopadhyay, J. F. Federici, H. Grebel and D. Pham,
"A non contact characterization technique of the defect states of high k dielectrics using THz radiation," *Proceedings of the IEEE Sarnoff Symposium*, Princeton, NJ, 28 March 2006 (in press).

A. Bandyopadhyay, A. Sengupta, J. F. Federici, V. Johnson and J. A. Harrington, "Terahertz time domain spectroscopy of hollow polycarbonate metal waveguides," *American Physical Society March Meeting*, N17. 00010; Baltimore, MD, 15 March 2006.

A. Sengupta, A. Bandyopadhyay, H. Altan, J. F. Federici, H. Grebel and D. Pham, "Terahertz spectroscopy as a non contact estimation technique of defect states in high dielectric constant materials," *American Physical Society March Meeting*, G 17.00004; Baltimore, MD, 14 March 2006.

A. Bandyopadhyay, A. Sengupta, R. B. Barat, D. E. Gary and J. F. Federici, "Grain Size Dependent Scattering Studies of Common Materials using terahertz time domain techniques," *Proc. SPIE, THz and GHz Electronics and Photonics V*, Vol. **6120**, 61200A, 2006.

A. Bandyopadhyay, A. Sengupta, V. Johnson, J.A. Harrington and J.F. Federici, "Characterization of Hollow Polycarbonate Metal waveguides using terahertz time domain spectroscopy," *Proc. SPIE, THz and GHz Electronics and Photonics V*, Vol. **6120**, 61200B, 2006.

A. Sengupta, A. Bandyopadhyay, R. B. Barat, D. E. Gary and J. F. Federici, "THz Reflection Spectroscopy of Composition C-4 and its detection through interferometric imaging," *Proc. SPIE, THz and GHz Electronics and Photonics V*, Vol. **6120**, 61200H, 2006.

A. Bandyopadhyay, A. Stepanov, B. Schulkin, M. D. Federici, A. Sengupta, J. F. Federici, D. E. Gary, R. B. Barat, Z. Michalopoulou and D. Zimdars, "THz interferometric and synthetic aperture imaging," *J. Opt. Soc. Am. A*, 2006 (in press).

A. Bandyopadhyay, A.Sengupta, R. B. Barat, D. E. Gary, Z. H. Michalopoulou and J. F. Federici, "Application of THz Imaging in Security Screening," *89th OSA Annual Meeting, Frontiers in Optics*, JWA 1, Tucson, AZ, 19 October 2005.

A. Sengupta, H. Altan, A. Bandyopadhyay, J. F. Federici, H. Grebel and D. Pham, "Investigation of Defect States of HfO_2 and SiO_2 on p-type Silicon using THz Spectroscopy," *89th OSA Annual Meeting, Frontiers in Optics*, FWF1, Tucson, AZ, 19 October 2005.

A. Sengupta, A. Bandyopadhyay, J. F. Federici and N. M. Ravindra, "Far-infrared Studies of Silicon related Structures using THz Spectroscopy", *The Physics and Materials Challenges for Integrated Optics: A step in the future for Photonics Devices symposium of MS&T 05*, pp 39, Pittsburgh, PA, 26 September 2005.

A. Sengupta, A. Bandyopadhyay, R. B. Barat, D. E. Gary and J. F. Federici, "Study of Morphological Effects on THz Spectra using Ammonium Nitrate," *OSA Topical Meeting, Optical THz Science and Technology*, ME6, Orlando, FL, 14 March 2005.

A. Sengupta, A. Bandyopadhyay, J. F. Federici and N. M. Ravindra, "Optical properties of silicon in the terahertz regime," *Solid State Electronics*, 2006 (under review).

A. Sengupta, A. Bandyopadhyay, R. B. Barat, D. E. Gary and J. F. Federici, "Spectral identification of granular solids in the THz range," under preparation.

To all those thirsty devotees pursuing her beauty in so many ways

Where there is great doubt, there will be great awakening;
Small doubt, small awakening and with no doubt, there is no awakening.

– Zen proverb

ACKNOWLEDGMENT

At each stage of my quest, the circle of people to whom I am indebted for sharing ideas and thoughts and offering suggestions, comments and encouragement has widened so much that I might forget to thank a great number of people without whom this doctoral dissertation work would not have been possible. I gratefully acknowledge the help of all those people and my deepest regard goes to all of them.

I particularly want to thank my dissertation advisor, Dr John Federici for initiating within me a lasting interest in the field of THz spectroscopy and imaging and for his unfailing support, encouragement and guidance at every step of my studies which finally led to this dissertation. Likewise, my heartfelt thank goes to the distinguished committee members Dr. Robert Barat, Dr. Dale Gary, Dr. James Harrington, Dr. Richard Mendelsohn and Dr. Pradyumna Swain who reached out in every possible ways to support this endeavor of mine by providing critical comments and invaluable suggestions. I am also thankful for all the enlightening discussions that I was fortunate to have with Dr. N. M. Ravindra, Dr. Z. H. Michalopoulou, Dr. D. E. Murnick, Dr. M. Salvermoser, Dr. G. A. Thomas, Dr. H. C. Lim and Dr. A. M. Sinyukov in the course of this work.

I also gratefully acknowledge the funding agencies (TSWG, Dept. of Homeland Security and Army Research Office) whose generous grants facilitated this work. Special thanks go to the GSA-NJIT, OSA and SPIE for covering the expenses to various conferences which helped immensely in widening my horizon.

Lastly an attempt to thank my parents and my family is simply beyond me; but a very special note of thanks would go to my long time friend, collaborator and my partner in life with whom I share every turn of this journey with so many exciting, and occasionally explosive moments.

TABLE OF CONTENTS

TABLE OF CONTENTS
(Continued)

Chapter **Page**

TABLE OF CONTENTS
(Continued)

Chapter **Page**

LIST OF FIGURES

LIST OF FIGURES
(Continued)

LIST OF FIGURES
(Continued)

CHAPTER 1

INTRODUCTION

1.1 Background

The Terahertz (THz where 1 THz = 10^{12} cycles/sec and 300 μm in wavelength) frequency range of the electromagnetic spectrum has long been of very limited interest to scientists and engineers, primarily due to lack of any efficient and affordable source and detector. Though sustained research was focused to bridge this "THz gap" between microelectronics and photonics for a long time[1, 2, 3, 4]; the real breakthrough came only in late 1980s with the advent of subpicosecond photoconductive dipole antennas[5, 6]. It brought about the largest wave of THz activities in terms of implementing the techniques of THz time-domain spectroscopy (THz-TDS)[7, 8, 9, 10] and "T-rays" imaging[11, 12] using ultrashort synchronized THz-pulsed gating.

The use of THz radiation, especially in the area of spectroscopy, has become very important as the scientists could carry out time-resolved far-infrared studies of materials with subpicosecond temporal resolution[13, 14]. Furthermore, many biological[15], organic[16] and inorganic[17] molecules have vibrational and/or rotational spectra that lie in the THz frequency range, with signatures resulting from intra-molecular and inter-molecular interactions. Coupled with that, THz wavelengths are short enough to enable submillimeter imaging while long enough to penetrate many non-metallic common materials, such as clothing, plastic, ceramic, wood etc., allowing concealed objects to be imaged. These reasons have made the THz science a potential candidate for commercial exploitation in a number of applications.

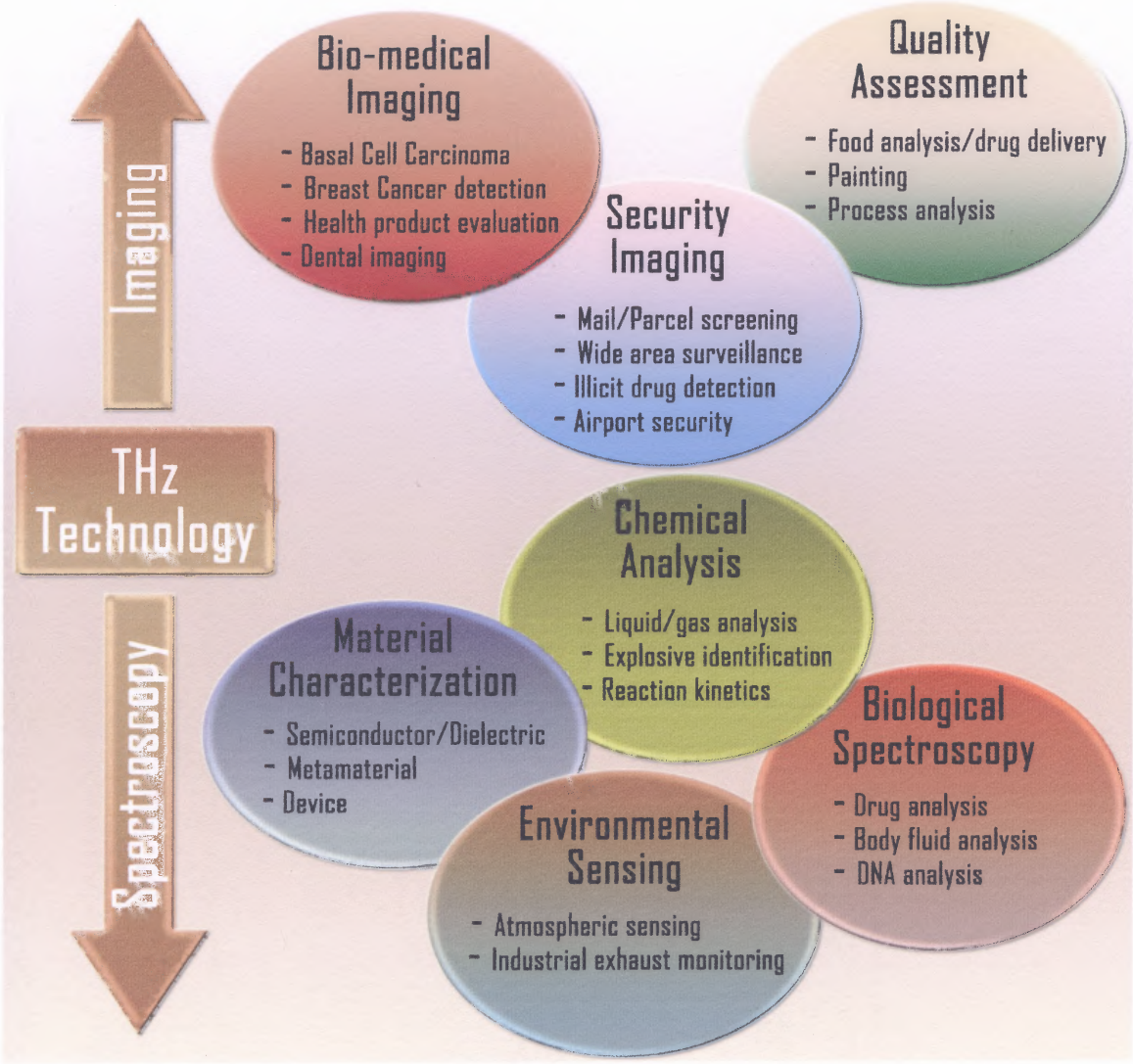

Figure 1.1 THz technology: Integrating spectroscopy and imaging techniques.

In past few years, THz science has initiated a steady growth of research efforts in a range of applications like bio-medical imaging and diagnostics, nondestructive evaluation of material parameters, chemical and gas sensing, remote sensing and security screening as illustrated in Figure 1.1. Currently, THz technology is poised to make great impact in several key sectors combining the spectral specificity with the imaging aspect of THz range. However, one crucial restraining factor that is yet to be overcome is the fact that there is no cheap, powerful and portable THz source and low cost, sensitive THz

detector existing and therefore, strong research efforts are directed towards fabricated cheap, solid-state THz emitters and detectors.

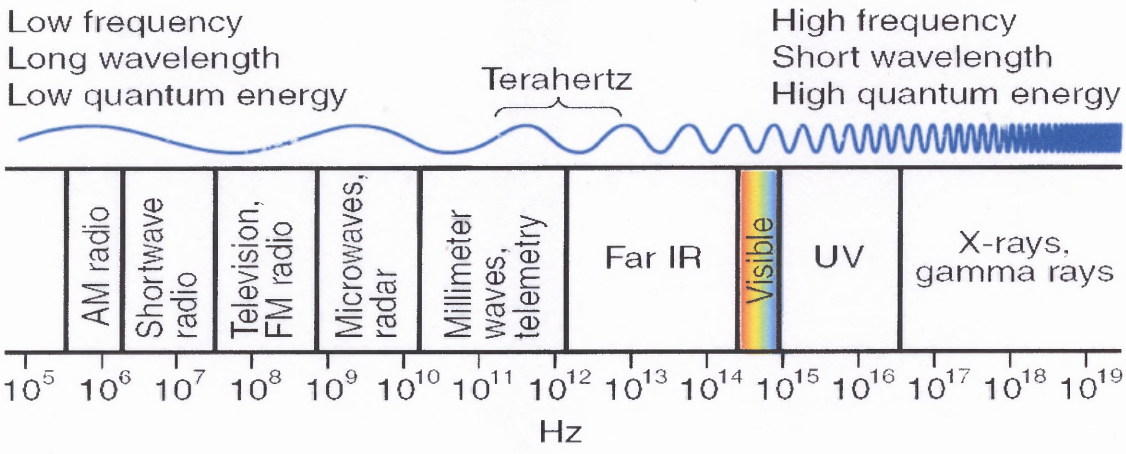

Figure 1.2 Electromagnetic spectrum and THz frequency range.
(Source: M.J. Fitch and R. Osiander, Johns Hopkins APL Technical Digest, 25, 348 (2004))

Presently, the THz regime is broadly taken to be the entire range from 0.1 to 10 THz. However, more strictly, the THz range has been defined to be the submillimeter-wavelengths between approximately 1 mm (300 GHz) and 100 μm (3 THz), which is located exactly between the traditional RF (radio frequency) microwave and the IR (infra red) domains as shown in Figure 1.2. Detailed account of different stages of the development and the current progress of THz science and technology in various fields of applications can be found in many good review articles[18, 19, 20, 21, 22] and books by various authors[23, 24, 25, 26].

1.2 Motivation

Over the past several years THz technology has become a primary tool for researchers across different fields of science and yet some key aspects of this multidisciplinary subject remain relatively unexplored. Specifically the description and understanding of

the propagation of THz pulses in optical systems and through material media are still very limited. Though considerable efforts have been directed to measure and calculate the distribution of THz field at or near THz emitting structure[27], focusing element[28] or aperture[29]; the overall propagation criteria of THz radiation through an assembly of optical and material elements are still essentially approximated. In particular, THz scattering by material media and surfaces, guided THz propagation, THz frequency filtering, THz near field imaging and other characteristics of interactions between THz radiation and physical systems have continued to be some of the pertinent questions for researchers at present.

This limited understanding is especially disadvantageous in many areas of THz application. In many situations, one needs to tailor selected propagation characteristics of THz radiation such as the attenuation, dispersion, frequency content, pulse shape and others to meet certain requirements associated with the particular application. Moreover, the material and device parameters directly induce changes in both the amplitude and phase of the propagated THz pulse which can be simultaneously measured by THz detectors. Therefore, one may exploit these material and device considerations to realize better operational systems in terms of accuracy, efficiency and cost, either in THz spectroscopy or THz imaging. However, for accurate identification and understanding of these parameters, one has to have a complete grasp of both THz propagation and detection mechanisms.

In the present study, to resolve some of the significant aspects related to THz propagation and detection methods with a specific goal of improving the technique of stand-off THz security imaging[30], in depth investigations of the following issues have been made:

- Determination of grain size dependent scattering contribution on the extinction spectra and how it affects the identification criteria of non-absorbing granular solids in THz range. The conclusion of this study will affect the detection mode of a THz security imaging system in terms of its sensitivity and precision.

- Comparison of free-space and guided propagation of THz radiation illustrating the particular case of a copper coated flexible, hollow polycarbonate THz waveguide to measure the loss and dispersion profile using broadband THz pulse source. This study would determine whether guided THz propagation is a viable option for low loss THz transmission in stand-off THz imaging along with many other applications.

- Design of a wavelength-scalable, band reject THz frequency filter in reflection mode using multilayer structure. THz frequency filtering is a necessary component in various THz applications, including THz security imager, as it would offer a possibility of reducing the signal or noise in certain band of frequencies (such as background thermal THz noise) and thus improving the overall signal to noise of the system.

- With respect to a stand-off interferometric THz imager, different considerations such as detector configuration, effects of boundaries, effects of near-field imaging and presence of barrier are examined to evaluate their respective and collective impact on agent identification. This study is a direct attempt to make an estimation of the measure of the performance of the THz imager under development.

1.3 Overview of Thesis

This thesis work is divided into seven main chapters. Summarized descriptions of the following chapters are provided below:

- **Chapter 2**: A review of the a) THz time domain spectroscopic (THz-TDS) technique used for scattering studies, waveguide characterization and b) interferometric THz imaging set-up with CW generation and detection techniques used for stand-off THz security imaging, have been provided. The ultrafast optical methodologies involving femtosecond lasers to generate terahertz radiation using photoconductive antennae has been described in detail.

- **Chapter 3:** Effects of scattering on THz spectra of granular solids are studied using common materials such as flour, salt, sugar and chalk in the frequency range of 0.2 to 1.2 THz. Separation of intrinsic material absorption from scattering losses using Mie Scattering theory shows that the frequency dependence of extinction in weakly absorbing materials is predominantly particle size dependent in lower THz frequencies and therefore unique identification of a granular solids cannot be made based on their rising trend of THz extinction spectra.

- **Chapter 4:** Copper coated flexible, hollow polycarbonate THz waveguides are studied using THz-TDS technique and the loss and dispersion profile of the same are determined over the frequency range of 0.2 to 1.2 THz. Comparison of free-space and guided propagation of THz radiation are also made to investigate the prospect of using THz guiding structures in various applications.

- **Chapter 5:** A design of a wavelength-scalable, band reject THz frequency filter in reflection mode using multilayer structure has been proposed. Physical parameters like refractive indices, attenuations, thicknesses of the layers are optimized for specific applications.

- **Chapter 6:** To complement experimental testing of THz interferometric imaging set-up, extensive simulations yield spatial composite images of agents at different frequencies based on the spectral data obtained with a THz Time Domain Spectroscopic (THz-TDS) system. Different criteria such as detector configuration, effects of boundaries, effects of near-field imaging and presence of barrier on image formation and subsequent agent identification using Artificial Neural Network (ANN) analysis approach have been examined.

- **Chapter 7:** Conclusion and future scope of the studies conducted are provided.

CHAPTER 2

REVIEW OF TERAHERTZ TECHNIQUES

2.1 Introduction

For past 20 years, THz science has chronicled a steady growth in various methods and techniques; some are quite typical to this new discipline and being utilized to realize the goals of myriad THz applications. However, in spite of the tremendous advent in this field, the developments have not spun-off any widespread industrial undertakings and one of the primary reasons for this impediment lies in the fact that the most of the advanced THz systems remain expensive and bulky. Though turn-key THz systems are now commercially available for THz spectroscopy and imaging, these are still very expensive (in excess of $250,000)[31]. Moreover, the conversion efficiency of optical-to-THz power in optoelectronic THz sources is still very low (not exceeding 10^{-4}), imposing regular and strict alignment requirements of the complex spectroscopic set-up and making large-area imaging a very time-consuming process.

Essentially, THz technology heavily depends on certain THz techniques, all of which are not general, but rather better suited for specific applications[32, 33, 34]. Two of these techniques namely the THz-Time Domain Spectroscopic (THz-TDS) technique for spectroscopic application and Continuous Wave (CW) THz imaging technique for imaging application will be discussed in detail in the present chapter. Both of these techniques are based on optoelectronic generation and detection mechanisms which are described in detail in the following sections. To understand these two THz techniques properly, a clear perspective of presently available THz sources and detectors is required.

2.2 Terahertz Sources and Detectors

Different existing approaches of generation and detection of THz radiation can be broadly classified into two types: that is, the broadband (or pulsed) THz emission and detection method and the continuous wave (CW) THz emission and detection. The former is more important for either broadband spectroscopic type of applications or proximity (< 3m) imaging[35], while the later one is more suitable for high resolution spectroscopy[36] (with resolution ≤ 1 MHz) or stand-off (> 3 m) imaging[37] purposes.

2.2.1 THz Generation

The broadband and CW generation of THz radiation can further be classified from a more fundamental perspective, based on the physical processes involved in such generation methods in the following major groups which are electronic, optical and optoelectronic THz generation.

2.2.1.1 Electronic THz Generation. This approach has been extended from the microwave side of the EM spectra where essentially the radiation is generated due to the movements of electronic carriers under the influence of strong electric and/or magnetic fields externally established in specific amplifying or oscillatory structures. The operational efficiency of these THz sources therefore essentially depends on the speed of the carriers and the electrical parameters of the particular device. Some of the most important and interesting electronic structures commissioned for THz generation are monolithic nonlinear transmission lines (NLTL's) as ultrafast voltage step generators[38, 39], submicron scaled heterojunction bipolar transistors (HBTs)[40, 41] which are broadband THz sources using the concept of high-order frequency multiplication and microwave

oscillators (for example, backward wave oscillator[42], Gunn diode oscillator[43]) which are used for producing narrowband tunable CW THz radiation using low-order frequency multiplication[44]. The advantages of this approach lie in the relative simplicity[45] and the robustness of these electronic structures. However, it is difficult to fabricate electronic devices that operate above a few hundred GHz of frequencies, because the optimal performance of these devices rely on very short carrier transit times in the active regions which effectively reduces the device area to lower device capacitance and consequently the power delivered by these devices in THz regime is typically small. The highest frequency generated with these kind sources is 1.9 THz with an output power of 20 μW[46]. Nevertheless, some key areas of THz applications use this approach of THz generation[47, 48, 49].

2.2.1.2 Optical THz Generation. Similar to microwave region, a few important mechanisms of optical energy emission has extended from the optical regime to THz region. These generation processes are fundamentally dominated either by direct optical transitions between energy subbands in semiconductor structures (such as in p-germanium[50], n-silicon lasers[51] and quantum cascade lasers[52, 53]) or by exciting the vibrational-rotational lines of molecular gases[54, 55] (such as methanol, CH_3OH) through optically pumped far infrared laser to obtain narrowband continuous wave operation of these sources. Using GaAs/AlGaAs quantum-well heterostructures, laser operation in the frequency range of 1.9–4.8 THz at temperatures of up to ~140 K, and high output power of up to 90 mW have been achieved[56]. For broadband production of THz radiation, the processes involved are mainly optical rectification by directly exploiting the material properties of suitable crystalline species[57, 58, 59] (which include among others $LiNbO_3$,

$LaTiO_3$; zinc-blende semiconductors (GaAs, ZnTe, CdTe, InP) or organic crystals (DAST)) or synchronous radiation from relativistic electrons moving under the influence of high magnetic field (free electron laser)[60]. Some of these approaches of submillimeter wave generation predates the advent of modern THz technology[61, 62] and yet most of these optical methods either require massive and expensive apparatus (like free electron laser or molecular gas laser) or involve cryogenic operating conditions (p-Ge laser, quantum cascade laser) and therefore their use is somewhat limited in many application areas. However, electro-optic generation of THz has gained a lot of interest because of extensive bandwidth comprising higher frequencies[63, 64, 65] .

2.2.1.3 Optoelectronic THz Generation. Combining the optical and electronic techniques, the optoelectronic THz generation exploits the electronic response of a material to optical excitations; for example, photoconductivity in semi-insulating semiconductors[66] or different excitation mechanisms of coherent phonons in other condensed media[67]. Incidentally the inception of the modern THz science was made with optoelectronic THz generation[68, 69] with photoconductive generation to produce subpicosecond THz pulse which has driven intense research activities since then to explore different photoconductive antennae structures[70, 71, 72, 73] and photoconductive materials[74, 75, 76, 77] in order to achieve higher power and broader bandwidth. Parallel to this effort, alternative approaches using surface fields[78, 79, 80] were also pursued to produce broadband THz radiation. Moreover, narrow spectral bandwidth continuous wave THz radiation sources with frequency tunability are some of the most recent advancements in the THz optoelectronic sources with the use of photomixing mechanisms in materials with nonlinear response[81, 82, 83]. At the same time, parametric oscillators are also used to

generate continuous tunable CW THz frequencies by parametric light scattering from the stimulated polariton scattering in nonlinear crystals[84, 85]. However, the one of the main drawbacks of optoelectronic terahertz sources, like photomixers, is their low output coming from their low optical-to-electrical conversion efficiency[86].

2.2.2 THz Detection

Unlike THz generation, the classification of THz detection in terms of physical processes is not that insightful. The detection mechanism should be classified in terms of the measurable quantity, that is, either THz field amplitude or THz power. The first mechanism is evidently a phase-sensitive detection method where both phase and amplitude can be detected simultaneously; while the later one measures the total power.

2.2.2.1 THz Amplitude Detection. To measure the THz electric field of either the broadband (or pulse) or continuous wave (CW) THz source, coherent gated detection mechanism is employed. For pulsed coherent THz radiation, either photoconductive sampling[87] or free-space electro optic sampling[88] are used; while for CW THz radiation, either homodyne[89] or heterodyne detection[48] methods are used, principally employing the photoconductive sampling.

2.2.2.2 THz Power Detection. The THz power detection is achieved using thermal detectors. THz radiation incident on a thermal detector is absorbed by some form of material which changes its physical properties such as electric conductivity (like bolometers[90]), volume (like Golay detector) or dielectric nature (like pyroelectric sensors[15]) with temperature. Common characteristics of these thermal detectors are their overall broadband sensitivity and comparatively long response times but with the

advantage of very small Noise Equivalent Power (NEP). NEP is the signal input power which is needed to generate a output signal at the detector as big as the output signal generated by the detector noise; small values of NEP generally signifies better detection because of very small inherent noise of the detector. The chart below in Figure 2.1 illustrates various forms of THz sources and detectors currently available.

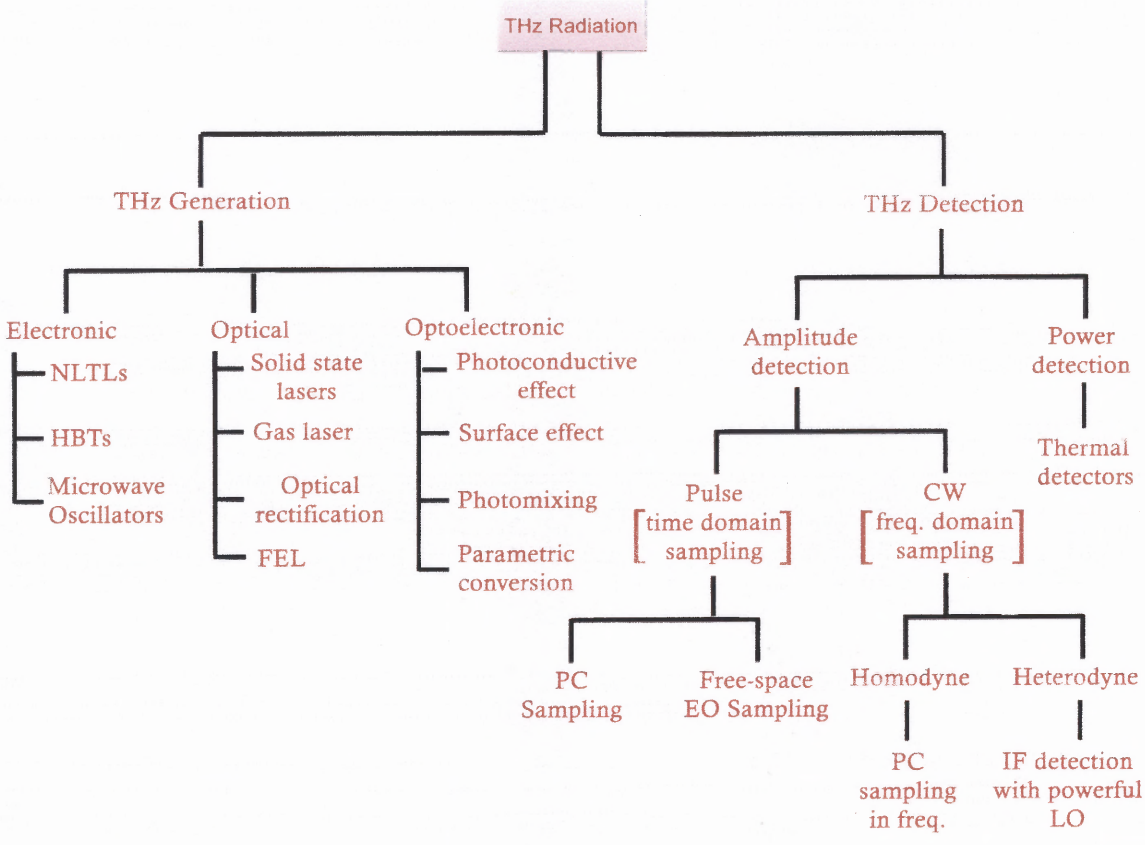

Figure 2.1 Different sources and detectors of THz radiation.

2.3 THz Time Domain Spectroscopic Technique

The coherent generation and detection of terahertz THz radiation using ultrashort optical pulses has become a standardized set-up in the field of THz spectroscopy today. Using theoretical simulations based on electrical field screening model, it was shown that THz

pulses of less than 100 femtosecond (fs) are possible[91]. However, the shortest free space THz radiation obtained in laboratory set-up was in the range of 300 fs. Therefore generation and detection of THz radiation were principally done using optical rectification of ultrashort laser pulses in thin Electro-Optic crystals[92], which was especially found to be a more efficient method of THz detection[93, 94]. However, as the pulse width of commercially available mode-locked Ti:sapphire lasers is approaching few tens of femtoseconds with ultrashort burst of visible/near-infrared laser pulses, ultrabroadband photoconductive generation/detection are being reported[95, 96] over 30 THz. Therefore, there is a renewed interest in employing photoconductive antennas for generation and detection of THz radiation.

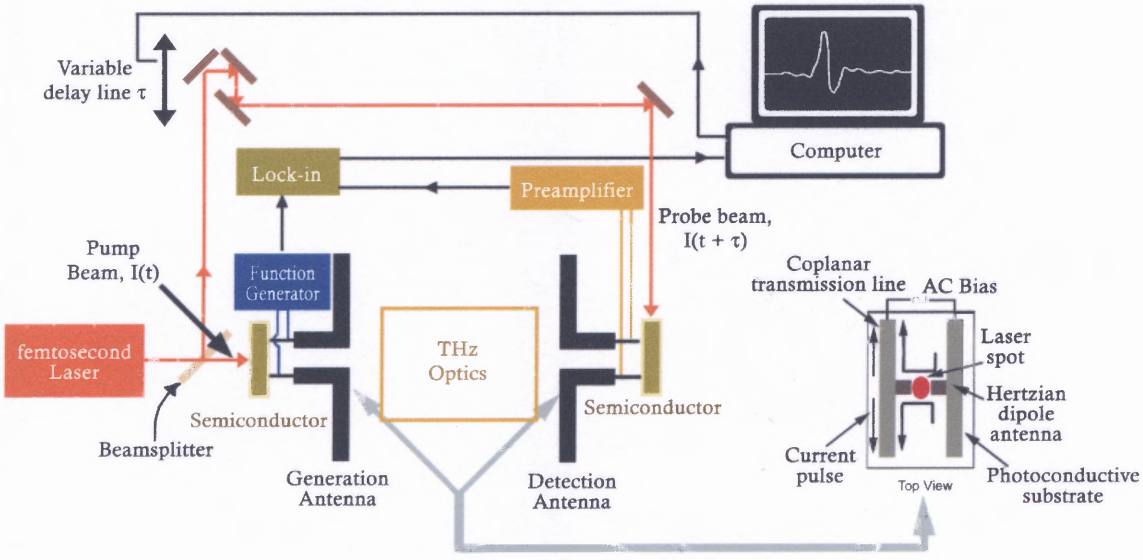

Figure 2.2 Experimental set-up for THz Time Domain Spectroscopy (THz-TDS).

In this technique, as described in Figure 2.2, an above-bandgap femtosecond laser pulse (pump beam) with intensity I(t) excites a biased semiconductor and consequently, electrons and holes are produced at the illumination point in the conduction and valence bands, respectively. These photoexcited carriers are then accelerated by the applied

electric ac bias (through function generator) and the physical separation of these charged carriers forms a macroscopic space-charge field oriented opposite to the biasing field. As a result, the fast temporal change in the electric field produces a transient current, which generates a pulse of electromagnetic radiation in the THz frequency range into free-space with the help of an antenna as shown in Figure 2.2. The production of ultrashort currents with a full-width half-maximum (FWHM) of 1 picosecond or less (to obtain radiation in THz frequencies) strongly depends on the carrier lifetime in the semiconductor which is tailored to become of sub-ps duration using various processing techniques such as annealing, ion implantation, and radiation exposure[33]. This type of semiconductors, for example, GaAs, is known as low temperature grown GaAs (LT-GaAs).

Following the schematic of Figure 2.2, the emitted THz pulse can be seen to be transmitted through an assembly of THz optics (which usually comprises of sets of parabolic mirrors, silicon lenses, etc.) and samples and then is collected onto the surface of another antenna for photoconductive detection. A part of the original femtosecond optical pulse that was used at the emission point (pump beam), is brought to this detection antenna (probe beam) with an intensity $I(t + \tau)$ after subjecting it to a variable delay line that delays it with time τ compared to the excitation pulse. Again photoexcited charge carriers are generated; however, the detection antenna is not externally biased. The incident THz electric field, in this case, provides the bias and a current I_{out}, proportional to the THz electric field amplitude and phase, is detected at the photoconductor pads which is detected as a voltage by a lock-in after passing through appropriate pre-amplification stage.

2.4 Continuous Wave THz Imaging Technique Using Photomixers

Among different forms of continuous-wave (CW) terahertz sources, photomixers are one of the most promising ones as potentially compact, low-cost, coherent, tunable and low power consuming THz sources[97, 98, 99]. This particular type of CW production of THz radiation is further favored by the availability of compact and inexpensive CW semiconductor lasers with high output power and stable monomode operation.

A THz photomixer essentially describes a photo-mixing process in which outputs of two single-mode lasers[100] or output modes of a dualmode laser[101] are used such that the frequency difference of the modes corresponds to THz range of frequencies.

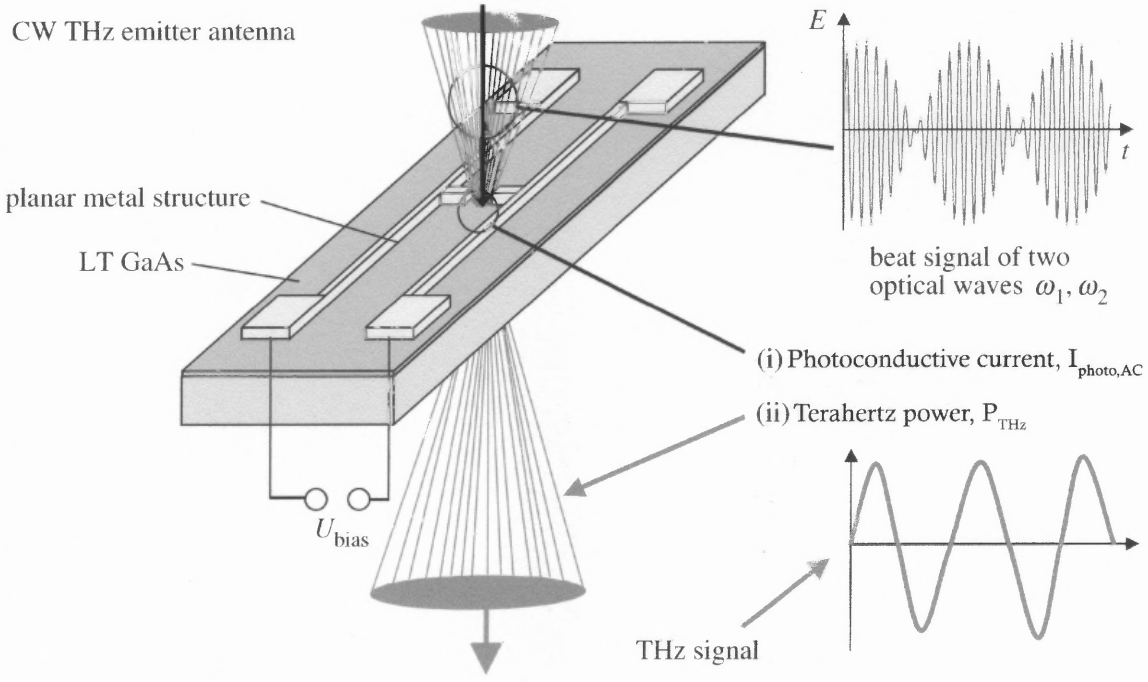

Figure 2.3 Photoconductive Hertzian-dipole antenna for the generation of CW THz radiation by the mixing of two visible/near-infrared laser beams, where one has (i) $I_{photo,AC} \propto U_{bias} P_{opt} \sin(\omega_{diff} t)$; (ii) $P_{THz} \propto I^2_{photo,AC}$.
(Source: T. Loffler et al., Phil. Trans. R. Soc. Lond. A, 362, 263 (2004))

As shown in Figure 2.3, these two modes of are then mixed accordingly in a nonlinear medium, such as a photoconductor[102] to generate a continuous wave signal whose frequency equals the frequency difference of the two lasers or two modes of the dual-mode laser.

Though an all-optoelectronic CW THz measurement system was demonstrated in 1998[103], the use of all optoelectronic THz generation/detection in CW THz imaging application is a relatively new implementation[104, 105].

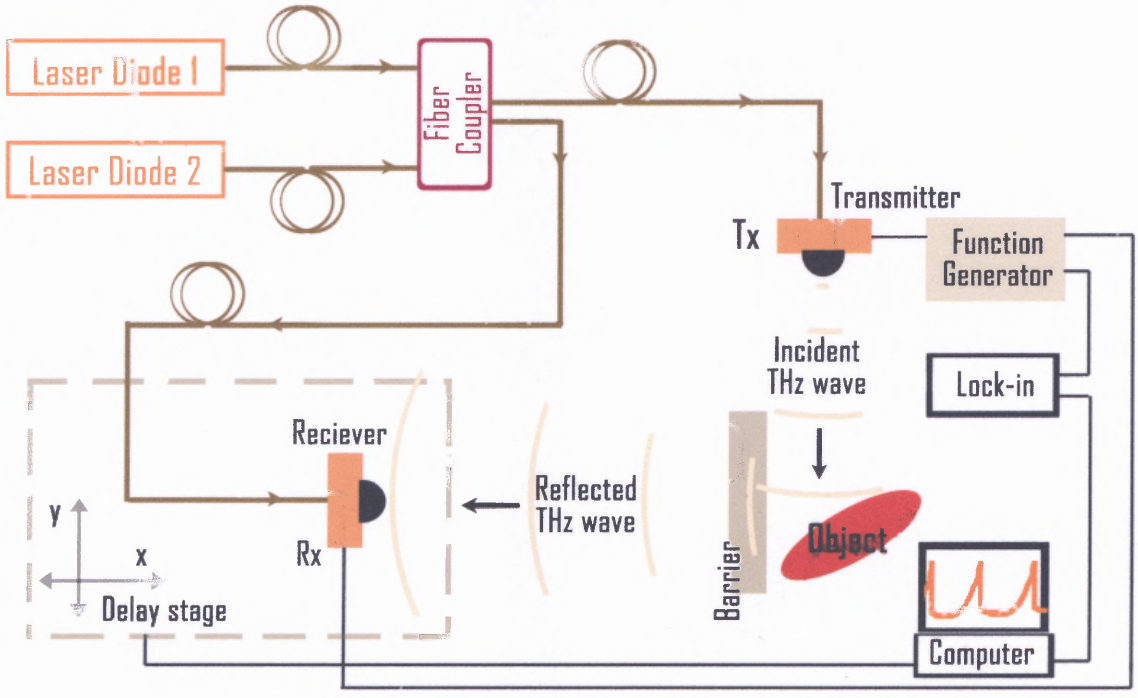

Figure 2.4 Experimental set-up for CW THz imaging with generation and detection of coherent THz waves using photomixing mechanisms.

In this scheme, as shown in Figure 2.4, either the object to be imaged or the receiver is mounted on a computer controlled *x*–*y* translation stage. To image one pixel of the object, the relative phase of the THz signal is varied by moving the optical delay line along *x* over only a few periods. The sampled temporal data points per period are then

employed to evaluate both amplitude and phase of the sinusoidal THz electric field of the object under THz illumination. In the attached figure, the imaging is in reflection mode.

In focal plane type of imaging, that is, where the number of pixels imaged at a time is equal to the number of receivers employed, the above process is repeated along y direction to obtain the complete image of the object in a scanning fashion. However, an alternative method is interferometric imaging which correlates the measured amplitude and phases by multiple receivers and reconstructs the image with number of pixels far more than the number of receivers employed. The detail of the same would be discussed in later chapters of this dissertation.

CHAPTER 3

IDENTIFICATION OF NON-ABSORBING GRANULAR SOLIDS IN TERAHERTZ RANGE: STUDY OF SCATTERING EFFECTS

3.1 Objectives

The primary motivation of this study is to understand the nature of the extinction or attenuation spectra of common granular solids such as, sugar, salt, flour and chalk in THz range and to establish the specific identification criteria, if any, for these solids through their THz extinction spectra obtained using THz Time Domain Spectroscopic (THz-TDS) technique.

For granular solids, apart from concentration (or particle density), moisture content, binder materials and other factors, the grain sizes of the solid itself play a major role in determining the THz spectra. Especially for solids having grain sizes comparable to THz wavelengths, the extinction spectra are greatly influenced by scattering losses which partially obscure the characteristic phonon resonances leading to complications in the quantitative analysis and subsequent material identification. The situation gets particularly critical when the materials under concern do not have any sharp intrinsic material absorption peaks in THz range. For these non-absorbing solid materials, therefore, one is required to consider the effects of scattering due to variation in sizes and shapes of the grains while analyzing their THz spectra. The following is therefore a case study to understand the nature of the scattering effects on the THz spectra of some common, non-absorbing granular solids and how it affects the identification criterion of the same in THz range. Apart from spectroscopic identification, the information regarding the scattering effects due to variation of grain sizes is equally vital for THz

imaging application, especially for THz security screening imaging system, as it directly affects the specificity of such a system in terms of successful spectral classifications of different lethal and non-lethal groups of materials.

3.2 Physical Basis of Scattering and Absorption

Whenever an electromagnetic wave propagates through a material medium, it experiences scattering due to the inhomogeneous nature of such medium[106]. It is an inherent quality of any material medium that either exists on the molecular scale or on the scale of aggregation of many molecules or both. As matter is composed of discrete electric charges, that is, electrons and protons; upon illumination by an electromagnetic wave, these electric charges of the medium, be it solid, liquid or even gas, are set into oscillatory motion by the electric field of the incident light. Subsequently, these oscillating electric charges or accelerated electric charges reradiate electromagnetic energy in all directions and it is this secondary radiation which is collectively known as scattering. Additionally to this secondary radiation, the excited bunch of electric charges of the medium may also transform a part of the incident electromagnetic energy into other forms through resonance processes that are characteristics of that particular medium (such as thermal energy through phonon resonance). That process is called the absorption.

However, almost all of the practical experimental arrangements that measure the attenuation of an electromagnetic wave in terms of either the reduction of the original field amplitude or intensity or energy of the incident wave upon the propagation through a finite distance through a material medium, essentially estimates the sum effects of these

two fundamental processes, that are the scattering and absorption. Moreover, as these two processes are not mutually independent, it is rather a very difficult task to isolate the effects of these two processes analytically. Nevertheless, careful experimental observation[107, 108] and theoretical analysis[109, 110, 111] can estimate (quantitatively, but only with certain degree of accuracy) the average attenuation of the electromagnetic wave caused by the scattering and absorption processes independently. In most of the cases, the procedure involved to extract the scattering contribution from the total attenuation of the electromagnetic wave is computationally challenging[112], but fundamental insights about the structure and composition of the material medium can be gained through such scattering measurements[113].

For an accurate estimation of the scattering contribution towards the total attenuation, it is a requirement of the experimental observation to be a phase sensitive optical measurement technique such as, THz spectroscopy, which directly measures the electric field amplitude of the scattered THz waves out of a medium. This condition is necessary as the scattering process of the electromagnetic radiation by the material medium essentially redistribute the radiation energy in all directions with changes in phase and amplitude as the scattered radiation. The effect is manifested through the alteration of the complex refractive indices of the medium that is, $\tilde{n} = n + i\kappa$ where n and κ are the real part and the imaginary part of the complex refractive indices of the material, respectively. However, any sharp change in the real part of the refractive index n, is principally associated with the phase change that occurs due to intrinsic absorption of the medium. While the imaginary part of the refractive index or the attenuation coefficient κ, carries the information of both scattering and intrinsic material

absorption[114]. As a consequence, simultaneous detection of both amplitude and phase of the transmitted radiation through the medium is necessary to evaluate n and κ accurately which in turn represent the absorption and scattering contributions towards total attenuation or extinction of the radiation energy by the material medium.

A physical example describes this fundamental and very important basis of scattering and absorption, where THz transmission through three discs of high density polyethylene (HDPE) is considered having different surface conditions, leading to different amount of scattering of the incident THz radiation[115]. The material HDPE has a very high transmission in THz range and therefore is used for manufacturing THz optics[116].

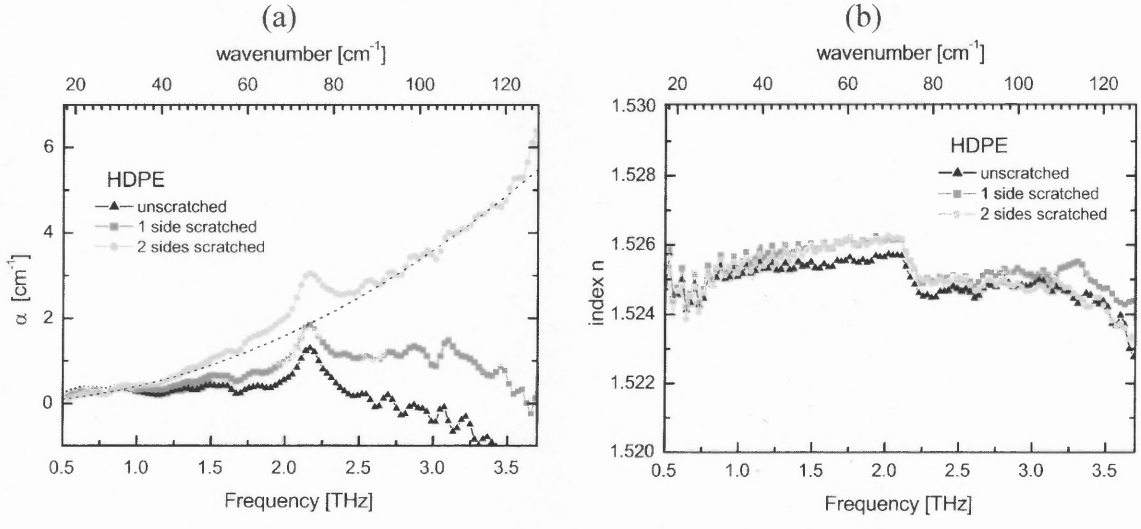

Figure 3.1 (a)The THz absorption and (b) the index of refraction of a high density polyethylene (HDPE) disc with different surface roughness.
(Source: M. Walther, PhD Thesis, Albert-Ludwigs Universitat Freiburg, Germany, 2003)

In this case as shown in Figure 3.1 (a), three different curves represent the absorption spectra (or essentially the attenuation coefficient κ as $\alpha = 4\pi\kappa\nu/c$ where α is the absorption, ν is the frequency and c is the velocity of light in vacuum) of the discs

with flat surfaces (unscratched) and of the same disc where the surfaces were roughened by sand paper (scratched), once on one side and the other one with both sides roughened. All the absorption spectra show an absorption feature centered at 2.15 THz, due to the characteristic lattice modes of the partly crystalline polyethylene. In addition to that, though the absorption of the unscratched sample is always below 0.2 cm^{-1} (apart from the phonon band peak at 2.15 THz), a rising scattering background is superimposed to the absorption of the scratched samples, with the stronger effect for the disc with two sides scratched. At the same time, the absorption band is accompanied by a characteristic change in refractive index (at exactly 2.15 THz) as shown in Figure 3.1 (b), typical for resonant processes, as discussed above. The real part of the refractive index n, does not show an effect due to scattering and has an average value of 1.525 in all cases. The slightly higher index of the scratched samples can be attributed to the decreased average thickness, which was not taken into account in the optical extraction procedure of evaluating n and κ, in the present case.

However, to separate the actual contribution of absorption and scattering towards the total attenuation from the above described analysis demands further theoretical scrutiny with careful considerations of the physical parameters of the medium such as the composition, sizes and shapes of the scattering centers and mutual distribution of same inside the medium. The values of these material parameters with respect to the frequency of the incident electromagnetic radiation set the regime of particular type of scattering processes such as Rayleigh scattering, Mie scattering and others[111]. In most of the cases, this part of the analysis becomes very complex and computationally involved, especially whenever multiple scattering events take place (which is the case in most of the

experimental observations) in a material and as a result the established scattering theories can only match the experimentally observed attenuation up to a certain degree of accuracy.

3.3 Scattering Studies in THz Range: Background and Current Status

By tapping the far infrared section of the electromagnetic spectra in form of THz radiation, researchers have now acquired the ability to image or to represent objects with a completely new perception which provide a rather different way to discriminate between them as well. However, for successful discrimination or classification of objects, it is essential to gain complete knowledge of the physical parameters of the materials that constitute such objects. Therefore, THz spectroscopic classification or identification of various materials is a prerequisite for any form of THz imager which attempts to discriminate objects based on their THz spectral information.

From spectroscopic standpoint, the appeal of exploiting the THz range for material classification is essentially three-fold:

- **Material signature:** The energies of terahertz radiation, that is, ~10^{-21} J (1 THz ≈ 4 meV and 1 eV ≈ 1.69e-19 J) are consistent with discrete molecular vibrational, torsional and other liberational modes in liquids and solids[117]. Especially low-frequency vibrations which are dominated by non-covalent, intermolecular interactions such as electrostatic, Van der Waals, and hydrogen bonds lie in the THz range[118].

- **Material transparency:** THz radiation is transmitted through most non-metallic and non-polar mediums, thus enabling THz systems to "see through" concealing barriers[119] such as packaging, walls, clothing, coatings etc. in order to probe hidden materials and as well as interfaces buried within dielectric structures[120].

- **Direct measurements:** Simultaneous detection of both amplitude and phase of the THz signal enables straightforward evaluation of the optical constants of the material without resorting to complicated Kramers Kronig relations[121].

Consequently THz spectroscopy of solids is a fast developing field of studies[122]. As a result, there is a growing need to develop an understanding of the interaction of this low energy, long wavelength radiation with commonly found solid substances and especially the underlying role of scattering events in propagation of THz radiation through solid media. Even though THz spectroscopy has been extensively used during the past decade to characterize numerous materials in the far infrared region of the spectrum, only recently granular solids are being inspected using THz radiation and experimentally observed absorption peaks are being reported[123, 124, 125, 126, 127, 128, 129, 130].

Submillimeter-wavelength scale of THz radiation implies that scattering will have significant effect on terahertz signals while passing through granular solids and will partially obscure the characteristic phonon resonances of the solid material leading to complications in the quantitative analysis. The radiation will either experience Mie scattering (proportional to v^m where m could be 1.1, 1.2, 1.5, 2.0 etc. depending on the material) or much stronger Rayleigh scattering (proportional to v^4) depending on the size distribution of the grains which could be either comparable or much smaller in scale to the THz wavelength, respectively. Despite this significant influence of scattering on the propagation of THz radiation through solids, experimental and theoretical work on scattering studies has been very limited in the THz range[131, 132, 133].

The origin of this current work, therefore, lies in a recent attempt that was undertaken by the THz Spectroscopy and Imaging group at NJIT to understand the effect of morphology of granular solids on their terahertz spectra in the region from 0.2 to 1.2 THz using samples of Ammonium Nitrate of different grain sizes[124].

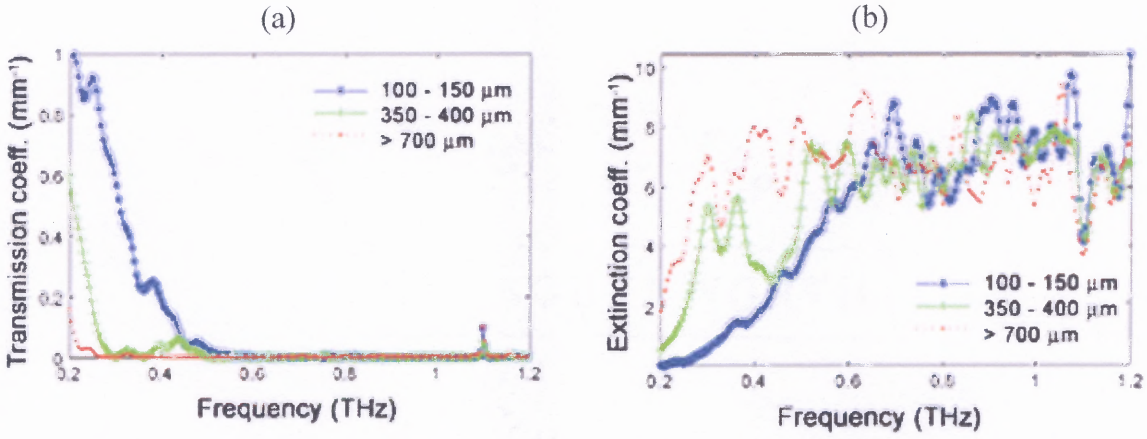

Figure 3.2 (a)Transmission and (b)extinction coefficients of different grain sizes of Ammonium Nitrate.
(Source: A. Sengupta, PhD Dissertation, New Jersey Institute of Technology, USA, 2006)

It was found that Ammonium Nitrate has monotonically increasing absorption spectra lacking any characteristic phonon resonance in the far IR range upto 3 THz[134]. Therefore, it was expected that changing the grain sizes of the sample, the effect of the scattering could be studied. As shown in Figure 3.2, it was found that the transmission and extinction spectra of samples of different grain sizes of Ammonium Nitrate show a characteristic trend with variation of grain sizes indicating scattering contribution to the total attenuation. The transmission spectra was later fitted to a $\sim\nu^2$ dependence and therefore Mie scattering was suspected to play a major role in this case[135]. Hence, to examine the physical basis of this observation, further investigations of experimental THz transmission and attenuation studies were carried out with commonly found granular substances such as, salt, chalk, sugar and flour in the range of 0.2 to 1.2 THz using THz time domain spectroscopic technique. The detail of this case study investigating the scattering effects of grain size variation on THz spectra of solids is described in the following section.

3.4 Scattering Studies of Common Granular Materials Using THz-TDS

In this section, it would be shown that the experimentally obtained THz extinction spectra of Ammonium Nitrate and as well as granular salt, chalk, sugar and flour of known grain sizes can be predicted on the basis of the Mie Scattering model at lower THz frequencies for smaller grain sizes. The current study is an attempt to extend the present understanding of scattering processes in solids in THz range. This study also sets a fundamental criterion for identification of non-absorbing, granular solids in THz range, which states that unique distinction of these kinds of solids cannot be made based on their rising trend of the extinction spectra at lower frequencies, as claimed previously by some researchers[120, 123].

3.4.1 Experimental Arrangements

In the present study, the general experimental configuration for THz Time Domain Spectroscopic (THz-TDS) set-up has been used in the transmission mode. The experimental arrangement consists of a Ti:Sapphire laser emitting 125 fs pulses at 800 nm, part of which pumps an Auston switch consisting of a semi insulating GaAs wafer with a gold transmission line structure microlithographically imprinted on it. These antennas have been fabricated at Lucent Technologies, Murray Hill, NJ.

The structure acts as a coplanar stripline (CPS) antenna when an AC bias is applied to it and becomes the source of THz radiation with a center frequency of about 0.5 THz. A silicon ball lens mounted above the antenna collects the emitted THz beam and guides it through a set of gold plated off axis parabolic mirrors to the detector. The detection scheme is just the reverse of the generation process, where the incoming THz electric field provides the bias for the antenna which is optically gated by the other part of

the laser pulse. The sample being studied is placed at the focus of the THz beam between two parabolic mirrors. The experimental layout is shown in Figure 3.3.

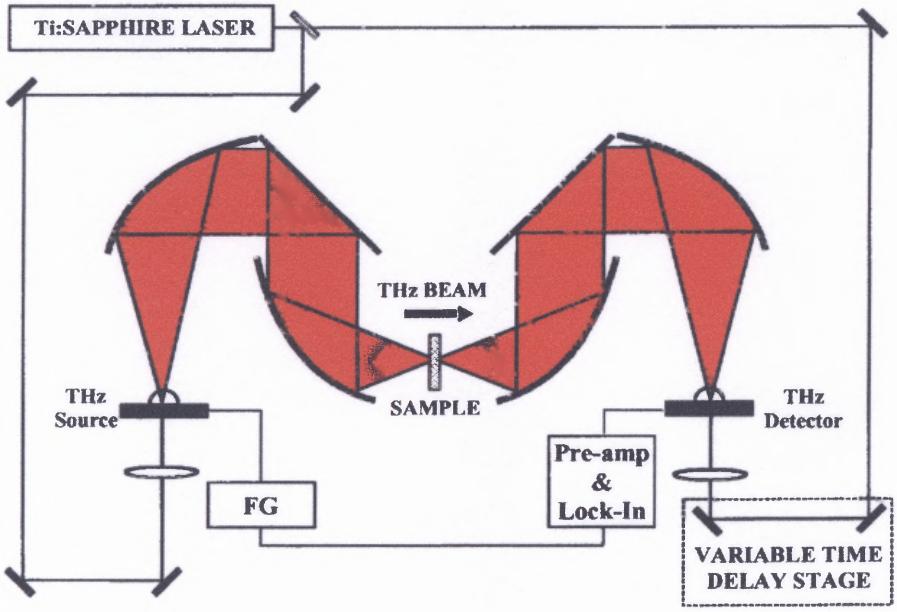

Figure 3.3 Schematic of a THz-TDS system in transmission geometry.

3.4.2 Sample Preparation

The sample of salt was made from dry crystalline form of extra fine Diamond Crystal® table salt that is available commercially having an average grain size of 100-150 μm. The sugar sample of average grain size of 300-350 μm was obtained from Shoprite® sugar and flour sample of average grain size of 150-200 μm was obtained from commercially available Pillsbury® flour. For the chalk dust, a Crayola® chalk stick was crushed to a powder of average grain size of 80-120 μm. Individual sets of grains were spread out uniformly over Scotch® polyethylene packaging tape which was used as the sample holder for each case and the two tapes sticking together was used as the reference or

"blank" for the measurements. The final sample thickness of salt, sugar, flour and chalk were of 0.3 mm, 0.6 mm, 0.4 mm and 0.25 mm respectively.

The samples of Ammonium Nitrate (CAS # 6484-52-2, from Fischer Scientific®) having an average grain size of 700-750 μm were spread out uniformly in three sets of samples over Scotch® polyethylene packaging tape. The first set of the samples had a thickness of 1.602 mm. The next two sets were crushed using mortar and pestle to an average grain size of 350-400 μm, thickness: 0.380 mm and 100-150 μm, 0.413 mm respectively[132].

The standard procedure of making pellets mixed with high density polyethylene (HDPE) using a pellet press was avoided in order to maintain control over the grain sizes. Moreover, it has been reported that inexact mixing of PE powder and the compounds affects the absorption spectra[136].

3.4.3 Analysis of Experimental Data

Time resolved THz spectroscopy measurements provide simultaneous information about the amplitude and phase of the samples under study. One reference waveform $E_{ref}(t)$ is measured without the sample or with a sample of known dielectric properties, and a second measurement $E_{sample}(t)$ is performed, in which the THz radiation interacts with the sample. In the present case, $E_{ref}(t)$ was obtained through "blank" and $E_{sample}(t)$ was the signal through different granular samples. The transmission spectrum is calculated using the Discrete Fourier Transform (DFT) of the sample and reference measurements,

$$T_{\exp}(\nu) = \frac{\left|E_{sample}(\nu)\right|}{\left|E_{ref}(\nu)\right|} \tag{3.1}$$

The extinction of a material is defined as the true absorption which is the sum of intrinsic material absorption and the extrinsic losses associated with scattering, that is, extinction = material absorption + scattering loss[111]. In this study, the experimentally obtained extinction is defined as:

$$\text{Extinction, } \varepsilon(\omega) = -\ln\left(\frac{|E_{sample}(\omega)|}{|E_{reference}(\omega)|}\right) \tag{3.2}$$

Previous work[126] showed that the THz extinction of Ammonium Nitrate of different grain sizes rises slowly with frequency which does not follow Rayleigh scattering where a dependence of ν^4 is expected. Thus Mie theory which is more comprehensive in dealing with spherical grains of arbitrary size is considered for explaining this trend in the extinction spectra.

The fundamental assumptions of Mie theory involve independent elastic scattering and single event scattering by spherical scatterers. The first assumption of elastic scattering requires that, the frequency of the scattered radiation is the same as that of incident radiation which is the case in the present situation as the samples under study do not show any non-linearity in the THz region. The second assumption of single event scattering essentially requires that the number of grains are small and their mutual separation is such that the in the neighborhood of any grain the total field scattered by all the rest of the grains is small compared to the external field. This ensures that the total scattered field is just the sum of the fields scattered by all the individual grains, each of which is acted on by the external field of the incident radiation in isolation from the other grains. The assumption of single scattering is relatively restrictive in the present case, particularly in higher frequency region or for bigger grains as the mutual separation

between two grains becomes comparable to the wavelength. Lastly the assumption of spherical scatterers holds true only for smaller grain sizes as they truly approach spherical shape with an aspect ratio of almost one. However, bigger grains deviate considerably from spherical shape and in those cases, Mie theory does not hold true. In general, Mie scattering model is a well studied model and the algorithm for the computational evaluation of the same has been developed over many years[137, 138, 139].

3.4.4 Theoretical Modeling

The geometry of the incident and scattered fields is shown in Figure 3.4. The plane of reference is taken through the directions of propagation of the incident and scattered waves. The perpendicular and parallel components of the electric field of the incident wave are $E_{ol} = \cos\varphi$, $E_{0r} = \sin\varphi$ and those of the scattered wave are $E_l = E_\theta$, $E_r = -E_\varphi$.

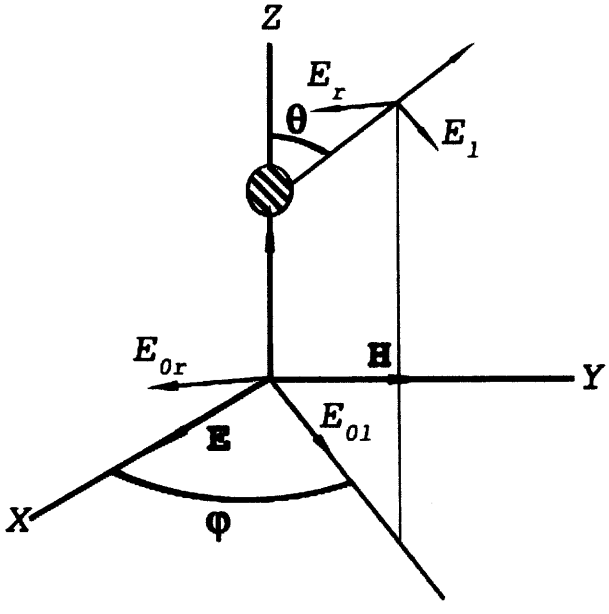

Figure 3.4 Decomposition of electric vectors of incident and scattered waves.

Here *r* denotes the perpendicular component and *l* denotes the parallel component of the electric field. Thus, Mie's formal solution for spheres of arbitrary size is given by[111],

$$\left.\begin{aligned} E_\theta &= -\frac{i}{kr} e^{-ikr+i\omega t} \cos\varphi S_2(\theta) \\ E_\varphi &= \frac{i}{kr} e^{-ikr+i\omega t} \sin\varphi S_1(\theta) \end{aligned}\right\} \tag{3.3}$$

where $S_1(\theta)$ and $S_2(\theta)$ are two elements of the scattering matrix, $S(\theta,\varphi)$ and are known as amplitude functions, $k = 2\pi/\lambda$ is the wave number in vacuum and ω is the angular frequency. The radial components of the electric field are ignored as they tend to zero with higher powers of *1/r*.

In the present experimental set-up, the incident THz field is p-polarized. Hence, the theoretical extinction coefficient, μ_{th}, is calculated from the amplitude functions for $\theta = 0$ ($S_1(\theta)$ *and* $S_2(\theta)$ are equal for $\theta = 0$) and is given by,

$$\begin{aligned} \mu_{th} &= N\frac{c^2}{\pi v^2}\mathrm{Re}[S(0)] \\ &= N\frac{c^2}{2\pi v^2}\sum_{m=1}^{\infty}(2m+1)\,\mathrm{Re}(a_m + b_m) \end{aligned} \tag{3.4}$$

where N is the number of grains per unit volume, c is the speed of light and a_m, b_m are coefficients of the infinite summation such that,

$$\left\{\begin{aligned} a_m &= \frac{\psi_m'(y)\psi_m(x) - n\psi_m(y)\psi_m'(x)}{\psi_m'(y)\zeta_m(x) - n\psi_m(y)\zeta_m'(x)} \\ b_m &= \frac{n\psi_m'(y)\psi_m(x) - \psi_m(y)\psi_m'(x)}{n\psi_m'(y)\zeta_m(x) - \psi_m(y)\zeta_m'(x)} \end{aligned}\right. \quad where \left\{\begin{aligned} \psi_m(z) &= z j_m(z) \\ \zeta_m(z) &= z h_m^{(2)}(z) \end{aligned}\right. \tag{3.5}$$

where $j_m(z)$ and $h_m^{(2)}(z)$ are Spherical Bessel functions of the first kind and third kind[140] respectively when z can be either $x = 2\pi vr/c$ or $y = 2\pi vnr/c$ and r is the radius of the spherical grain and n is the real part of the complex refractive index. Equation (3.4) is the

theoretical equivalent of Equation (3.2) and takes into account both the intrinsic absorption of the material as well as extrinsic losses involving single scattering events.

Mie theory also defines the complex refractive index of a scattering material as $\tilde{n}(v) = 1 - i2\pi NS(0)/k^3$. Equating the real and imaginary parts of this equation with $\tilde{n}(v) = n(v) + i\kappa(v)$, where $n(v)$ and $\kappa(v)$ are the frequency dependent real and imaginary parts of the complex refractive index $\tilde{n}(v)$, one readily obtains,

$$\begin{aligned} \kappa(v) &= \frac{2\pi N \,\mathrm{Re}[S(0)]}{k^3} \\ &= \frac{\mu_{th} c}{4\pi v} \end{aligned} \tag{3.6}$$

which is the effective attenuation factor caused by the sum effect of material absorption and scattering losses, neglecting the effects of insignificantly small radiation pressure in the present case (it is inversely proportional to the velocity of light).

One can then separate the theoretical extinction coefficient μ_{th} into the coefficients of intrinsic material absorption μ_{abs} and scattering μ_{sca} as $\mu_{th}(v) = \mu_{abs}(v) + \mu_{sca}(v)$ where $\mu_{sca}(v)$ is also calculated using Mie theory and is given by,

$$\mu_{sca} = \frac{Nc^2}{2\pi v^2} \sum_{m=1}^{\infty} (2m+1)(|a_m|^2 + |b_m|^2) \tag{3.7}$$

In all of the above analysis, $n(v)$ can be assumed to be n, the frequency independent broadband refractive index, as all of the granular solids are known to have no sharp absorption features[120, 123, 125, 131] in the frequency range of the present study. In other words, there is no contribution of any intrinsic material absorption causing a sharp change in the value of the real part of the refractive index, as explained in the previous section.

3.4.5 Results

The experimental results obtained for the common granular materials (that is, salt, sugar, flour and chalk) and the experimental data of Ammonium Nitrate[132] are analyzed in the following sections where the Mie scattering model has been applied to the extinction spectra of all of the granular samples.

3.4.5.1 Raw Time Domain Data and Amplitude Spectrum. In Figure 3.5 (a), typical THz electric fields for the "blank" and for flour of 150-200 μm grain size have been shown. The corresponding amplitude spectrum is shown in Figure 3.5 (b) from which it is evident that the acceptable frequency range in our THz-TDS system is approximately between 0.2 and 1.2 THz.

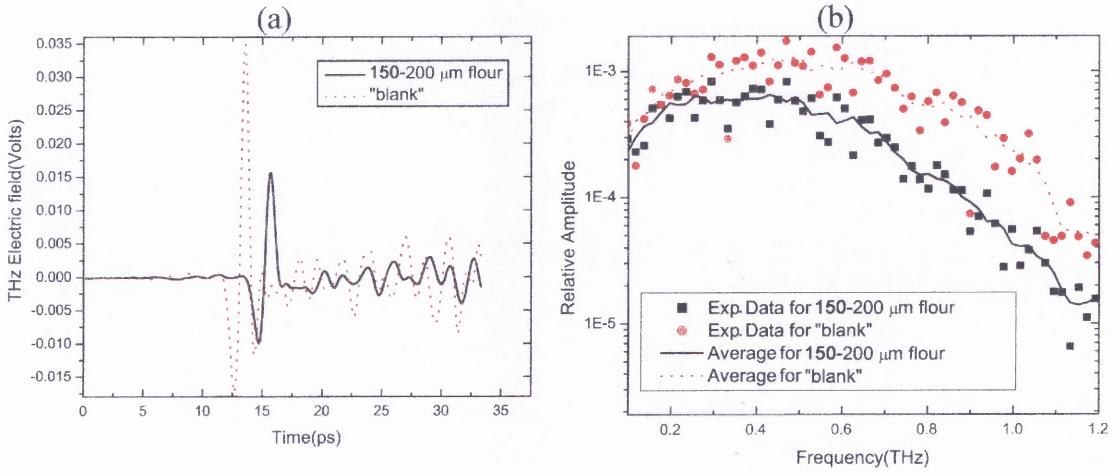

Figure 3.5 (a) THz fields for 150-200 μm grain size flour and "blank" samples and (b) THz amplitudes of the same. The dips at 0.56, 0.78 and 1.13 THz are due to water vapor absorption. The "blank" was almost 95% transparent and completely featureless between 0.2 and 1.2 THz.

For the purpose of brevity to avoid any repetition, corresponding plots obtained for other samples (salt, sugar, chalk and Ammonium Nitrate of different grain sizes) are not shown here. From these time domain plots, the broadband refractive indices of the

materials under study can also be calculated by observing the delay in the arrival of the THz pulse when the sample of finite thickness is placed between the source and the detector. This technique is validated by finding the broadband refractive indices of flour, salt and Ammonium Nitrate to be 1.44, 1.54 and 1.82, respectively which agree with previously reported values[120, 123, 141] in the existing literature.

3.4.5.2 Mie Theory Calculations of Extinction for Non Absorbing Spherical Solids. The experimental extinction data for the different samples is shown in Figure 3.6 with the theoretically calculated extinction curves up to the 4^{th} order term of Equation (3.4).

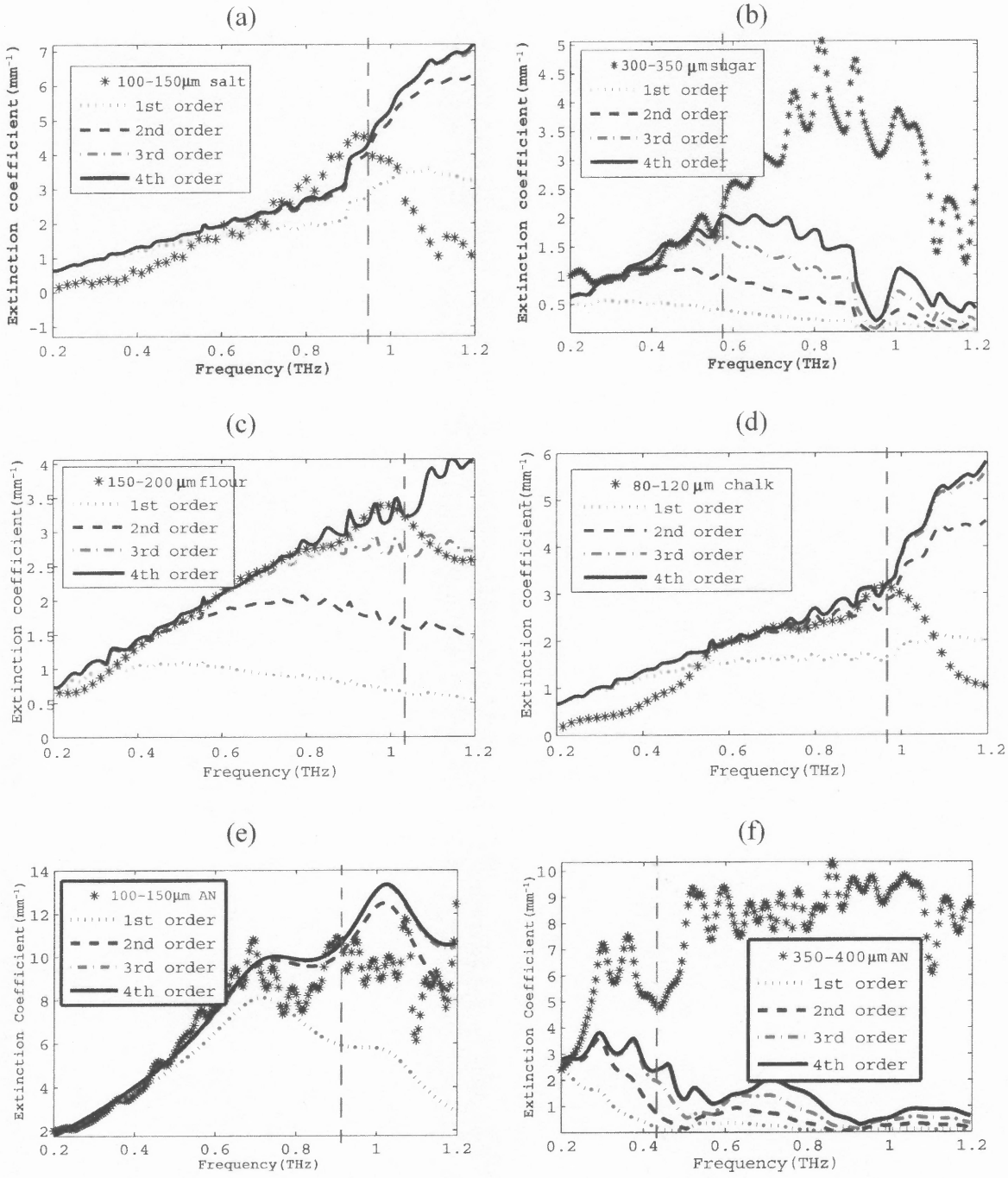

Figure 3.6 Experimental and theoretical predictions of extinction coefficients for (a) 100-150 μm grain size of salt; (b) 300-350 μm grain size of sugar; (c) 150-200 μm grain size of flour; (d) 80-120 μm grain size of chalk; (e) 100-150 μm grain size of Ammonium Nitrate and (f) 350-400 μm grain size of Ammonium Nitrate. The red dotted line in parts (a), (c), (d) and (e) shows the region up to which the prediction of Mie theory matches satisfactorily with the experimental analysis.

In all of the above plots, Equation (3.4) has been terminated at 4th order as it produces hardly any deviation as m changes value from 3 to 4. A comparison of the experimental and theoretical data for 700-750 μm Ammonium Nitrate shows a strong discrepancy in the 0.2-1.2 THz range and hence, has not been shown. It is suspected that this deviation is mainly due to the fact that the grains of these samples were mostly nonspherical in shape.

The apparent roll off at higher frequencies as seen in Figure 3.6 for all of the materials does not indicate any true phonon characteristic resonance but rather indicates the threshold of the region of validity of Mie theory. In other words, the fundamental assumption of Mie theory of single event scattering ceases to hold in higher frequency range as the incident wavelength becomes smaller compared to the size of the scatterers and their mutual separations leading to a dominance of multiple scattering events[142]. It is also observed that the experimental THz extinction of the materials with larger grain size (Sugar of 300-350 μm grain size and Ammonium Nitrate of 350-400 μm grain size) show significant deviation from the theory as any random irregularities of the spherical shape of the scatterers become prominent to the incident wavelength with larger grain sizes. This contradicts the other assumption of the Mie theory which requires the scatterers to be spherical. In fact, on inspection of the samples with a microscope, it was found that the grains in the case of 100-150 μm salt, 150-200 μm grain size of flour, 80-120 μm grain size of chalk and 100-150 μm of Ammonium Nitrate were typically spherical while the larger grains of sugar and Ammonium Nitrate form considerably irregular clusters.

3.4.5.3 Mie Theory Calculations of Absorption and Scattering Coefficients. Two separate parts of theoretically predicted extinction, i.e, the intrinsic material absorption and extrinsic scattering losses, for the small grain samples of salt (Figures 3.7 (a) and (b)) and of Ammonium Nitrate (Figures 3.7 (c) and (d)) are shown using Equation (3.7).

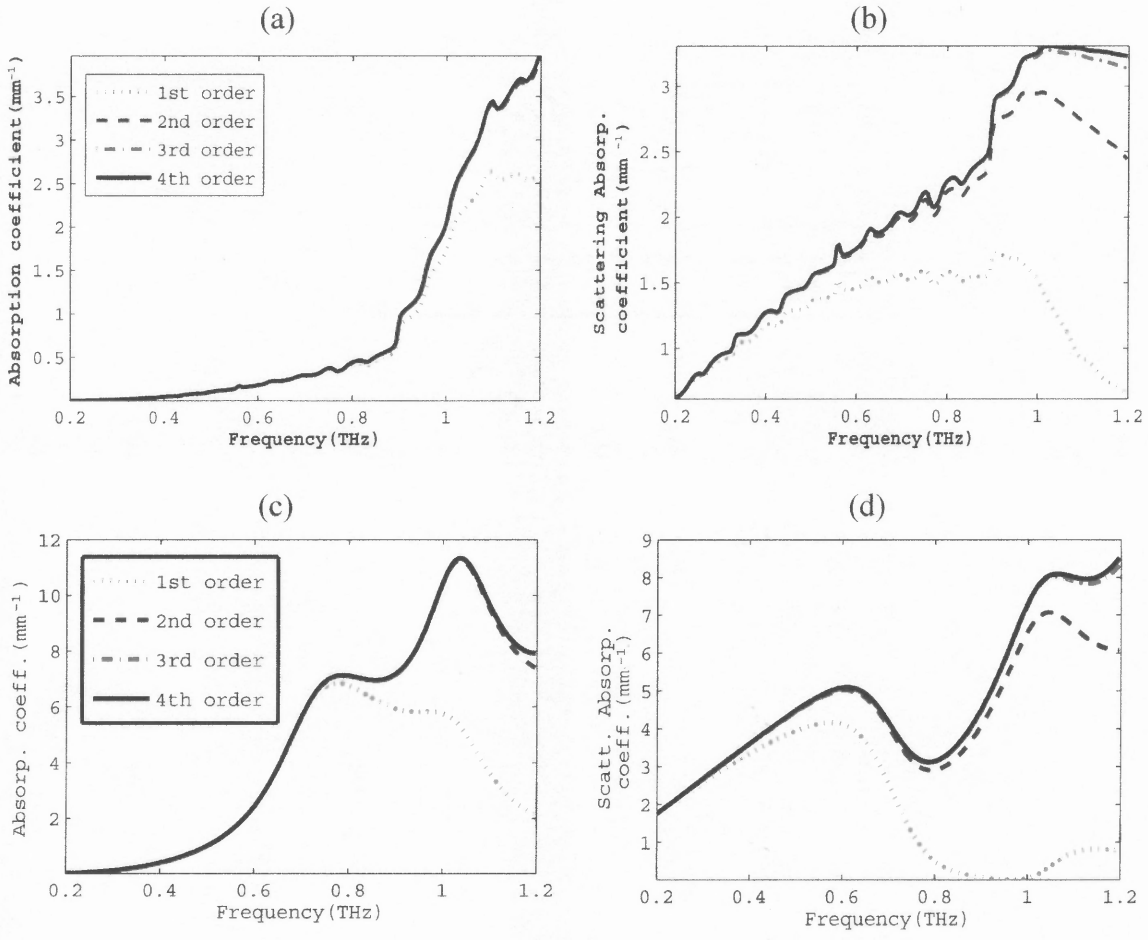

Figure 3.7 Theoretically predicted absorption and scattering coefficients for (a) and (b) 100-150 μm Ammonium Nitrate and (c) and (d) 100-150 μm salt respectively. Similar legends have been followed for all the figures.

From the Figure 3.7, it is seen that at lower frequencies, single event scattering is the predominant contribution towards the total extinction and thus Mie scattering model is successful implementation in the present case in the lower THz frequencies. For reasons of repetition, similar plots of sugar, flour and chalk have not been shown here.

3.4.5.4 Identification of Non Absorbing Spherical Granular Solids. From Figure 3.6, it can be observed that all the materials investigated, namely salt, sugar, flour, chalk and Ammonium Nitrate, have rising trends in their extinction spectra as observed experimentally which matches with the prediction of Mie theory in the limit of weak scattering, that is, in the region of lower THz frequencies. Provided that this trend in the spectral shape is characteristic of the material, previous reports have suggested that this might offer a possibility for spectral identification in the lower THz frequencies[120, 123].

Therefore, to test the possibility, a generic curve based on Mie theory has been plotted which predicts the total extinction coefficient for different materials, M with refractive indices n_M, and a range of values of size parameter, x, to account for any variation of their size and/or wavelength as shown in Figure 3.8. In this surface plot $x = 2\pi\nu r / c$ is the size parameter which is defined as the ratio between the size of the grain and the centre wavelength of the probing radiation, is an important dimensionless quantity in scattering analysis.

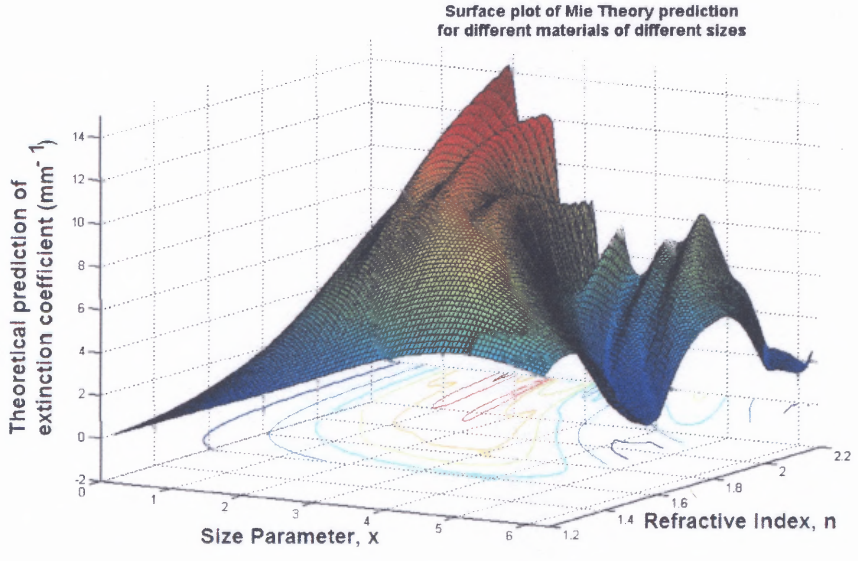

Figure 3.8 Generic plot of Mie scattering theory predicted extinction coefficients for materials having refractive indices, n and size parameters, x.

To understand the underlying information in a more conceivable fashion, the surface plot can be sliced into several sections along the lines of constant refractive index, *n* and then one obtains a two dimensional multitude plot as shown in Figure 3.9.

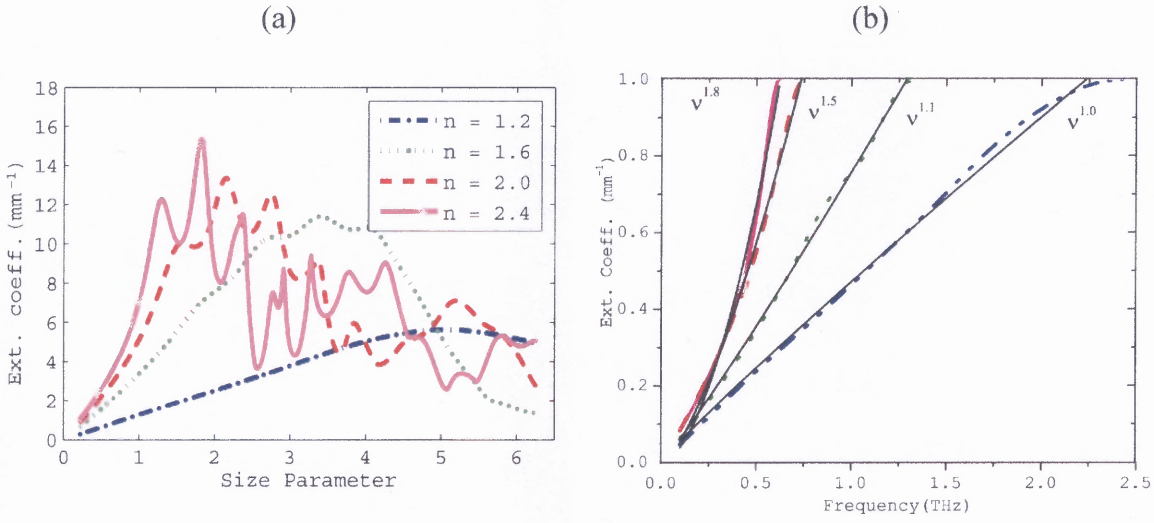

Figure 3.9 (a)Theoretically predicted extinction coefficients for materials having refractive indices, *n* and size parameters, *x*; and (b) the normalized extinction coefficient for a grain size of 100 μm as a function of frequency.

In the lower frequency region, this plot provides an incisive estimation of the total extinction for materials with a particular refractive index value and grain size. As shown in Figure 3.9 (b), (where the graph of Figure 3.9 (a) has been enlarged to show only upto the first undulation in the data), this becomes apparent when the different frequency dependences of the extinction coefficient are plotted for a constant grain size of 100 μm.

Hermann et al.[120] and Brown et al.[123] have reported experimental findings on absorption spectra of solid grains where they have shown the frequency dependence to be approximately ν^1 and ν^2 respectively, for flour (n ~ 1.4) and sugar (n ~ 2.0). Upon a direct comparison of these frequency trends with the theoretical plot of Figure 3.9 (b), one may find that the predicted extinction spectra according to Mie scattering theory are

to be indeed $\nu^{1.0}$ and $\nu^{1.8}$ for those materials with those particular grain sizes. This effectively suggests that their observed spectra were primarily due to single event scattering contribution of the grains under study (flour~50 μm, sugar~300 μm). Moreover, from Figure 3.9 (a) one can readily argue that these frequency trends are not unique or representative of the materials used, as extinction is a function of the refractive indices, n and as well as the size parameters, x of the samples. In fact, for a specific material with different grain sizes, one would obtain varying frequency dependence of extinction. Likewise, the grain sizes of different materials could be chosen in such a way that the extinction spectra of all those different materials with varying grain sizes would show a particular frequency trend. For example, 200 μm grains of flour and 450 μm grains of sugar would yield the same frequency trend of $\nu^{1.1}$ in the extinction spectra. Therefore, the frequency dependence of extinction spectra cannot be used for identifying non absorbing spherical granular solids of unknown grain sizes in the weak scattering region. Nonetheless, Figure 3.9 (a) and 3.9 (b) also show that, in certain cases where the grain sizes are accurately known for a particular non-absorbing solid, the frequency trend of extinction spectra could be used for a broad classification of granular solids since one can essentially estimate their refractive indices.

3.5 Conclusions

In this study experimentally obtained extinction spectra of granular salt, sugar, flour, chalk and Ammonium Nitrate of different grain sizes between 0.2 to 1.2 THz using THz time domain techniques have been presented. It has been shown that the obtained extinction for these non-absorbing materials in the frequency range of study essentially

consist of scattering losses. It is demonstrated that, the experimentally obtained extinctions of these non absorbing solids of spherical grains can be predicted on the basis of Mie theory in the weak scattering limit. The intrinsic material absorption and scattering losses are separated from the total extinction and thus, this work makes an attempt to reconcile the apparent discrepancies in the extinction values of different materials of varying grain sizes by calculating the expected frequency dependence of such materials due to the impact of scattering. Finally, it can be deduced from this study that any identification of an unknown granular solid in a concealed manner cannot be made based on the frequency trend of its THz extinction spectra, as the frequency dependence of the extinction of a solid is a function of both its material property, as well as its grain size. This work, therefore, might prove to be a crucial step towards successful material identification under THz study by a complete understanding of the apparent discrepancies in the extinction spectra brought about by the variations of different morphologies of non absorbing spherical granular solids.

CHAPTER 4

GUIDED TERAHERTZ PROPAGATION: HOLLOW CORE WAVEGUIDES

4.1 Introduction

With the advent of semiconductor optoelectronics technology[143], generation and detection of coherent THz radiation has become possible. Associated with the development of THz technology and techniques, a search for flexible guiding systems for THz transmission has also become crucial. Guided propagation of THz waves is advantageous as the THz beam can be directed into obscure places, around the bends without employing any bulk optics and as most of the radiation energy is trapped inside the small cross-section of the core of the waveguide structure during its propagation, spectroscopic measurements can be done with enhanced sensitivity[144]. Coupled with this fact, guided THz propagation is also advantageous to reduce atmospheric losses of THz radiation as shown in Figure 4.1 which is prevalent in free-space THz propagation and is especially important for high frequency THz range.

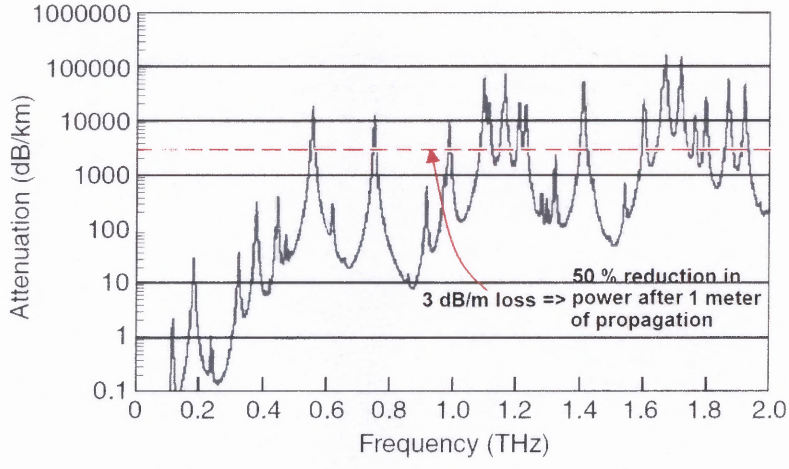

Figure 4.1 The water vapor absorption spectrum of THz radiation in atmosphere.
(Source: M.J. Fitch and R. Osiander, Johns Hopkins APL Technical Digest, **25**, 348 (2004))

Hollow waveguides present an attractive alternative to other forms of THz guiding structures owing to their ability to transmit THz wavelengths with low loss and their relatively simple structure and potential low cost[145]. In the present study, characterization in terms of its attenuation and dispersion profile is made for a straight, circular Cu coated hollow core waveguide of bore size 2 mm. The attenuation coefficient of the lowest loss mode and the group velocity dispersion and waveguide dispersion of the waveguide under study have also been calculated.

4.2 Background

From mid 1960's the research effort had been directed to develop a variety of materials for transmitting wavelengths greater than 2 μm[146, 147]. This thrust gained impetus in conjunction with the silica-based fiber optics which brought major impacts in telecommunications and in general, optoelectronic industry including laser power transmission for various sensing applications. While these silica-based fibers have offered excellent optical properties upto 2 μm; longer wavelengths, especially CO_2 lasers which are particularly important for medical applications, cannot be transmitted through these fibers. Therefore alternative materials like fluoride[148] and chalcogenide glasses[149], single crystalline sapphire[150], polycrystalline silver halides[151] and many others were pursued as a potential candidate for guiding wavelengths of 20 μm and beyond.

Around the same time, air-core guiding of CO_2 laser through simple metallic structure was also demonstrated[152] and the use of flexible, circular hollow waveguides became common later on, especially in medical diagnostics[153]. The interest in guided THz propagation, which is a submillimeter range of wavelengths, arose recently with the

advent of photonic crystal fibers which exhibit omnidirectional behavior[154,155] and with low loss and dispersion of THz transmission through metal wires[156]. The utility of transport of THz pulses in hollow core waveguides, especially in circular structures, are also recently being inspected and characterization of their attenuation profile, dispersion and bending losses are in progress[157, 158, 159]. Various applications like bio-medical imaging and diagnostics, nondestructive evaluation of material parameters, chemical and gas sensing, remote sensing and security screening are expected to improve their performance through guided THz transmission. In most of these applications, THz waveguides would either play the crucial role of a short-haul energy transmitter from a broadband source to remote sensors or as a coupler between the THz source and other parts of the optics in an integrated system employed especially for imaging or communication.

4.3 THz Propagation in Hollow Core Metal Waveguides

The concept of using hollow metal pipes to transmit EM waves began in the times of Rayleigh in 1897. However, it was in the 1930s when hollow waveguides became widespread in the use of transmitting microwave frequencies which are millimeter to centimeter wavelengths. These kinds of structures offer very low dissipative losses in that range. The extension of this idea from microwave regime to mid-IR and finally far-IR range of wavelengths was not straightforward. It was 1974, when rectangular hollow waveguides were first used[160] to transmit CO_2 wavelengths. Then gradually the field of hollow core metal waveguides gained its prominence in transmitting longer wavelengths offering superior flexibility and reliability. However, the issues of very strong

dependence of attenuation of the waveguide on its bore size and bending losses restrict the use of hollow core waveguides in many applications[142].

4.3.1 Fabrication of the Hollow Core Waveguides (HCWs)

The fabrication of hollow core waveguide involves coating of the inside of either silica or polymer tubing with metallic and metallic/dielectric coatings using liquid-phase chemistry methods. For this study, Copper was chosen as the metallic layer because it is one of the best reflectors at THz frequencies, having a measured reflectivity of 0.997 at 513.02 μm[161]. The reason for using polycarbonate tubing was because it has a very smooth inner surface nearly equal in roughness to silica glass and secondly the use of the same allows the guides to be quite flexible even with relatively large bore sizes. The polycarbonate tubing used for this study has bore sizes of 2 mm. In contrast, glass tubing with similar bore size would be inflexible.

During the fabrication, Copper films were deposited inside polycarbonate tubing using an electrode less, liquid-phase chemistry process[162]. The first step involves sensitizing the polycarbonate using an aqueous solution of $PdCl_2$ and $SnCl_2$. Next a copper bath solution was prepared consisting of copper sulfate, formaldehyde, Rochelle salt, and sodium hydroxide with a pH of 12.5. This solution was pumped through the plastic tubing at a flow rate of 5 ml/min. The formaldehyde reduces the Cu ions and Cu metal plated out on the tubing. The duration of the deposition process is 30 to 45 min and the estimated thickness of the Cu layer formed is 0.5 to 0.7 μm. This thickness is much greater than the skin depth of about 0.05 μm for Cu at THz frequencies. A schematic of the prepared hollow core waveguide and the diagram of the coating process are shown in Figure 4.2 (a) and 4.2 (b) respectively.

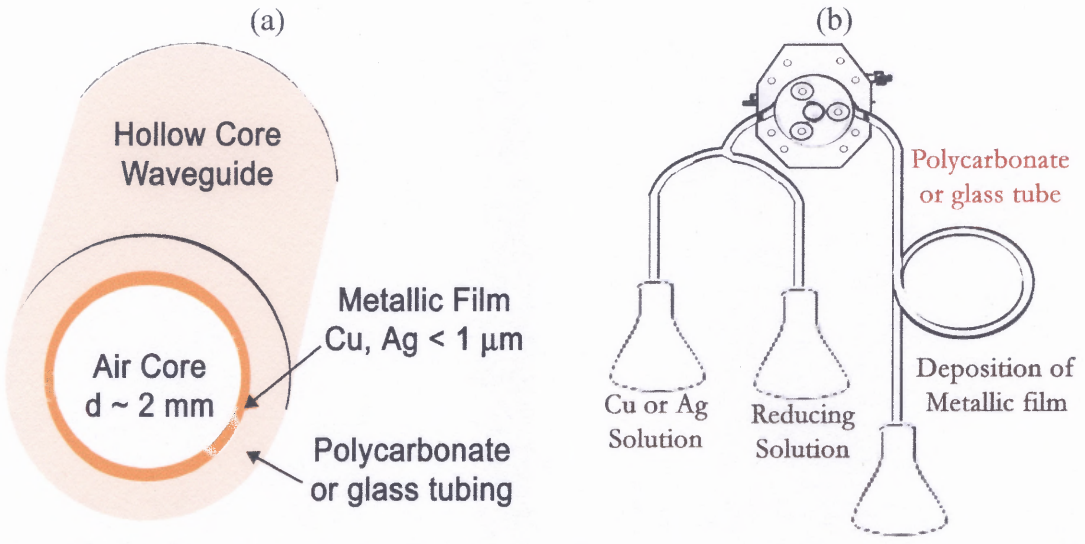

Figure 4.2 (a) Transverse section through a hollow core waveguide showing the profile of the structure, and (b) Schematic of the waveguide fabrication procedure.

4.3.2 Experimental Arrangements for THz Characterization of HCWs

The experimental arrangement for THz characterization of the hollow core waveguides consists of a standard THz-Time Domain Spectroscopic (THz-TDS) set-up, where a Ti:Sapphire laser emitting 125 fs pulses at 800 nm is used as the pump source. A part of the same pumps an Auston switch consisting of a semi insulating GaAs wafer with a gold transmission line structure microlithographically imprinted on it. The structure acts as a coplanar stripline (CPS) antenna when an AC bias is applied to it and becomes the source of THz radiation with a center frequency of about 0.5 THz. A silicon ball lens mounted above the antenna collects the emitted THz beam and guides it through a set of gold plated off axis parabolic mirrors to the detector. The detection scheme is just the reverse of the generation process, where the incoming THz electric field provides the bias for the antenna which is optically gated by the other part of the 800 nm laser pulse.

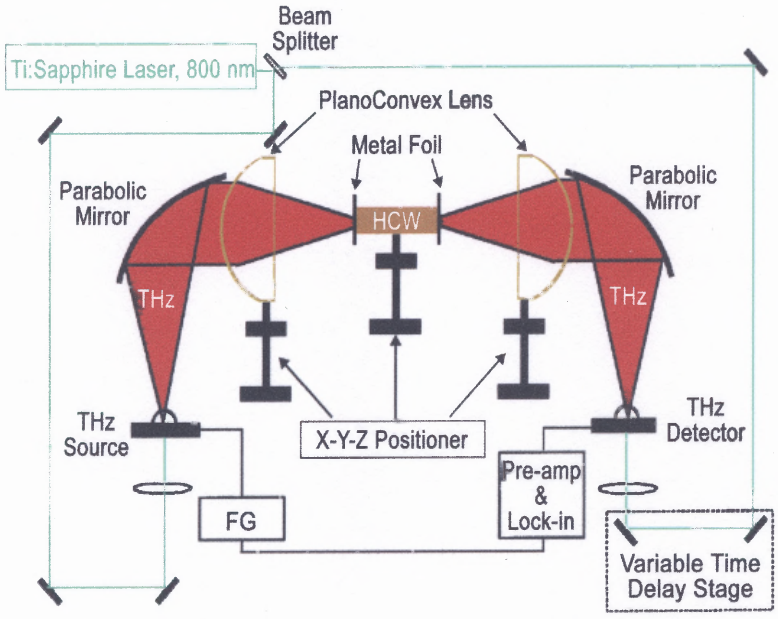

Figure 4.3 Schematic of the THz-TDS system used for hollow core waveguide characterization.

As shown in Figure 4.3, the Cu coated hollow core waveguide was placed at the focus of the plano convex lens at the THz source side and the guided pulse was collected by the second plano convex lens to direct the collimated beam to the parabolic mirror. The pair of lens had a focal length of 50 mm with diameter 38 mm. The focused spot size of the THz beam was about 0.5 mm. Metal foils were placed at the entrance and exit faces of the waveguide to ensure that no stray THz radiation reaches the detector.

4.3.3 THz Propagation Considerations through HCWs

The optical principles that govern the transmission characteristics of hollow core waveguides are somewhat different from that of solid-core fibers due to their typical structures. The following sections briefly describe these typical characteristics of hollow core waveguides based on the work done by Marcatilli and Schmeltzer in 1964[163] and Miyagi in 1980s[164, 165].

4.3.3.1 Attenuation. Attenuation, or power loss, as light travels a distance L, through a material, can be measured in terms of the fractional power lost in transit. In particular for metal coated hollow core fibers, the attenuation is principally caused by surface impedance at the air-metal interface which is accentuated by the fact that at present range of frequencies, the attenuation coefficient ($K \approx 10^2$) is very high[166]. This physical origin is straight forward to understand why in general, the circular electric modes TE_{nm} have the lowest loss in metallic hollow core waveguides while the circular magnetic TM_{nm} and hybrid modes HE_{nm} are rapidly attenuated for even the shortest wavelengths. In fact, the lowest loss mode is the TE_{01} mode which travels parallel to the walls of the guide and has a very tight energy spread centered round the axis of the hollow core waveguide. Other sources of signal attenuation during guided propagation comes purely from experimental considerations such as atmospheric losses in the air core, coupling losses due to launching misalignment, scattering losses due to surface roughness of the waveguide wall and other effects.

Theoretically, the attenuation in hollow metallic and dielectric waveguides for long wavelengths was calculated by Marcatilli and Schmeltzer in 1964[160] where they show that a metal coated circular cylindrical hollow straight guide will have the lowest loss for TE_{01} mode given by,

$$\alpha_{lm} = \left(\frac{u_{lm}}{2\pi}\right)^2 \frac{\lambda^2}{a^3} \mathrm{Re}\left(\frac{1}{\sqrt{(\tilde{n}(\nu))^2 - 1}}\right) \tag{4.1}$$

where u_{lm} is the m^{th} root of the Bessel function, a is the bore radius; λ is the wavelength and $\tilde{n}(\nu)$ is the frequency dependent complex refractive index of the metal. For TE_{01} mode, $u_{lm} = 3.832$ and therefore one obtains,

$$\alpha_{lm} = \frac{33.476}{v^2}\left(\frac{\sqrt{n(v)^2 - k(v)^2 - 1}}{n(v)^2 + k(v)^2 - 1}\right)[in \quad m^{-1}]$$
$$= \frac{145.386X10^4}{v^2}\left(\frac{\sqrt{n(v)^2 - k(v)^2 - 1}}{n(v)^2 + k(v)^2 - 1}\right)[in \quad dB/m] \tag{4.2}$$

where v is the frequency in THz and n and k are the real and imaginary part of the complex refractive index $\tilde{n}(v)$ such that, $\tilde{n}(v) = n(v) + ik(v)$.

4.3.3.2 Dispersion in Waveguide. An optical signal becomes increasingly distorted as it travels along a waveguide due to the mechanisms of intermodal and intramodal dispersion caused by different group velocities of different modes and due to explicit dependence of the core-cladding refractive indices on wavelength[167]. Essentially, the dispersion causes different wavelengths to propagate along the fiber with different travel time which causes broadening of the pulse at output end. Therefore, for all practical applications, dispersion characteristics of waveguide propagation is extremely important from design perspective and these phenomena can be explained by considering the group velocity of the propagating waves inside a waveguide of particular geometry and material.

- **Intermodal Dispersion:** Intermodal dispersion is present whenever more than one mode is excited in a waveguide. In that case, the different modes travel along different paths with different reflection angles at the core/cladding boundary resulting in broadening of the pulse. This is measured as the difference in travel time between the longest (L_1) and shortest (L_2) paths and for hollow core waveguide is given by,

$$\tau_m = \frac{n_1}{c}(L_1 - L_2) \tag{4.3}$$

  where the refractive index of the core $n_1=1$ for hollow core metallic waveguides. However, for the waveguide under study (straight 2mm bore Copper coated hollow polycarbonate waveguide), this dispersion can be neglected as the principal mode that is excited in the waveguide in the present launch conditions is the TE_{01} mode which is also the lowest loss mode.

- **Intramodal Dispersion:** Even in single mode operation, as an optical signal propagates along the guide, each spectral component (the incident pulse is centered about a mean wavelength), undergoes a time delay t_g per length L of the waveguide and is given by,

$$t_g = \frac{L}{c}\left(\frac{d\beta}{dk}\right) = -\left(\frac{\lambda^2 L}{2\pi c}\right)\left(\frac{d\beta}{d\lambda}\right) \tag{4.4}$$

where $k=2\pi/\lambda$ is the free space wave vector and β is the propagation constant. Correspondingly, assuming that the THz source has a finite spectral width, the factor,

$$D = \frac{1}{L}\left(\frac{dt_g}{d\lambda}\right) = \left(-\frac{1}{2\pi c}\right)\left[2\lambda\frac{d\beta}{d\lambda} + \lambda^2\frac{\partial^2\beta}{\partial\lambda^2}\right] \tag{4.5}$$

is then defined as intramodal dispersion and is usually measured in units of ps/mm-cm. In general, D consists of contributions from both the core material referred to as material dispersion (involving $dn_1/d\lambda$) and from the guiding aspects of internal reflection referred to as waveguide dispersion (involving $d\theta/d\lambda$). Material dispersion is obtained by assuming that there is no waveguide dispersion and it occurs whenever the refractive index of the core composition is a nonlinear function of λ. For a specific mode propagating within the waveguide, the angle of reflection θ is a function of wavelength due to the wavelength dependent propagation constant β. This variation in β produces a wavelength dependent time delay τ_{wg} along a waveguide length L as the wavelength spans the spectral width $\Delta\lambda$ of the source. The resulting ratio,

$$D_{wg} = \frac{\tau_{wg}}{L\Delta\lambda} \tag{4.6}$$

is a measure of the waveguide dispersion.

4.3.4 Extraction of Attenuation and Dispersion of HCWs from Experimentation

Time resolved THz spectroscopic measurements provide simultaneous information about the amplitude and phase of the samples under study. One reference waveform $E_{ref}(t)$ is measured without the waveguide and when the lenses moved to their confocal positions, and a second measurement $E_{sample}(t)$ is performed, in which the THz radiation propagates through the waveguide, when the waveguide is placed at the foci of the two lenses. The

amplitude transmittance is calculated by performing a Discrete Fourier Transform (DFT) of the sample and reference measurements.

4.3.4.1 Experimental Determination of Attenuation. The experimentally obtained attenuation coefficient of the HCWs is calculated as,

$$\alpha\left(\frac{dB}{m}\right)=\frac{10\log_{10}\left[P(0)/P(L)\right]}{L(m)} \tag{4.7}$$

where *P(0)* and *P(L)* are the total power transmission without and through the waveguide of length L in meter. This attenuation is equivalent to the theoretical attenuation expressed in Equation 4.2.

The coupling loss was estimated by using cut-back method where a long waveguide was "cut back" to smaller lengths and the data points for specific losses were extrapolated for zero length of the waveguide to obtain the coupling loss in dB. However, since this coupling loss is a function of frequency and the THz source used was broadband, coupling losses at different frequency points was measured for a better adjustment in the final value of the attenuation coefficient of the waveguide arising out of modal loss due to surface impedance.

Additionally, there is attenuation of THz radiation due to water vapor absorption as the set-up has not been purged with nitrogen during the experimentation. This effect has not been accounted for in the present analysis in the present range of analysis from 0.2 THz to 1.2 THz. This limitation does not affect the estimation of the waveguide loss significantly in the lower THz frequencies below 1.2 THz. As can be seen from the Figure 4.1, the atmospheric attenuation does not cross the 3 dB mark, except at 0.56 THz, 0.78 THz, 1.13 THz and 1.19 THz. Therefore, any oscillations in the attenuation values

near these frequencies should not be considered to be true values, but rather local instabilities arising out of unequal water vapor absorptions of the THz radiation (dependent on the relative humidity of the surrounding at a specified time) at different cases, that is, without and with waveguide.

4.3.4.2 Experimental Determination of Dispersion. To extract the dispersion of the waveguide, the propagation constant β of the guided pulse is calculated. Equating the phase of the reference pulse and the pulse through the waveguide of length L, that are detected at the THz receiver, one obtains,

$$\begin{aligned} \phi_0 - kL &= \phi - \beta L \\ \beta &= \frac{2\pi\nu}{c} + \frac{\Delta\phi(v)}{L} \end{aligned} \tag{4.8}$$

where $k = 2\pi v/c$ is the free space propagation constant; v is the frequency; ϕ_0 and ϕ are the phase of the pulse without and with the waveguide, respectively, so that

$$\frac{d\beta}{dv} = \frac{2\pi}{c} + \frac{\Delta\phi'(v)}{L} \tag{4.9}$$

and hence the total pulse broadening over the entire waveguide becomes

$$\tau = L\frac{d\beta}{dv} = \frac{2\pi L}{c} + \Delta\phi'(v) \tag{4.10}$$

Also, from the work of Marcatilli and Schmeltzer[160], the phase constant for TE_{01} mode of the hollow core waveguide is found to be,

$$\beta_{lm} = \frac{2\pi}{\lambda}\left\{1 - \frac{1}{2}\left(\frac{u_{lm}\lambda}{2\pi a}\right)^2\left[1 + \mathrm{Im}\left(\frac{\lambda}{\pi a\sqrt{\tilde{n}(v)^2 - 1}}\right)\right]\right\} \tag{4.11}$$

where u_{lm} is the m^{th} root of the Bessel function, a is the bore radius; λ is the wavelength and $\tilde{n}(v)$ is the complex refractive index of the metal. For TE_{01} mode, u_{lm} = 3.832 and therefore one obtains,

$$\beta_{lm} = \frac{2\pi v}{c} - \frac{c}{4\pi v}\left(\frac{u_{lm}}{a}\right)^2 - \frac{2\sqrt{2n(v)k(v)}}{a(n(v)^2 + k(v)^2 - 1)} + \frac{\sqrt{2n(v)k(v)}}{v^2 a^3 (n(v)^2 + k(v)^2 - 1)}\left(\frac{u_{lm}c}{2\pi}\right)^2 \quad (4.12)$$

A direct comparison of this theoretically predicted phase constant by Equation 4.12 with the equivalent quantity given by Equation 4.8 reveals that the experimentally obtained phase difference $\Delta\phi$ is expected to have a frequency variation. Therefore, the pulse broadening would be,

$$\tau = \frac{2\pi L}{c} + \frac{Lc}{4\pi v^2}\left(\frac{u_{lm}}{a}\right)^2 - \frac{2L\sqrt{2n(v)k(v)}}{v^3 a^3 (n(v)^2 + k(v)^2 - 1)}\left(\frac{u_{lm}c}{2\pi}\right)^2 + term \quad of\left(\frac{dn}{dv}, \frac{dk}{dv}\right) \quad (4.13)$$

A direct comparison of Equation 4.13 with Equation 4.10 reveals that the experimentally obtained derivative of phase difference $\Delta\phi'$ is expected to have positive and as well negative values, where the contribution of the negative dispersion comes from the material characteristics, that is, from 2nd and 3rd terms. Therefore,

$$\Delta\phi'(v) = \frac{Lc}{4\pi v^2}\left(\frac{u_{lm}}{a}\right)^2 - \frac{2L\sqrt{2nk}}{v^3 a^3 (n^2 + k^2 - 1)}\left(\frac{u_{lm}c}{2\pi}\right)^2 + term \quad of\left(\frac{dn}{dv}, \frac{dk}{dv}\right) \quad (4.14)$$

The first derivative of the total pulse broadening with respect to frequency is proportional to the waveguide dispersion coefficient, which is given by,

$$D_{wg} = -\frac{\Delta\tau}{cL\Delta v}v^2 = \frac{d\tau}{dv}\Delta v\frac{v^2}{cL\Delta v} = -\frac{v^2\Delta\phi''(v)}{cL} \quad (4.15)$$

where L is in cm and c, the speed of light is taken in mm/s to obtain an appropriate unit of ps/cm-mm for the dispersion coefficient for hollow core waveguides in the present spectral range. This quantity thus, in other words, gives the amount of the pulse

broadening in the units of picosecond per cm (length of the waveguide) per millimeter (spectral width of the THz source).

4.3.5 Optical Parameters for Metal Coating of HCWs

Not many experimental studies are performed in far IR region on metals[168, 169, 170, 171] and therefore it is difficult to obtain optical data, especially refractive index, attenuation coefficient etc. in THz region. For the present study, to evaluate the attenuation and dispersion theoretically, both n and k values of Cu as a function of THz frequencies are required. To extract these values for the metallic coating of Cu, a Drude Model fit is employed using the fitting parameters obtained near 30 μm wavelengths. Following are the values[165] of plasma frequency, $\omega_p = 6.38 \text{ X } 10^4$ cm^{-1}, damping frequency, $\omega_\tau = 2.78 \text{ X } 10^2$ cm^{-1}; high frequency dielectric constant, $\varepsilon_\infty = 5.27 \text{ X } 10^4$ of Cu which are related through Drude Model as,

$$\varepsilon_1 = \varepsilon_\infty - \frac{\omega_p^2}{\omega^2 + \omega_\tau^2} \quad and \quad \varepsilon_2 = \frac{\omega_p^2 \omega_\tau}{\omega^3 + \omega \omega_\tau^2} \tag{4.16}$$

where ω is the wavenumber in cm^{-1} and n and k are related as,

$$\begin{aligned} n &= \sqrt{\frac{1}{2}\left(\sqrt{\varepsilon_1^2 + \varepsilon_2^2} + \varepsilon_1\right)} \\ k &= \sqrt{\frac{1}{2}\left(\sqrt{\varepsilon_1^2 + \varepsilon_2^2} - \varepsilon_1\right)} \end{aligned} \tag{4.17}$$

The values of n and k obtained through this method are somewhat extrapolated and therefore the values of attenuation and dispersion of the waveguides under study are also approximated to that extent.

4.4 Results

4.4.1 Time Domain Data and Amplitude Spectrum for HCW

THz electric fields of the reference pulse and the HCW of different lengths have been shown in Figure 4.4.

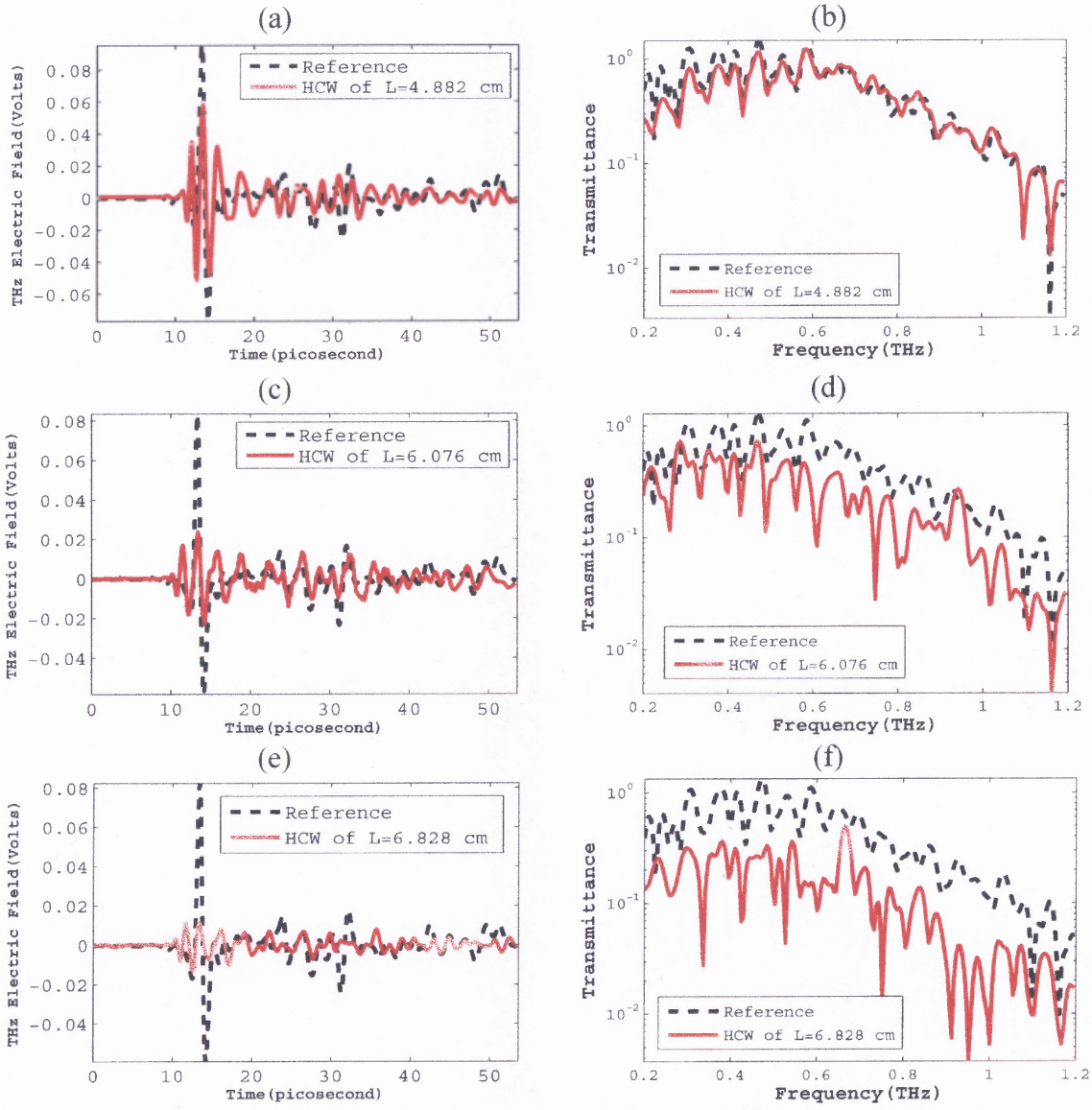

Figure 4.4 (a), (c) and (e) show the time domain reference THz pulses and the propagated pulses through Copper coated polycarbonate hollow waveguide of lengths 4.882 mm, 6.076 mm and 6.828 mm respectively. (b), (d) and (f) show their corresponding relative amplitude transmittance. It should be noted that the phase of the guided pulse through the HCW have been temporally shifted to overlap with the reference pulses for easy comparison in (a), (c), (e). It is also observed that as the length of the HCW was increased, the propagated pulses were attenuated to larger extent.

It could be seen from Figure 4.4 (a), that an input pulse of FWHM (full width at half maximum) 1.4 ps broadens to a pulse of FWHM 6.5 ps after traveling through the waveguide. Hence, the group velocity dispersion (GVD) for the 48.80 mm length waveguide is approximately 2.1 ps/THz·cm at a center frequency of 0.5 THz.

4.4.2 Attenuation Coefficient for HCW

The theoretically obtained values for n and k for Copper using Drude Model Fit are plotted in Figure 4.5 (a). Using these values, the experimentally obtained attenuation coefficient from Equation 4.7 and the theoretically expected attenuation for TE_{01} mode are compared in Figure 4.5 (b). Here the total loss is in dB/m and is corrected for losses associated with coupling. However, the losses due to atmospheric absorption are not corrected for and the apparent anomalies of the attenuation coefficient near 0.56 THz, 0.78 THz, 1.13 THz and 1.19 THz are suspected to be due to water vapor absorption in the unpurged experimental set up for waveguide characterization, as discussed in Section 4.3.4.1.

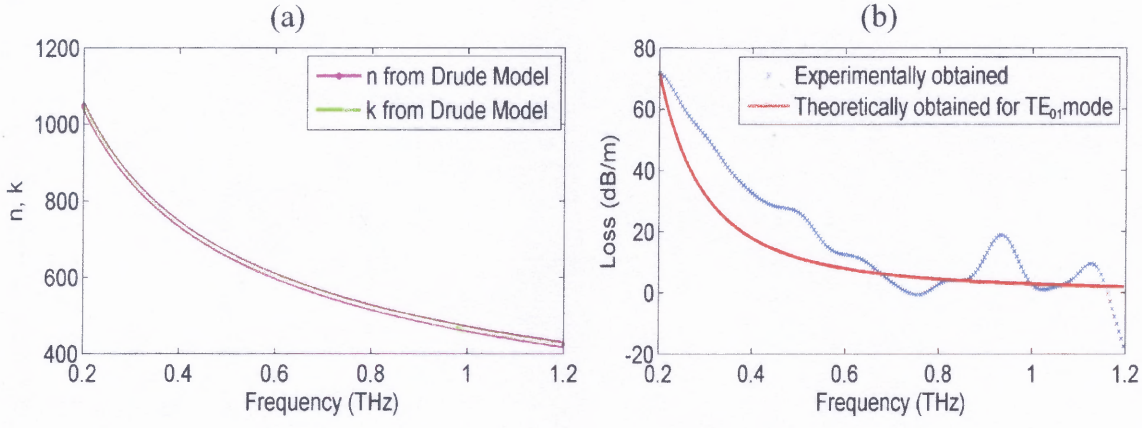

Figure 4.5 (a) Theoretically obtained n and k for Cu using Drude Model Fit; and (b) Comparison of the experimental and theoretical attenuation coefficients in dB/m using the n and k data.

Earlier works[157] on the measurements of attenuation of these HCWs (having bore size of 2 mm with Copper coatings) using CW THz sources had reported a loss of 6.6 dB/m, 6.5 dB/m and 5 dB/m at 1.69 THz, 1.89 THz and 2.53 THz, respectively. From Figure 4.5 (b), it can be seen that the attenuation of the Copper coated hollow core waveguides is 20 dB/m at 0.5 THz. On extrapolation, the attenuation at 1.4 THz can be found to be approximately 7 dB/m which agrees well with earlier reported values on a direct comparison. These attenuation values are also expected to follow this decreasing trend with increasing frequencies. As from Equation 4.1, one can see that the theoretically predicted attenuation is proportional to the square of the wavelengths; or in other words, the attenuation is inversely proportional to the square of the frequencies of the THz pulse.

4.4.3 Dispersion Characterization for HCW

The unwrapped phase of the reference pulse and the guided pulse through fiber length of 4.882 cm are shown in Figure 4.6 (a) as a function of frequency and the corresponding phase difference is plotted in Figure 4.6 (b). The pulse dispersion, which is proportional to the derivative of the phase difference, is plotted in Figure 4.6 (c). It can be seen that the pulse broadening is around 2 ps at 0.5 THz, a fact that has already been reflected from the GVD calculation obtained from the time domain data.

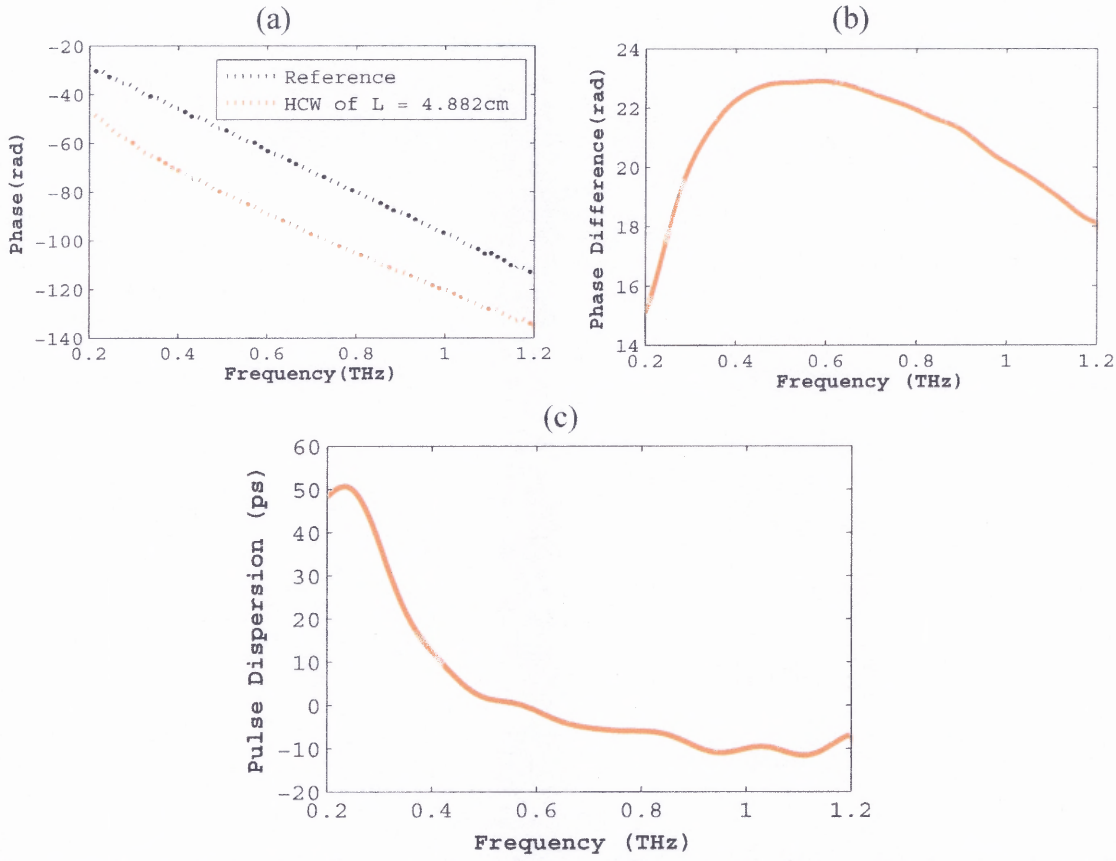

Figure 4.6 (a) shows the phase of the reference THz pulse and the guided pulse through the hollow core waveguide of length 4.882 cm; (b) shows the corresponding phase difference and (c) shows the pulse broadening in picosecond.

As can be seen from Figure 4.6 (c), the pulse dispersion is negative over a certain range of frequencies, which could be explained on the basis of material dispersion as discussed in Section 4.3.4.2. This conclusively shows that the interaction of the THz electric field with the metal coating is significant not only from attenuation point of view, but also for dispersion management in these kinds of waveguides.

4.5 Conclusions

In the present study, a straight Cu coated hollow core cylindrical waveguide is characterized based on its attenuation and dispersion profile in THz range of frequencies between 0.2 THz to 1.2 THz. However, for a more practical approach, the scope of the present study has to be broadened to include the characterization of different bore sizes, different coating materials and outer layers and at the same time, the losses and mode profile are to be characterized for bent fibers. In the present study, the estimation of both the attenuation and dispersion of the waveguide structure is limited by the approximation of n and k values of the metal coating, which in the present case is Cu. For a more reliable estimation, direct experimental measurements of n and k are required in THz region. Additionally, the effect of water vapor absorption to the loss estimation can be minimized by purging the experimental set-up.

CHAPTER 5

WAVELENGTH SCALABLE TERAHERTZ BAND-REJECT FILTER

5.1 Objectives

Similar to electronic filter, an optical filter enhances the optical signal in a certain frequency range while suppressing the same in other frequency range. In most of the applications, the optical signal of interest has a major contribution from a certain band of frequencies. On the other hand, the noise of an optical system, in general, has some other distinct frequency characteristic than the signal. Therefore, to attain optimal performance of any optical system, such as an optical imager, frequency management through filtering is a very important issue. As many applications in THz region are being developed based on the spectral response of the system including, spectroscopy[172], imaging[173], communication and others, the demand for quasi-optic components such as tunable frequency filters, phase shifters, attenuators and polarizers in the THz range is on the rise. Many existing filtering technologies targeted mainly for the visible and infrared region are unsuitable or difficult to fabricate for THz radiation which is essentially a long wavelength radiation. At the same time, many filtering devices suffer from acute substrate losses in the THz range, adding unwanted device specific frequency signature to the signal.

In this chapter, a simple design of a wavelength-scalable, band reject THz frequency filter using multilayer structure has been proposed in reflection mode. The aim is to design a multilayer structure with p number of layers to obtain a featureless, broadband frequency rejection in reflection over a certain frequency range. This could also be used as a filter in different wavelength range with adjustment of the thicknesses

of the layer with respect to the wavelength. The model is based on Impedance Matching approach which takes into account of the Fabry-Perot effect due to multiple reflections at the boundaries between different layers. Different parametric simulations have been illustrated. Additionally, experimental THz characterization using standard THz Time Domain Spectroscopic (THz-TDS) set-up, are shown for i) 3 metal grid structures having 20, 40 and 55 lines per inch respectively; and ii) different ferrous boride films, which have potential use in THz frequency filtering. This work is particularly motivated to attain THz frequency filtering in THz security imager. As frequency filtering is expected to offer a possibility of reducing the noise in certain band of frequencies (such as background thermal THz noise) and thus improving the overall signal to noise of the imaging system.

5.2 Background

THz pulse shaping in time domain is a field of interest for a long time[174, 175, 176]. However, signal management in THz frequency domain is comparatively a new area of pursuit. Different filtering architecture are being proposed which include frequency filtering based on two-dimensional metallic hole arrays/photonic crystals acting as a bandpass filter[177, 178], binary grating with rectangular grooves[179, 180], plasmonic high pass filter consisting of high aspect-ratio micron-sized wire arrays[181, 182], tunable THz filter based on a GaAs/AlAs multiple quantum well structure[183, 184], metallic photonic crystal filter tunable by a relative lateral shift between two micromachined metallic photonic crystal plates[185, 186]; defect material inserted into a periodic structure of alternating layers of quartz and high-permittivity ceramic[187, 188] and other interesting structures[189, 190, 191].

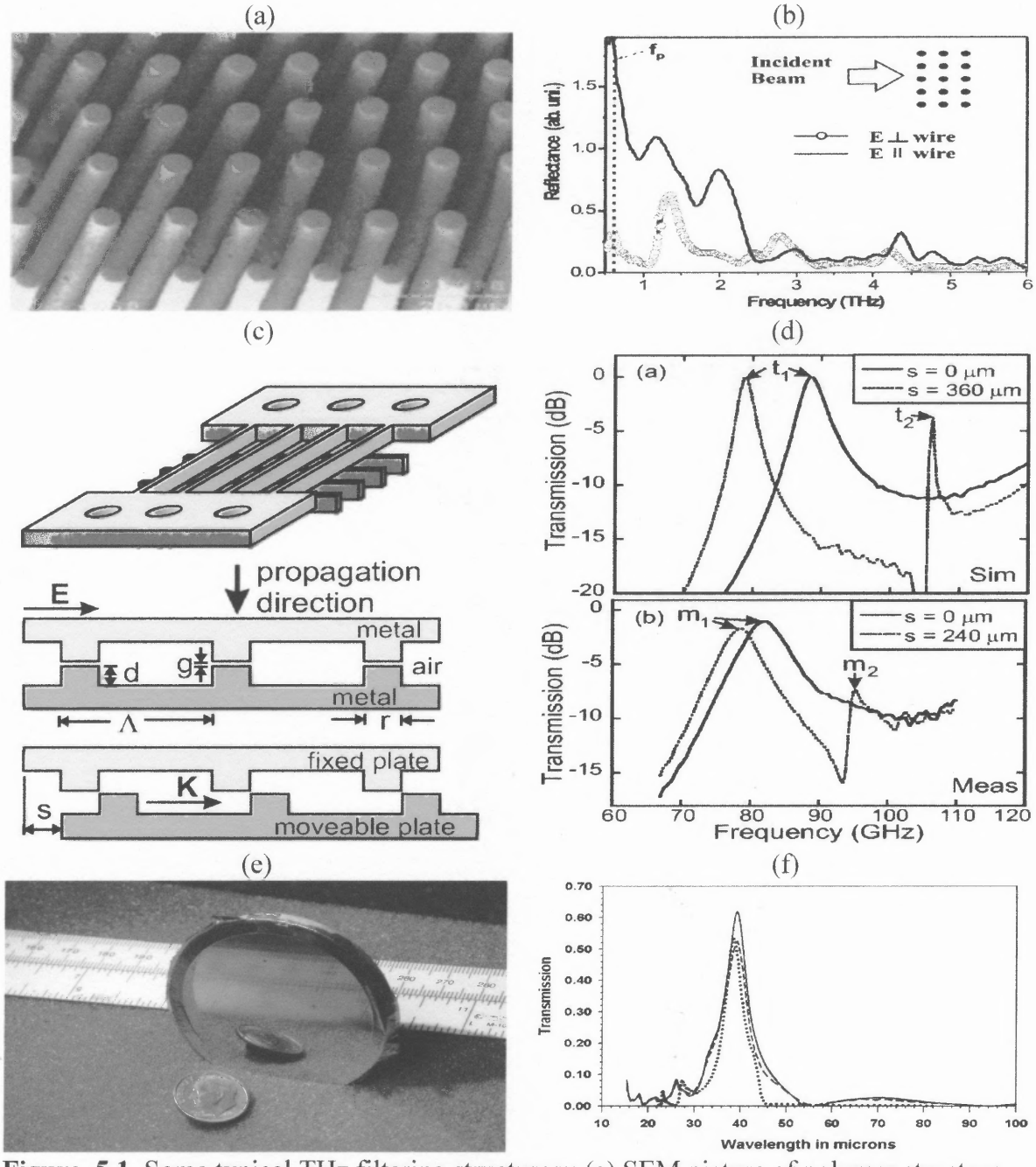

Figure 5.1 Some typical THz filtering structures:: (a) SEM picture of polymer structure before gold coating with a 2D cubic lattice fabricated by advanced microstereo-lithography (lattice constant 120 μm, wire radius 15 μm, wire length 1 mm). The dimension of whole structure is 2.1 X 2.1 X 1 mm^3 and (b) corresponding reflection signal from FTIR measurement[179]; (c) One of two metal plates required to make the filter which is tuned by lateral shift parallel to the inner grid and (d) corresponding frequency spectra showing highest and lowest center frequency for the transmission peak[184]; (e) 38 μm stacked metal lattice filter with (f) Measured and modeled transmission at 5 K (dashed line) and at 298 K (dotted line)[178].

Figure 5.1 shows some of the representative structures used for filtering purpose and their typical frequency response in THz range. However, there is a recent thrust in developing the so called metamatetials[192] which are tailored structures to produce such refractive indices/attenuation coefficients, otherwise unattainable through synthesis of material media. As the THz frequency filtering essentially depends on the optical parameters of the materials of the filtering structures, attaining these seemingly impossible refractive indices/attenuation coefficients has opened up a new field of recent research activities[193, 194].

5.3 Design of the Band-Reject THz Filter

To design a band-reject filter having a stack of layers of different materials, an estimation of the refractive indices and thicknesses of the different layers are required which minimize the reflectivity over a particular frequency range and angle of incidence. For this purpose, it is better to approach Impedance Matching (IM) technique instead of the ray analysis as the IM technique directly relates to the optical parameters (n, μ, ε) of the materials involved which could be frequency dependent and can describe the energy transfer of polarized radiation incident at any angle on the structure. On the other hand, the ray analysis (or the transfer matrix) method, inherently restricts angular variation as it makes the following assumptions, that is $sin\theta \cong tan\theta \cong \theta$, where θ is the incident angle. In other words, the radiation has to be incident normally or very close to normal, which is not always practical for real life applications. However, the transfer matrix method is much easier to implement in terms of calculations than impedance matching.

5.3.1 Impedance Matching Approach

Optical Impedance of a medium is defined as the ratio between the transverse electric field and transverse magnetic field, that is, $Z = \frac{E_{transverse}}{H_{transverse}} = \sqrt{\frac{\mu_0 \mu_r}{\varepsilon_0 \varepsilon_r}}$, where μ_0 and ε_0 are the permeability and the permittivity of vacuum, respectively and μ_r and ε_r are the respective quantities in the medium. This impedance is equivalent to electrical impedance which a flow of alternating electrical energy experiences through an electrical medium. Similarly a radiation, which essentially is an alternating electric and magnetic field, experiences the same impedance through an optical medium. However, when radiation is incident on an interface between two materials having different impedances, then the amount of optical energy that gets reflected and transmitted, is related to the impedances of both the materials under concern. At the same time, the changes in the polarization state which results when the radiation passes through an optical system, can also be directly calculated from the impedance of such a system. Therefore, for a composite optical structure, one needs to apply the approach of impedance matching which directly relates to the matching of the effective impedance of all the interfaces in such a structure to find out the total reflection or transmission of the incident radiation by such a system.

5.3.2 The Formalism

Considering a three layer structure as shown in Figure 5.4 (a), the effective impedances of media 1, 2 and 3 are[195],

$$\left.\begin{aligned} Z_1' &= Z_1 \cos\theta_1 = Z_0 \cos\theta_1 / n_1 \\ Z_2' &= Z_2 \cos\theta_2 = Z_0 \cos\theta_2 / n_2 \\ Z_3' &= Z_3 \cos\theta_3 = Z_0 \cos\theta_3 / n_3 \end{aligned}\right\} \qquad (5.1)$$

where, θ_1 is the incident angle on the boundary between the media 1 and 2 with complex refractive indices n_1 and n_2, respectively; θ_2 and θ_3 are refracted angles in media 2 and 3 with complex refractive indices n_2 and n_3, respectively; and d is the thickness of medium 2. It can be shown that the reflection and transmission coefficients of the structure are exactly the same as shown in Figure 5.2 (b) for normal incidence where the effective thickness of layer 2 is given by $d'=d\cos\theta_2$ and effective impedances of media 1, 2 and 3 becomes Z_1', Z_2', Z_3' respectively.

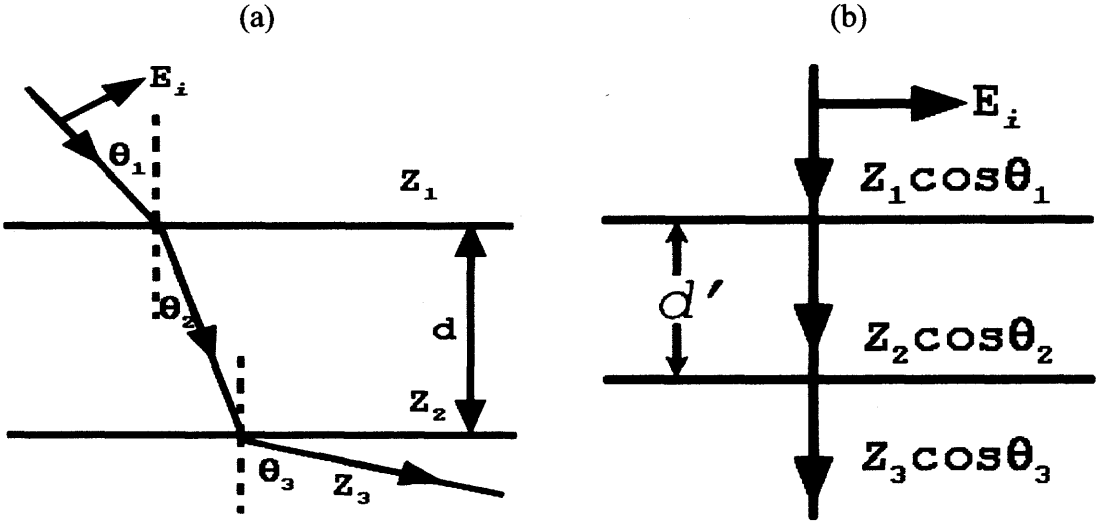

Figure 5.2 Waves passing through a dielectric slab of thickness d; (a) waves incident at a finite angle with normal being refracted and transmitted and (b) normal impedance structure equivalent to (a).

Thus, the transformed impedance of medium 3 at the boundary between medium 1 and medium 2 is,

$$Z_3^{int1,2} = Z_2' \left(\frac{Z_3' \cos k_2 d' + i Z_2' \sin k_2 d'}{Z_2' \cos k_2 d' + i Z_3' \sin k_2 d'} \right) \tag{5.2}$$

where $k_2=2\pi n_2/\lambda_0$.

Essentially, the aim is to calculate how medium 3, medium 4 and so on and so forth would affect the reflection and transmission at the very first interface, that is, instead of considering all these interfaces, one has to consider an effective two layer structure with certain effective impedance.

The reflectivity, ρ of the above structure is given by,

$$\rho = \frac{Z_3^{"} - Z_1^{'}}{Z_3^{"} + Z_1^{'}} \tag{5.3}$$

and therefore the reflectance is given by $R = |\rho|^2$.

5.3.3 Assumptions of the Current Model

Following are the assumptions of the current model under consideration;

- The incident wave is *p*-polarized, that is, $\vec{E}$ lies in the plane of incidence.
- Faces of the layers (slabs of the stack under consideration) are flat and parallel.
- The light source is coherent.
- $\mu_1 = \mu_2 = \mu_3 = \mu_4 \approx 1$ (the materials are non-magnetic).
- The electromagnetic responses of all the media are linear.

The first assumption is made for the convenience of calculation. If the polarization state is intermediate, then one has to account for both r_p and r_s components separately and then sum them up through effective impedance matching at the interfaces for both *p* and *s* polarizations separately, which complicates the calculation. The incident polarization state is, therefore, taken to be *p*-polarized, which is also the polarization state of the experimental set-up used for characterization of the THz filtering structures. The

next two assumptions ensure that the effect of scattering is minimal and hence can be neglected. In an optical structure which causes strong scattering, the effective impedance of the same becomes strongly direction dependent (that is, dependent on the scattering angles) and the following calculation becomes cumbersome. The fourth approximation is generally true for most of the materials, except for magnetic materials with finite magnetic permeability. These assumptions are made for a simple implementation of the method of transformed impedances[196] to calculate the transmission/reflection. In case of anisotropic magnetic materials, the impedances calculations get further complicated by the presence of surface charges at the interfaces. However, the present model can account for magnetic media in the multistack structures by incorporating the effect of the same in the calculation of the corresponding impedances at particular interfaces. Finally, the last assumption is made to design a linear optical structure which does not depend on the incident electromagnetic intensities of the radiation.

5.3.4 The Model

Using the concept expressed in Equation 5.2 and Equation 5.3, the effective impedance between any two media of a p-layered multistack is evaluated as,

$$Z_{effective}^{(\alpha,\beta,\gamma)} = \frac{Z_{(\alpha,\gamma)}\left(\frac{Z_{effective}^{(\alpha+1,\beta,\gamma)}\cos kd_{opt}^{(\alpha,\beta,\gamma)} + iZ_{(\alpha,\gamma)}\sin kd_{opt}^{(\alpha,\beta,\gamma)}}{Z_{(\alpha,\gamma)}\cos kd_{opt}^{(\alpha,\beta,\gamma)} + iZ_{effective}^{(\alpha+1,\beta,\gamma)}\sin kd_{opt}^{(\alpha,\beta,\gamma)}}\right)}{1-\left(\frac{\tilde{n}_{(\alpha)}-\tilde{n}_{(\alpha-1)}}{\tilde{n}_{(\alpha)}+\tilde{n}_{(\alpha-1)}}\right)\left(\frac{\tilde{n}_{(\alpha)}-\tilde{n}_{(\alpha+1)}}{\tilde{n}_{(\alpha)}+\tilde{n}_{(\alpha+1)}}\right)\exp\left[-i\frac{4\pi\tilde{n}_{(\alpha)}\nu_{(\beta)}d_{opt}^{(\alpha)}}{c}\right]} \quad (5.4)$$

where α goes from 1 to p; β goes from 1 to f where f is the number of frequencies on the frequency axis; γ goes from 1 to t where t is the number of incident angles on angle axis;

ν is the frequency and c is the speed of light in vacuum. In this expression, $d_{opt}^{(\alpha)}$ is the optical thickness of α-th layer such that,

$$d_{opt}^{(\alpha)} = \frac{\lambda}{\tilde{n}_{(\alpha)}} d_{actual}^{(\alpha)} \tag{5.5}$$

where $d_{actual}^{(\alpha)}$ is the actual thickness of the α-th layer without any unit; λ is the center wavelength of the frequency range of interest and $\tilde{n}_{(\alpha)}$ is the complex refractive index of α-th layer such that, $\tilde{n}_{(\alpha)} = n_{(\alpha)} + i\kappa_{(\alpha)}$ where $n_{(\alpha)}$ and $\kappa_{(\alpha)}$ are the real part and imaginary part (or attenuation coefficient) of the of the complex refractive index of the α-th layer, respectively. Also one other important point that is to be noted about Equation 5.4 is that the term in the denominator is solely due to the Fabry-Perot effect (that is, multiple forward and backward reflections between adjacent layers)[197].

5.4 Experimental THz Characterization of Different Structures

5.4.1 THz-TDS Characterization of Metal Grid Structures

A set of three square shaped screens (metal grid structures prepared at Electronic Imaging Center, Dept. of Electrical Engineering at NJIT by the group led by Dr. Haim Grebel) with 20, 40 and 50 lines/inch have been investigated in the frequency range of 0.1 to 1.0 THz (3 to 33 cm^{-1} in wavenumbers). Using a T Ray-2000™ THz Spectroscopic system (which essentially is a standard THz Time Domain Spectroscopic set-up) a time domain THz signal is obtained over a total of 80 ps sweeps with 0.078125 ps wait time for all of the filters and reference scans. The reference used is a circular aluminum aperture of

diameter ~ 0.7 cm to ensure normalization in THz transmission through all the screens. The spot size (beam diameter) of the collimated THz beam from the transmitter is ~ 2 cm with a nominal divergence angle of less than 10 mrad . The screens are placed normally to the incident THz beam.

The THz transmittance in frequency domain is obtained after implementing Fast Fourier Transformation (FFT, which is obtained using 2048 points with zero-padding) to the time domain data. The transmittance is defined as following,

$$\tilde{T}_{\exp}(\nu) = \frac{\tilde{E}_{sample}(\nu)}{\tilde{E}_{ref}(\nu)} \tag{5.6}$$

where $\tilde{E}_{sample}(\nu)$ and $\tilde{E}_{ref}(\nu)$ are the complex THz electric field (containing both amplitude and phase information) through the screens and references, respectively in frequency domain.

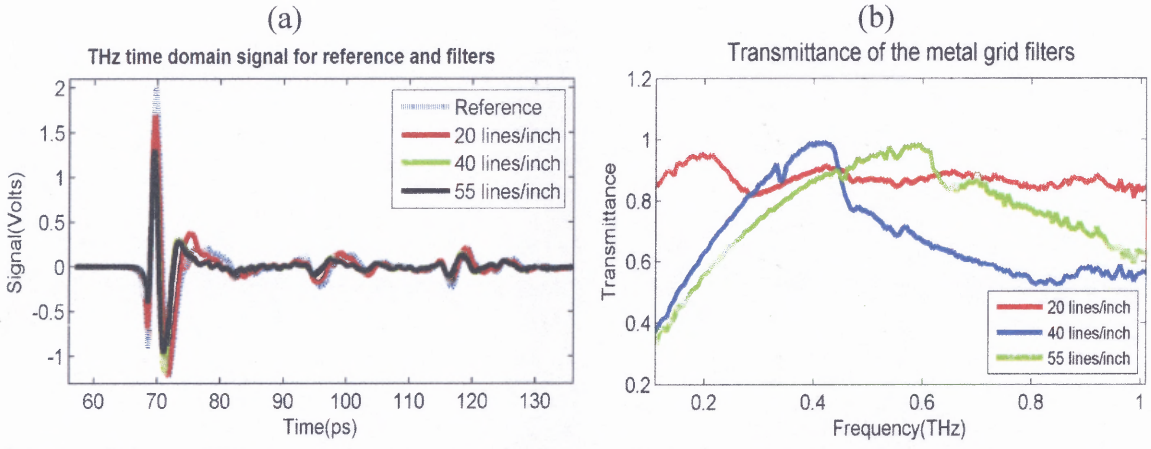

Figure 5.3 (a) THz time domain signal of the reference aperture and the square metal grid screens with 20, 40 and 50 lines/inch; and (b) corresponding THz transmittance of the same showing the filtering properties of the screens in the frequency range of 0.1 to 1.0 THz.

Figure 5.3 (a) shows the time domain experimental plots. Correspondingly, Figure 5.3 (b) shows the transmission peaks for the metal screens which are observed at 0.2 THz, 0.42 THz and 0.59 THz (or 6.7 cm^{-1}, 14.0 cm^{-1} and 19.7 cm^{-1} in wavenumbers) for the grids with 20, 40 and 50 lines/inch, respectively. The theoretical resonance frequencies of these structures were found to be at 0.2034 THz, 0.4068 THz and 0.5593 THz, respectively[198]. The transmission data is truncated at 1.0 THz as the transmission is found to be oscillating strongly at the water vapor lines of THz at 1.13 THz, 1.18 THz, 1.43 THz and so on as the system was not nitrogen purged.

5.4.2 THz-TDS Characterization of Ferrous Boride Films

Four Ferrous Boride (containing either FeB or FeB_2 or both in different concentrations) films (samples are prepared at Dept. of Physics, Material Science and Engineering Program, NJIT by the group led by Dr. Roumiana Petrova) are investigated in the frequency range of 0.1 to 1.0 THz (3 to 33 cm^{-1} in wavenumbers). Using the T Ray-2000™ THz system with the initial optical delay of 104.96 ps and 0.078125 ps wait time and an averaging of 20 sweeps per scan, the effective bandwidth of the system with High Density Polyethylene lenses is found to be ~ 1.8 THz. These convex lenses of focal length 60 mm were used to focus the collimated THz beam of diameter ~ 2 cm to a spot size of ~ 4 mm.

The sample holder used during the experimentation is an aluminum aperture of diameter ~ 0.7 cm. Reference 1 is two layers of scotch tape with thickness 0.15 mm and was used as sample holders for Sample 1, Sample 2 and Sample 3 with thickness of 0.19 mm, 0.30 mm and 0.33 mm, respectively. Reference 2 is two layers of scotch tape with

thickness of 0.22 mm which was used as the sample holder for Sample 4 of thickness 0.56 mm.

The FFT is done using 2048 points to obtain THz transmittance as defined in Equation 5.6. The transmission data is again truncated at 1.0 THz similar to the previous case, as the transmission is found to be oscillating strongly at the water vapor lines of THz at 1.13 THz, 1.18 THz, 1.43 THz and so on as the system was not nitrogen purged. In the frequency range of 0.1 THz to 1.0 THz, the references are found to be featureless. To extract the optical parameters, following expression is used,

$$\left.\begin{aligned} n(\nu) &= \left[1 - \frac{c}{2\pi\nu l}\arg\left(\tilde{T}_{\exp}(\nu)\right)\right] \\ k(\nu) &= \frac{c}{2\pi\nu l}\ln\left[\frac{(n(\nu)+1)^2}{4n(\nu)}\left|\tilde{T}_{\exp}(\nu)\right|\right] \end{aligned}\right\} \tag{5.7}$$

where $\tilde{T}_{\exp}(\nu)$ is obtained using Equation 5.6, l is the thickness of the sample; ν is the frequency and c is the speed of light in vacuum. This expression is obtained by equating the modulus (amplitude) and argument (phase) parts of the Fresnel reflection/transmission coefficients separately at the air/sample/air interfaces[197].

Figure 5.4 (a) shows the experimentally obtained THz time domain signal of the references and four different samples of Ferrous Borides, while Figure 5.4 (b) shows the corresponding transmittance. Figure 5.4 (c) and Figure 5.4 (d) show the real part and the imaginary part of the complex refractive index extracted from the experimental transmittance using Equation 5.7.

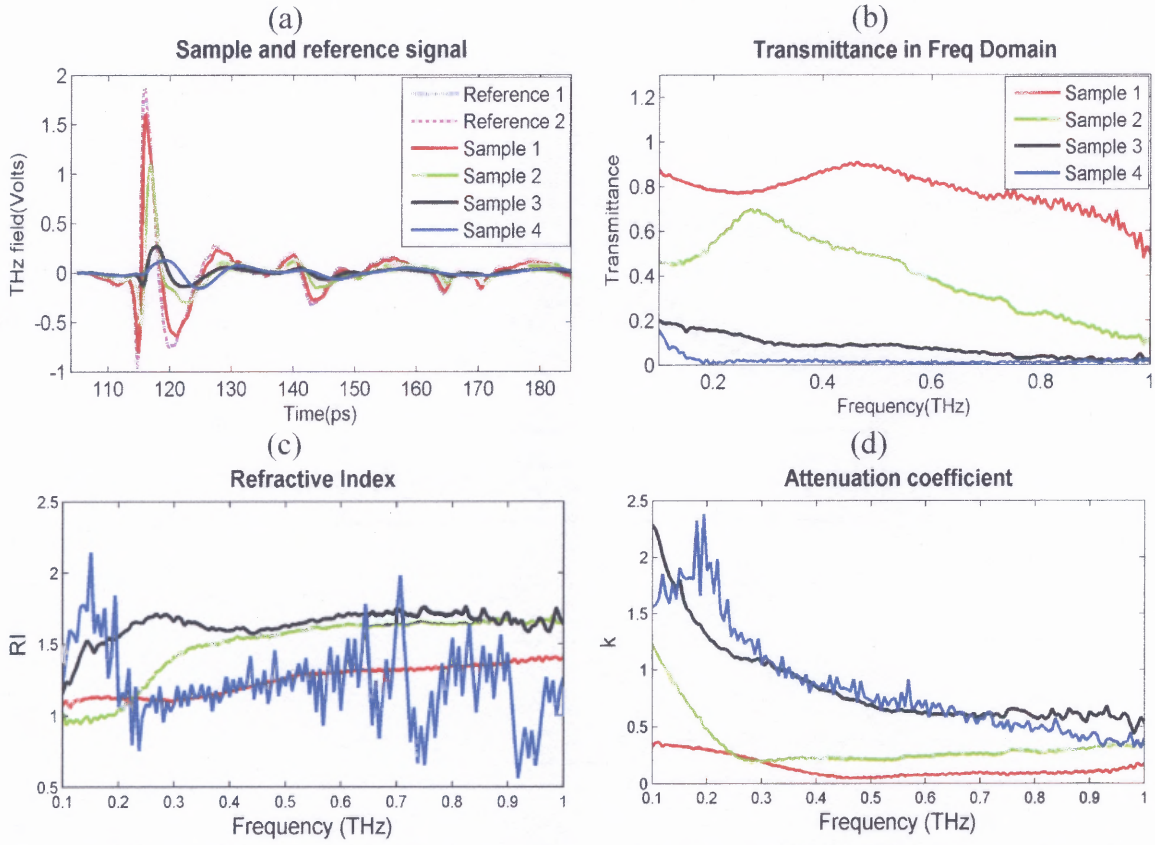

Figure 5.4 (a) THz time domain signal of the references and four different samples of Ferrous Borides; (b) corresponding THz transmittance of the same; (c) extracted optical refractive indices of the samples under study from the phase data and (d) the attenuation coefficient of the samples.

5.5 Simulation of THz Filter Structures

Using Equation 5.4 and Equation 5.3, different multilayer structures are designed to simulate THz filtering in reflection mode over the frequency range of 0.1 THz to 1.0 THz. In these simulations, the input parameters are the number of layers to be used in the stack, frequency dependent real part of the refractive indices, $n(\nu)$ and frequency dependent imaginary part of the refractive indices, $k(\nu)$ of all those individual layers in the specified frequency range. To obtain minimum reflectance of the structures, the thicknesses of the layers are adjusted automatically by the program made in MATLAB.

This corresponds to the value of $d = \frac{\lambda}{4n}$ (like thickness of an anti-reflective coating). Figure 5.5 shows a simulated multilayer structure of 5 layers based on the Ferrous Boride samples studied in the previous section.

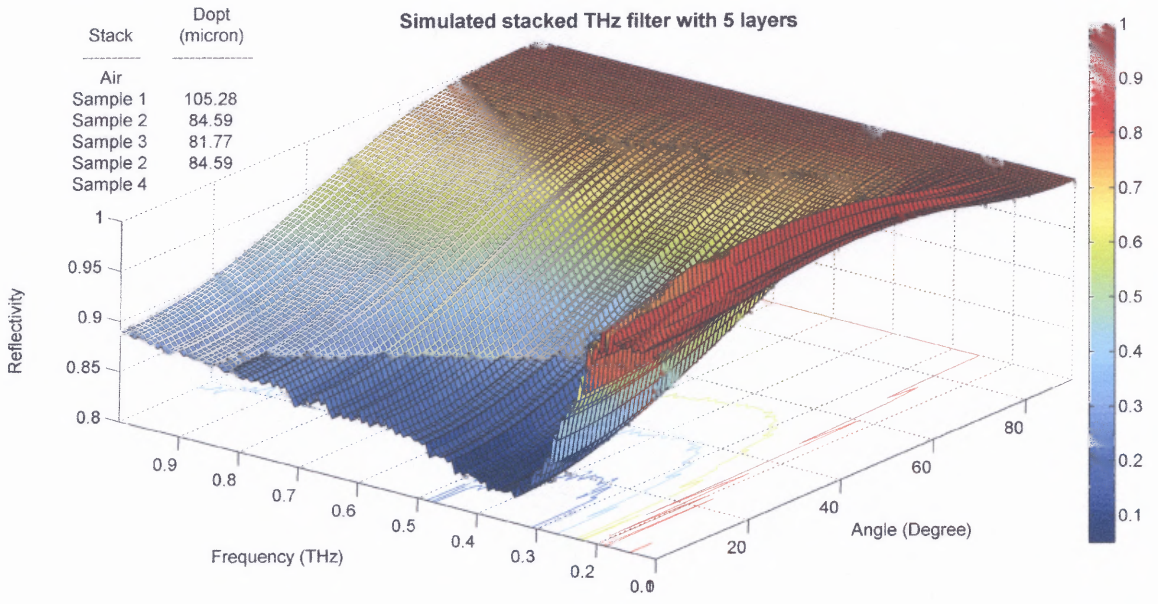

Figure 5.5 A simulated multilayer structure of 5 layers based on the Ferrous Boride samples showing the predicted reflectance as a function of frequency and incident angles.

This shows the predicted reflectance, *R* of the structure as a function of frequency and incident angles. The reflectance of the structure could be seen to be high (the lowest reflectance is 0.83 at 0.38 THz at an incident angle of 0 degree with the normal) at all incident angles other than normal which indicates a very narrow numerical aperture for this filtering structure. This suggests a poor performance of frequency filtering for this design.

Using the same program, some other multilayer structures were also simulated based on some of the representative materials such as, Silicon, Silicon-dioxide, quartz, Silicon nitride, Aluminum oxide, metallic Aluminum and others.

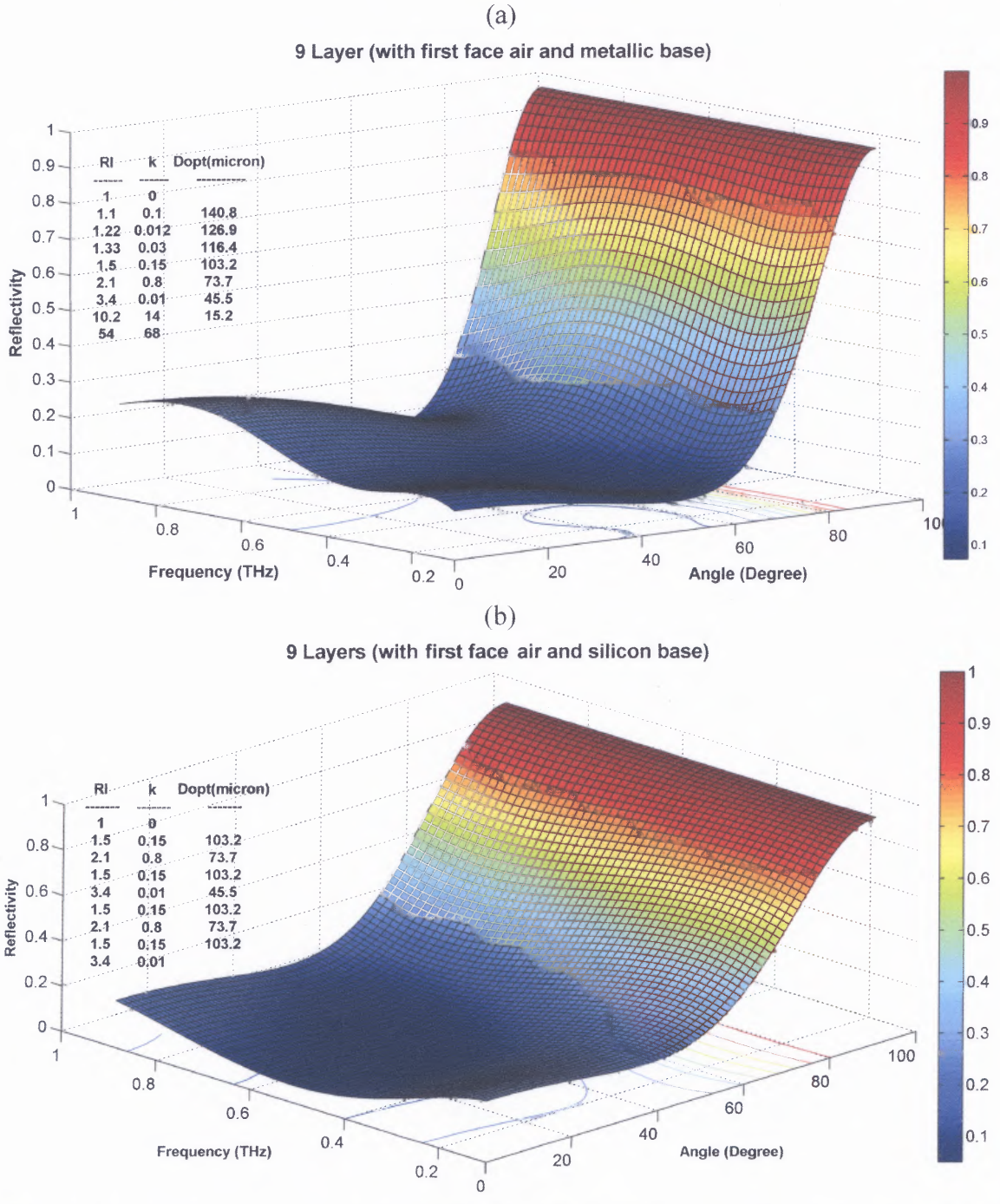

Figure 5.6 Simulated multilayer structures of 9 layers with (a) metallic substrate and (b) silicon substrate which show the predicted reflectance as a function of frequency and incident angles.

Figure 5.6 shows the performance of two simulated multilayer structures of 9 layers with Figure 5.6 (a) showing a structure with metallic substrate and Figure 5.6 (b) showing a structure with silicon substrate. These designs are successful filter structures as the predicted reflectances are very low over a wide range of angle of incidence. However, as these structures use a large number of layers, they might prove to be difficult to fabricate. In all of these structures, the optical parameters of the layers are taken to be dispersionless (that is, the values of n and k are broadband and not dependent on the frequency) as the $n(\nu)$ and $k(\nu)$ of the materials are extracted from experimental THz characterization. The variations of the reflectance over the frequency as seen in Figure 5.6 (a) and 5.6 (b) are, therefore, only due to Fabry-Perot effect.

5.6 Conclusions

In this study, modeling of a wavelength-scalable, band reject THz frequency filter using multilayer structure has been shown in reflection mode. The model of the filter design based on Impedance Matching approach taking into account of the Fabry-Perot effect produces different parametric simulations. The multistack of 5 layers, using the experimentally characterized samples of Ferrous Boride as individual layers, shows poor performance in frequency filtering. While the metal grid filters show good performance of frequency filtering but only with a very narrow band (that is, around the resonance frequencies of the grid structures). Additionally, design of multistacks with large number of layers show promise, suggesting that to design a multilayer structure to obtain a featureless, broadband frequency rejection in reflection over a certain frequency range, a large of number layers with variation in both refractive indices and attenuation

coefficients are to be used. This might be challenging from fabrication point of view as only very few materials could be found to be suitable candidates for this application. However, alternatively one can expect that an efficient frequency filtering multilayer structure could be designed using tailored materials such as, metamaterials. For example, photonic crystals with some introduced defects or micromechanically tailored grooves and many others can be considered to be potential candidates for use in such structures. In those cases, since the optical parameters are not only dependent on the intrinsic material properties but also on the physical dimensions of the structures as well, it might be easier to implement the design of a multilayer structure with few numbers of layers.

CHAPTER 6

TERAHERTZ INTERFEROMETRIC IMAGING

6.1 Objectives

The applications of terahertz (THz) radiation are rapidly expanding. In particular, ultrafast THz radiation imaging is emerging as a powerful technique to spatially map a wide variety of objects with spectral features which are present for many materials in THz region. THz frequencies also possess several other notable advantages for imaging. Objects buried within dielectric structures can be imaged using THz radiation due to the transparency of most dielectrics in this regime. Therefore, concealed items having spectral signatures in THz regimes can be identified non-invasively. Moreover, the nonionizing nature of THz radiation permits noninvasive biological imaging as well. Unfortunately, the image quality in these applications is inherently influenced by scattering introduced by the inhomogeneities of the medium, presence of barriers and attenuation due to water vapors and other factors. These factors thus reduce both the transmitted power of the THz signal and the spatial resolution in the image. For continued development in THz radiation imaging, therefore, a comprehensive understanding of the interplay of these factors on image formation is necessary. In all of the previous chapters, some of these aspects were discussed in detail, particularly from the point of view of THz propagation and detection.

In the present chapter, a practical application of THz radiation in the form of a novel imaging method has been described which is currently being developed by THz Spectroscopy and Imaging group at NJIT. It combines the spectral imaging capability of THz waves through characteristic transmission or reflection spectrum of explosive

agents, with interferometric imaging techniques to provide spatial detection of such lethal agents using only a limited number of detectors. Figure 6.1 shows a block diagram of the proposed THz imager.

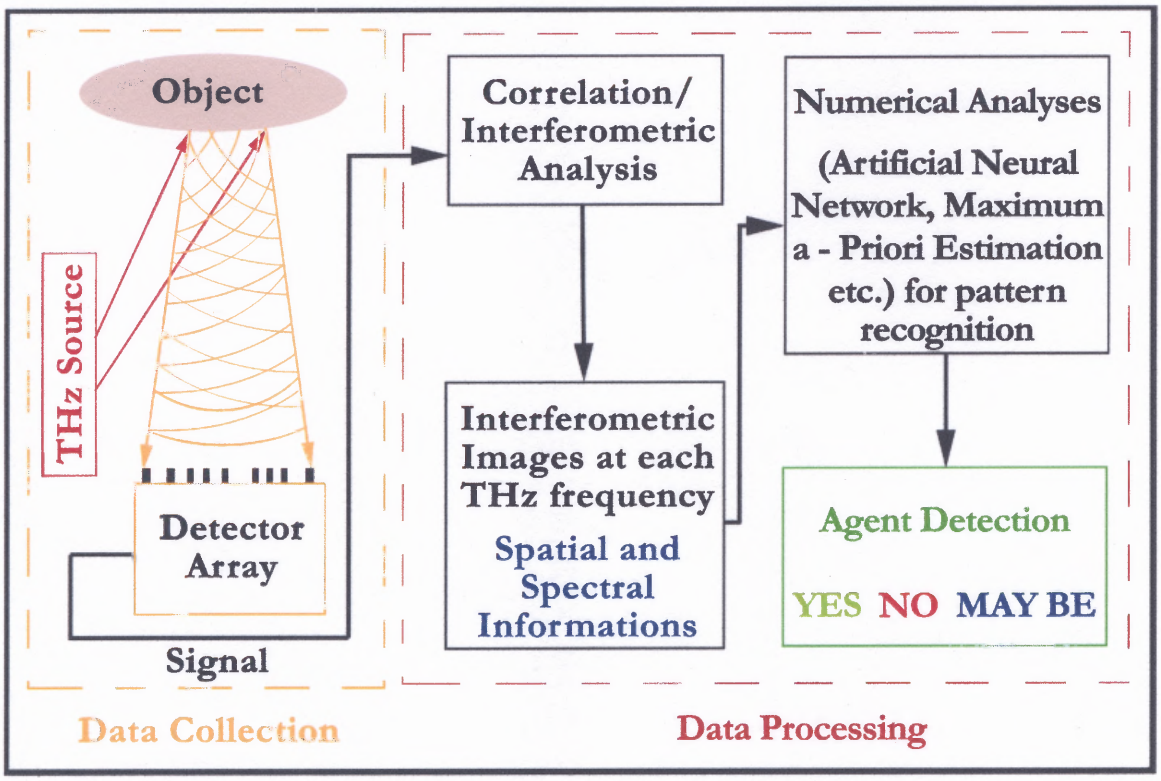

Figure 6.1 Proposed THz imaging system for security screening.

However due to the current limited availability of resources, especially suitable THz sources and detectors, the measure of the performance of the THz imager in its developmental stage cannot be estimated directly. Moreover, demonstrating the value of the technique against more established imaging procedures is difficult. Especially owing to the fact that necessary high power THz sources and sensitive and fast detecting mechanisms required to obtain fast frame rates with high resolution are not readily accessible.

Therefore in addition to the ongoing experimental testing of this THz imaging system[199], extensive simulations yield spatial composite images of agents at different frequencies. These images are simulated based on the spectral data obtained with a THz Time Domain Spectroscopic (THz-TDS) system and different interferometric detector configurations. Apart from performance evaluation, this exercise is also important to estimate the correct range of frequencies of operation to obtain necessary spectral contrast of different agents in an image for positive identification. Additionally, interferometric reconstructed images obtained either from experimental observation or through simulation, cannot be interpreted directly for agent identification. Therefore, artificial neural network (ANN) analysis has been employed as an agent classifier in the subsequent processes of agent identification out of those images.

In this chapter, a compilation of all the above computational techniques to generate simulative interferometric reconstructed images and identify the same using ANN analysis has been discussed in detail. At the same time, some of the preliminary images obtained experimentally using the THz interferometric imager are also shown.

6.2 Background

In the wake of the acute sense of vulnerability to concealed threats, a primary focus of national security is the development of non-obtrusive, yet highly reliable schemes for monitoring and detection of different lethal agents. While several existing security screening technologies such as, X-rays, infrared, ion mobility spectrometry and others have their various advantages and disadvantages, there has been considerable interest in exploring the capabilities of Terahertz screening systems. Its ability to penetrate non-

metallic common materials, such as clothing, plastic, ceramic, wood, and identify hidden objects, such as plastic explosives, chemicals and other materials beneath clothing and in packages [200, 201, 202, 203, 204] presents an opportunity to use THz technology in the areas of security and defense. Moreover, since energies of $\sim 10^{-21}$ J of THz frequencies are equal to discrete molecular vibrational, torsional and librational modes in liquids and solids, there is existence of spectral signatures of various explosives and chemical species in THz range. That increases the potential of specificity to reduce false-alarm rates. At the same time, as the energy levels of THz radiation are very low (1–12 meV), damage to cells or tissue should be limited to generalized thermal effects, that is, strong resonant absorption seems unlikely.

From an imaging standpoint, this wavelength regime is appropriate since the diffraction limited spot size ($1.22\lambda_0$ = 366 μm @ 1 THz) yields a resolution (~70 dots/in) that is comparable to the resolution of a standard modern day computer monitor. Submillimeter-wavelength scale also implies that terahertz signals would pass through tissue with only Mie scattering rather than much stronger Rayleigh scattering (proportional to ν^4) that dominates in the IR and optical region since cell size is much less than the wavelengths of the radiation. All of these reasons implies that, THz imaging technology has all the potential to complement and enhance existing and emerging imaging techniques to increase operational effectiveness in security screening[205, 206, 207].

6.3 Interferometric Spectral Imaging

The interferometric spectral imaging technique is suited for THz security imaging as it requires only a few individual detector elements and can image many sources of THz radiation at once. Therefore, this approach has the potential of developing a cost-effective, fast THz imager. It can also produce images using incoherent as well as coherent sources, and provides spectral information as well as spatial imaging data[208, 209].

The proposed imaging interferometer consists of an array of individual detectors arranged non-periodically. As the wavefront of reflected (or transmitted) THz radiation encounters the array, each pair of detectors measures one spatial Fourier component of the incoming THz radiation as determined by the separation of the detector pair, otherwise known as a baseline. Each spatial Fourier component is represented by a point in the Fourier transform plane called the *u-v* plane. In other words, signals at two or more points in space (that is the detector aperture plane) are brought together with the proper delay and correlated both in phase and in quadrature to produce cosine and sine components (points in the Fourier transform u-v plane) of the brightness distribution. In order to determine a spatial Fourier component and hence the direction of the incoming THz wavefront, the phase delay in the arrival of the wavefront between a pair of detectors must be measured. The relative angle between the direction to the source and the baseline (an imaginary line connecting the two detectors) defines the geometric delay τ_g in arrival of the wavefront between the two detectors. All the directions that form a cone around the baseline have the same phase delay

$$\tau_g = \frac{b\sin(\alpha)}{c} \tag{6.1}$$

where b is the length of the baseline, c is the speed of light, and α is the relative angle. In order to determine the correct source direction, additional measurements with other orientations of the baseline must be carried out[210].

In the proposed THz imager, the THz radiation incident onto the interferometric detector array corresponds to either the reflection or transmission spectrum of the objects being irradiated. Given N detectors, there are N(N-1)/2 possible pairs of baseline combinations.

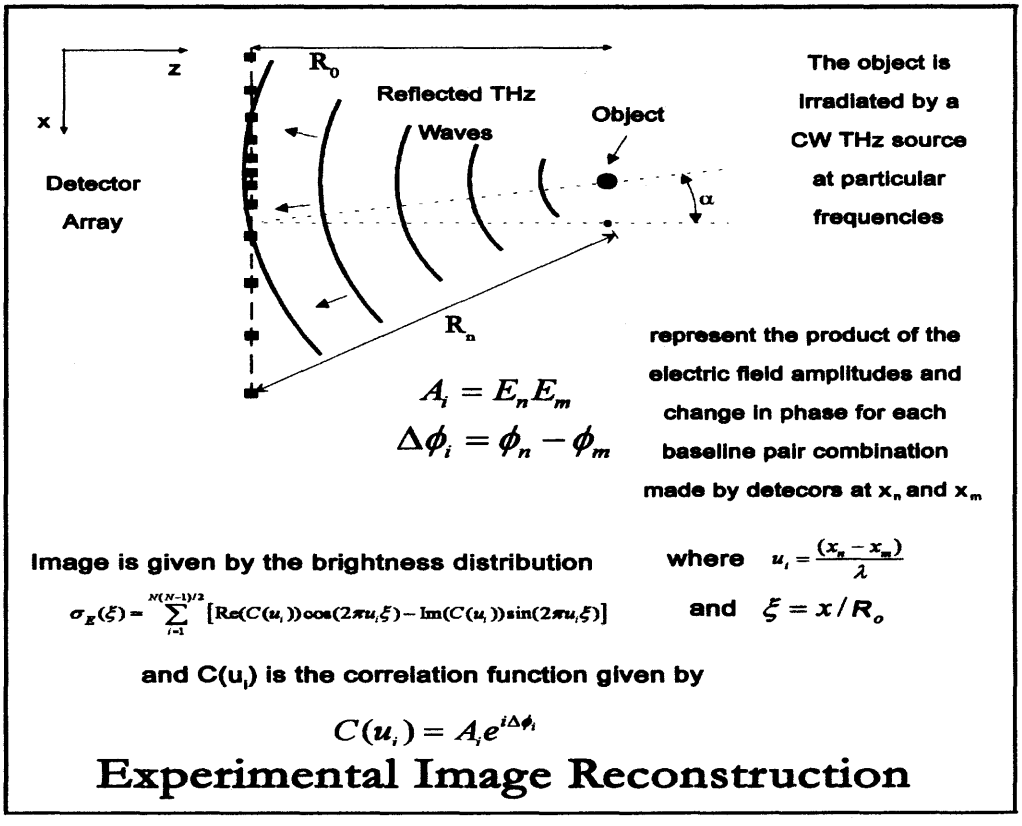

Figure 6.2 Flowchart showing experimental scheme for terahertz interferometric image reconstruction.

Figure 6.2 illustrates experimental interferometric image reconstruction with a linear set of detectors for a linear image in reflection mode. It explains the calculation of THz brightness distribution through measurement of THz electric field amplitudes and

phases at each detector element. In order to obtain an interferometric image of an object by an N element detector array, amplitudes and phases of THz field at the point of each detector are necessary. The generated image is represented by the brightness distribution function

$$\sigma_E(\xi) = \sum_{i=1}^{N(N-1)/2} \left[\mathrm{Re}\left(C(u_i)\right)\cos\left(2\pi u_i \xi\right) - \mathrm{Im}\left(C(u_i)\right)\sin\left(2\pi u_i \xi\right) \right] \tag{6.2}$$

For detector positions x_m and x_n, $u_i = (x_n - x_m)/\lambda$ and $C(u_i) = A_i e^{i\Delta\phi_i}$ is the electric field correlation function. $A_i = E_m E_n$ and $\Delta\phi_i = \phi_m - \phi_n$ represent the product of electric field amplitudes and change in phase for each baseline pair combination, respectively[211].

Unlike the astronomical applications where the interferometric imaging array is typically operated in the far field (that is, planar wavefront), for the present imaging applications, the object to be imaged is in the near-field (that is, the spherical wavefront) region of the imaging array. Consequently, the far-field image reconstruction must be modified to account for the wavefront curvature in the near-field. The near-field correction is calculated conceptually by repositioning the detectors from a linear arrangement to a spherical arrangement that matches the curvature of the incoming wavefront.

Apart from the spatial information of different sources, the reflected wavefront also carries the characteristic spectral signature of the sources present. Therefore, by combining two or more images of the same set of objects made at two or more different THz frequencies, composite interferometric spectral images are obtained through which

discrimination or classification of lethal agents, even hidden behind barriers, can be achieved using appropriate numerical techniques.

To obtain the measure of the performance of the proposed THz imager, initially a point source of THz radiation for a particular detector configuration is imaged. This essentially provides the point spread function or the impulse response function of the particular detector array.

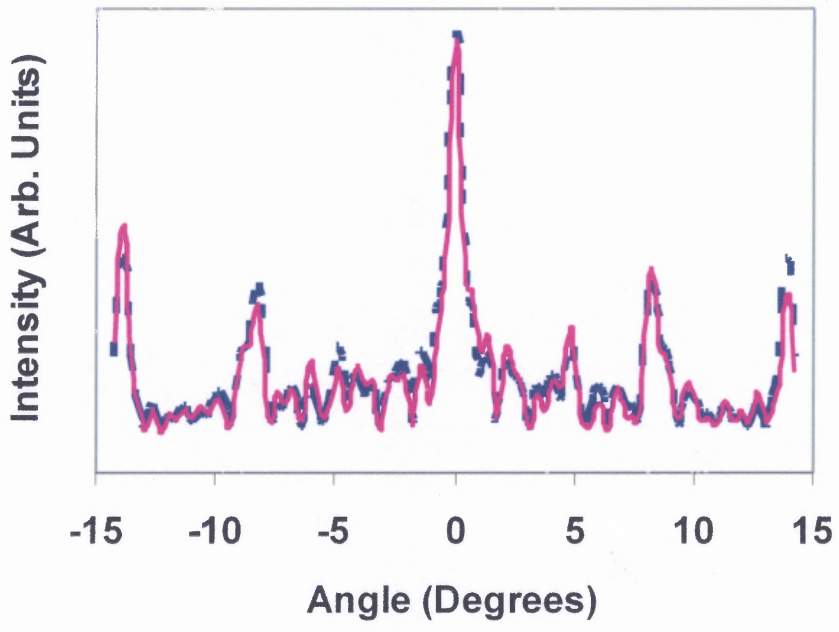

Figure 6.3 Comparison of a reconstructed line image (solid line) with near-field correction and theoretically predicted point image (dashed).

Figure 6.3 shows the comparison between the reconstructed line THz images of a point THz source with near-field correction with theoretical predictions of a point source image. The interferometric array in this case was of 8 detectors at a distance of 40.9 cm from the source. Subsequently, a piece of 3 cm wide rough metal object is imaged using the same detector configuration, but at a distance of ~1 m. The object surface is kept rough which provides uncorrelated reflections of electric field from the object.

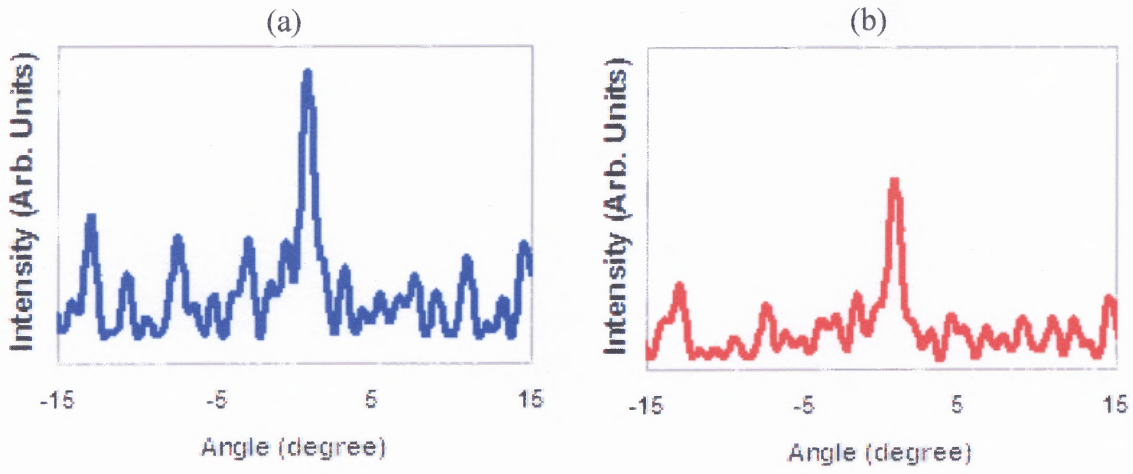

Figure 6.4 Linear interferometric images of a metal object obtained with reflected THz radiation, where (a) shows the image of the metal object (with no barrier) and (b) the image of the same object hidden behind a book bag.

Figure 6.4 (a) shows a linear interferometric image of the metal object without any barrier and Figure 6.4 (b) represents the image of the same with a barrier of book bag, respectively. Behind the bag, object is still detected at the correct position. The book bag used in the experiment is ~ 2 mm thick and is non-transparent for visible light. In all of these experiments, only one THz detector was used, which was mounted on an X-Y computer controlled stage. The movement of this stage allows the change in the position of the THz detector and obtains oscillations of THz field at several points. Subsequent extractions of the THz amplitude and phase at those points from the obtained data provides the electric field correlation function for each pair of detector positions resulting in the image reconstruction using the interferometric imaging method. Due to this shortage of THz detectors, computational technique is vital to design optimum interferometric detector configuration for optimum image quality.

6.4 Interferometric Image Simulations

For the interferometric image simulation, the starting point is a bitmap image of the object under study. The image is then appropriately converted to multiple images at different THz frequencies, containing the spectral characteristics of different compounds present, based on their individual THz reflection spectra. After the Fourier transform of these raw images, they are multiplied by the corresponding Fourier transform of the mask at those frequencies. These masks are the impulse response or point spread function for the imaging system. They are dependent on the specific detector configuration, and the distance between the object and detector plane. In other words, these functions are a measure of the energy spread of a central THz source. An inverse Fourier transform is applied to these products. The results are simulated reconstructed interferometric images of the object under study at those particular THz frequencies.

In the present study, a problem "Metal-RDX" is considered. This is a set of images of 1 pixel by 500 pixel size as produced by the interferometric image simulation. It corresponds to an object consisting of a 2.5 cm square of gold mirror and a 2.5 cm square of Composite C-4 explosive (91% RDX or cyclotrimethylenetrinitramine + 9% plasticizer) placed 5 cm apart at a distance of 1 meter from the detector array. The detector array is linear and consists of 10 detectors. The probing frequencies are 0.7 THz and 0.9 THz, which together produce a contrast of roughly 8% for Composite C-4 in its reflection spectrum as measured with the THz Time Domain experimental set-up[212]. Earlier reports also cite similar spectral signatures of this substance at two different THz frequencies[213, 214]. Figure 6.5 shows the flowchart of the simulative interferometric reconstructed THz images.

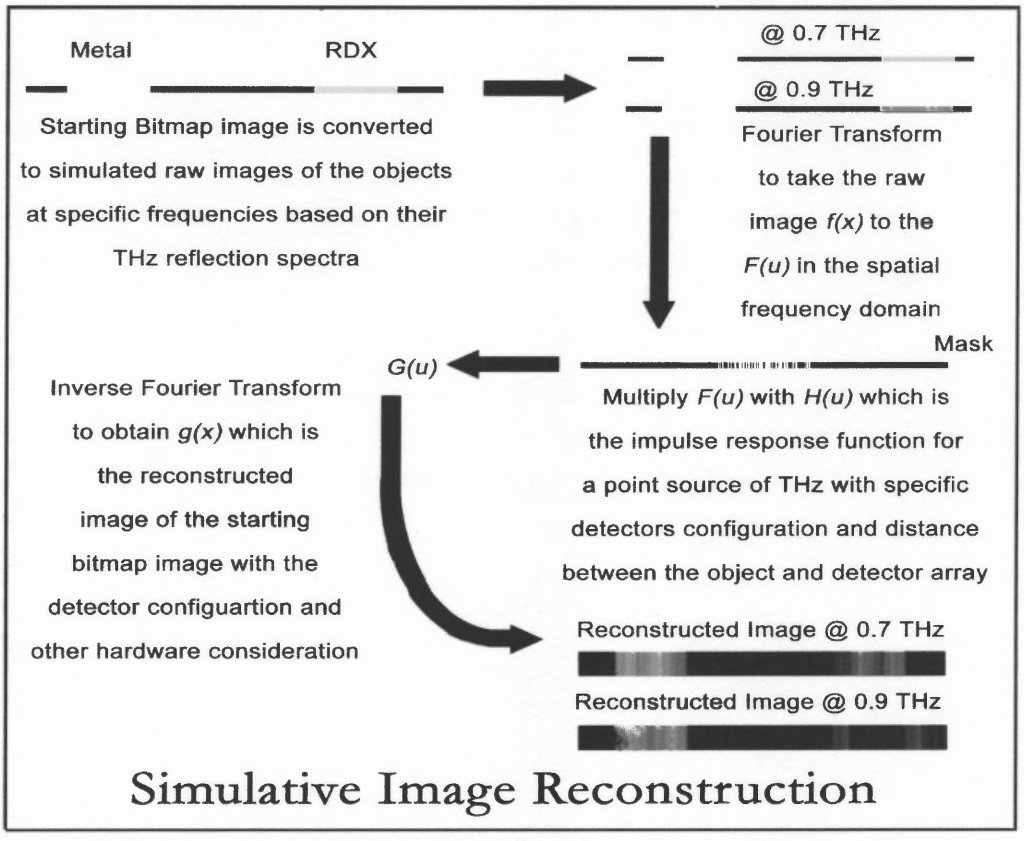

Figure 6.5 Flowchart showing simulation schemes for terahertz interferometric image reconstruction.

Figure 6.6 shows the reconstructed images of the Metal-RDX object obtained through simulative image reconstruction.

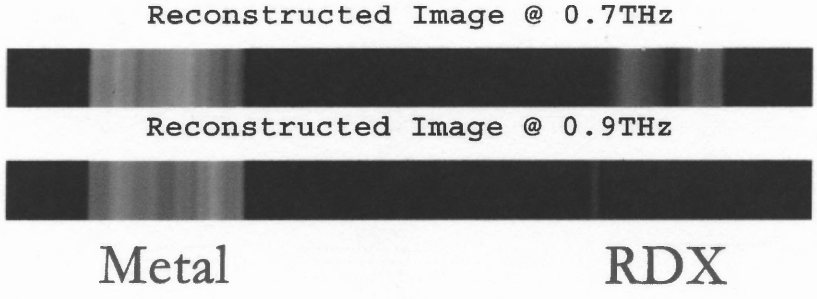

Figure 6.6 The reconstructed images in the Metal-RDX problem at two frequencies of interest as obtained from the simulation.

One may readily see the spectral contrast of the agent Composition C-4 explosive at two THz frequencies as opposed to metal which has flat spectral response in THz range. In this study, the main objective is to establish a working model for a successful spectral classification of different agents using these simulated interferometric images. Therefore linear images are sufficient as they contain all the spectroscopic information of various agents for the spectral classification purpose. However, linear images can only specify the relative positions of the agents present, but cannot describe the geometrical shapes of the same.

6.5 Image Analysis Using Artificial Neural Network Analysis

Interferometric reconstructed images obtained either from experimental observation or through simulation, cannot be interpreted directly for agent identification. These images contain fringe pattern, which is characteristic artifact of the interferometric image formation, as well as additional effects due to noise, signal fluctuation and other variables. These problems make extraction of spatial and spectral information on potential hidden agents present in the images very difficult with traditional numerical approaches. Therefore, towards the realization of an efficient and accurate classification and positive identification scheme for lethal and non-lethal agents in an image, Artificial Neural Network (ANN) analysis is employed.

Inspired by biological nervous systems, ANN is essentially an evolved structure of mathematical functions that can perform a particular task of considerable complexity through supervised learning[215]. This kind of computing architecture is especially suitable for solving problems of classification, pattern recognition and identification. A network is

typically trained (that is, calibrated) based on a comparison of its actual output and the desired target. Internal weighting values are adjusted until the network output matches the target description to within a minimal (acceptable) error. During training, the network produces an output to each input whereby correct outputs are reinforcing while incorrect ones cause internal adjustments in the structure of the network[216].

The ANN is extensively used in various industrial, business and scientific applications[217]. An early application of neural networks outside the financial industry was in the area of security screening in 1989[218]. The attributes that make ANN a very suitable tool for agent identification, in contrast to the traditional statistical technique[219] or discriminant analyses[220], are its ability to adapt to the effects of multiple variability by processing sufficiently large datasets to optimize an error criterion, and faster performance owing to its tremendous number of interconnects and simple processors[221]. There are various types of ANN architectures frequently used in the application of image processing and pattern recognition[222]. In our present study, the following methods are adopted, which are Multilayer Perceptron (MLP) model and the Kohonen Self-Organizing Maps (KSOM). The interferometric image simulation and KSOM model are done using the MATLAB® [223]. The MLP model is done using the NeuroSolutions for MATLAB® software package from NeuroDimension, Inc[224].

6.5.1 Application of Multilayer Perceptron Model

The MLP model is the most widely used class of ANN, especially for classifications. The MLP can "learn" how to interpret large sets of input data relatively fast, though MLPs do require considerable training to be effective[208]. The MLP consists of input, hidden and

output layers. The computation at the k^{th} node in a MLP considers a weighted sum (activation value net_k) of inputs (vector I_j). The output, o_k, of the node is computed by:

$$o_k = \tanh(net_k) = \tanh(\sum_{j=1}^{j} w_{kj} I_j) \tag{6.3}$$

where w_{kj} represent a set of weights that are optimized during the training process. Figure 6.7 represents a schematic of the basic structure for a MLP model. The threshold function can be varied, though *tanh* is common and effective.

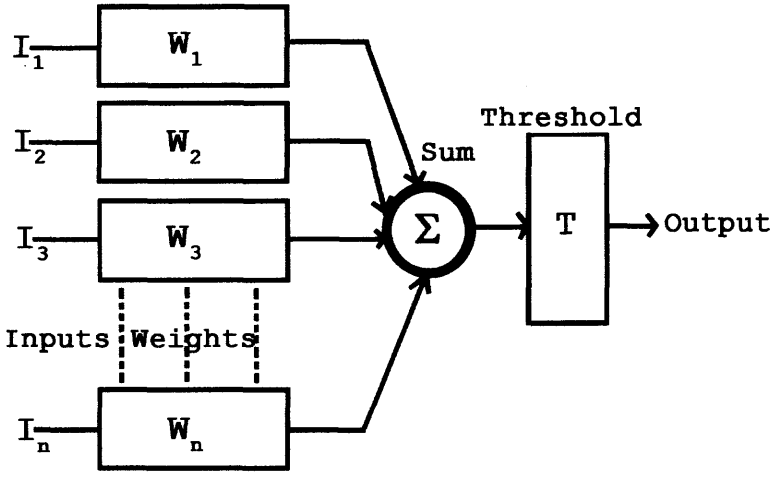

Figure 6.7 Schematic representation of Multilayer Perceptron Model.

The reconstructed images corresponding to the object Metal-RDX are first processed to prepare the training dataset for the MLP model used in the present study. For the purpose of generating the dataset to train the MLP, the simulation produces separate images in the following manner:

- Only a single metal square or a single RDX square is imaged at a time, keeping the size, distance, detector configuration and other factors constant.

- To achieve superior randomization in the training set, which essentially returns better performance of a trained ANN, the spatial position of the object is changed. In other words, the square of metal or the square of RDX is placed at different spatial locations in the image.

- These images are then scanned with a template of 1 pixel by 5 pixel rectangular template. Thus they are converted to input matrices where each row is assigned with a desired output of 0, 1 or 2 depending on whether the template finds background, metal or RDX during its scanning of a given row. Compared to a pixel-by-pixel approach, this method of scanning reduces the data preprocessing time considerably.

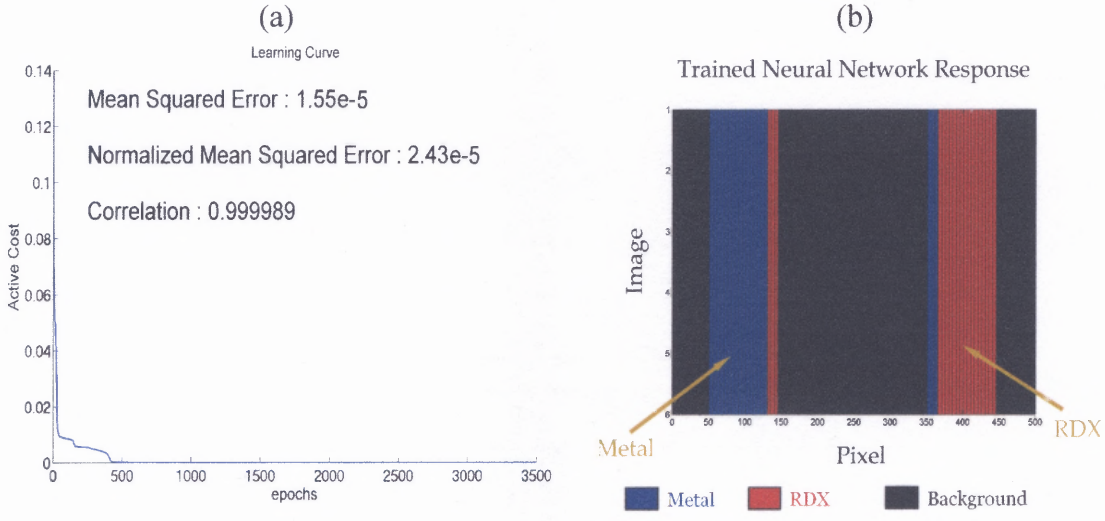

Figure 6.8 (a) The learning curve obtained during the training of the MLP structure used in the Metal-RDX problem with 2 hidden layers and 3500 epochs; (b) The response of the trained MLP network to the unknown input in the Metal-RDX problem.

Successful training of the MLP network consisting of 2 hidden layers required less than 5000 epochs (or iterations) as illustrated by the Learning Curve of the MLP in Figure 5 (a). During this training session, the input was the set of simulated images with one agent placed on bare background at a time as described above. In the present case, with 2 hidden layers it is found that the active cost of the MLP stabilizes quickly within or less than 1000 epochs, indicating better performance. The mean square error (that is, the square of the difference between the calculated and desired output) is found to be

appreciably low at 1.55E-5 with a very high correlation value, approaching 1, as shown in the learning curve in Figure 5. This suggests a successful execution of the MLP structure in recognizing the spectral signatures of the metal and RDX. The trained MLP is then tested using another set of simulated images of individual agents on the background.

Once successfully trained and tested, the MLP network is then employed to an unknown input, that is, a set of composite images of the Metal-RDX as shown in Figure 6.6. The response is found to be quite satisfactory as shown in Figure 5 (b). The MLP network could recognize metal and RDX in their respective original positions. However in some of the pixel positions in between the metal and RDX squares, some ambiguities are found. This is due to the so called boundary effect where the reconstructed images themselves bear the edge effect due to the Fourier transform and subsequent finite sampling of the image space in generation of the mask. This is a fundamental problem of digital image processing[225]. When the sampling function chooses a pixel near the edge or boundary of an image, then some of the weight of the function also operates upon "invalid pixels" beyond the boundary of the real image. As a result, the intensity values which directly correspond to the spectral characteristics of the agents under concern get distorted, and therefore, the MLP cannot classify or discriminate these pixel positions accurately.

6.5.2 Application of Kohonen Self Organizing Maps

Kohonen Self Organizing Maps are two-layer (input and output) neural networks[226, 227]. The output is typically a two-dimensional arrangement of nodes, often forming square or hexagonal maps. The number of input nodes is, in the present case, equal to the number

of frequencies at which the measurements are made (0.7 THz and 0.9 THz, in the present study). Input patterns presented to the network for processing are vectors with two elements; these elements are image intensities corresponding to the same pixel at the two distinct frequencies. The number of input patterns presented to the network is the number of pixels in the images. No training is required in this method.

The input layer is linked to the output map through weighted connections. The weights are initially randomized, with a random mapping from input patterns to output nodes. Weights are adapted iteratively in a way that maps input patterns with a small Euclidean distance to the same or neighboring nodes. Thus, measurements corresponding to the same object are mapped to a cluster in the output space. Measurements corresponding to different objects with distinct spectral signatures will typically produce large distance and will be assigned to different clusters. The goal is to generate spatially separated clusters at the output corresponding to the distinct categories of data. The number of iterations necessary for the process to converge depends on the number of input patterns and output nodes. Convergence is here defined as the state during which the map does not change significantly between consecutive iterations.

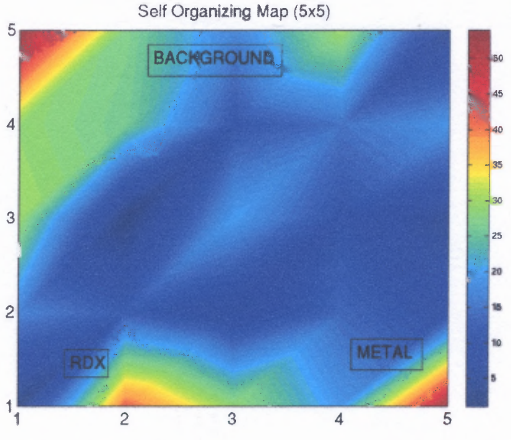

Figure 6.9 The response of the KSOM to the Metal-RDX problem.

In this work a square output map with 25 nodes was considered; the network was presented with 500, two-element input patterns. The 5x5 output map shown in Figure 6.9 demonstrates that the KSOM successfully separates the three classes that are present in the data (metal, RDX, and background) into three distinct clusters; metal is mostly mapped to neighboring nodes (5,1) and (5,2), RDX is mapped to neighboring nodes (2,1), (3,1), and (2,2), and background is mapped to a large cluster of nodes with a peak at the upper left corner (1,5) of the map (a pair (x,y) denotes a KSOM node at coordinates x and y, where x and y are integers with values between 1 and 5). The intensity value at each node represents the number of elements mapped there. Higher intensity is observed in the background cluster, because the number of background pixels exceeds the numbers of metal and RDX pixels within the original interferometric image.

6.6 Further Issues with Image Analysis

The fundamental approach of agent classification using ANN in THz interferometric spectral imaging as described in the above sections becomes complicated when practical issues such as the presence of barriers, nearby boundaries of different agents, comparable spectral signatures for different agent classes and other factors come into play. In this study, the impact of barriers is discussed.

In most real cases, the effects of a barrier are primarily manifested in terms of reduced signal to noise. These effects essentially lower the specificity in the classification process. A possible solution is the removal of the spectral pattern of the barrier material from the composite signature of the agent behind the barrier. It should be noted that, common barriers such as cotton, wool, leather etc. have either flat or monotonically

increasing or decreasing spectral properties in the THz range. Thus it is nominally possible to "see through" the barriers and identify the agent, provided the reduction in signal to noise is not significant.

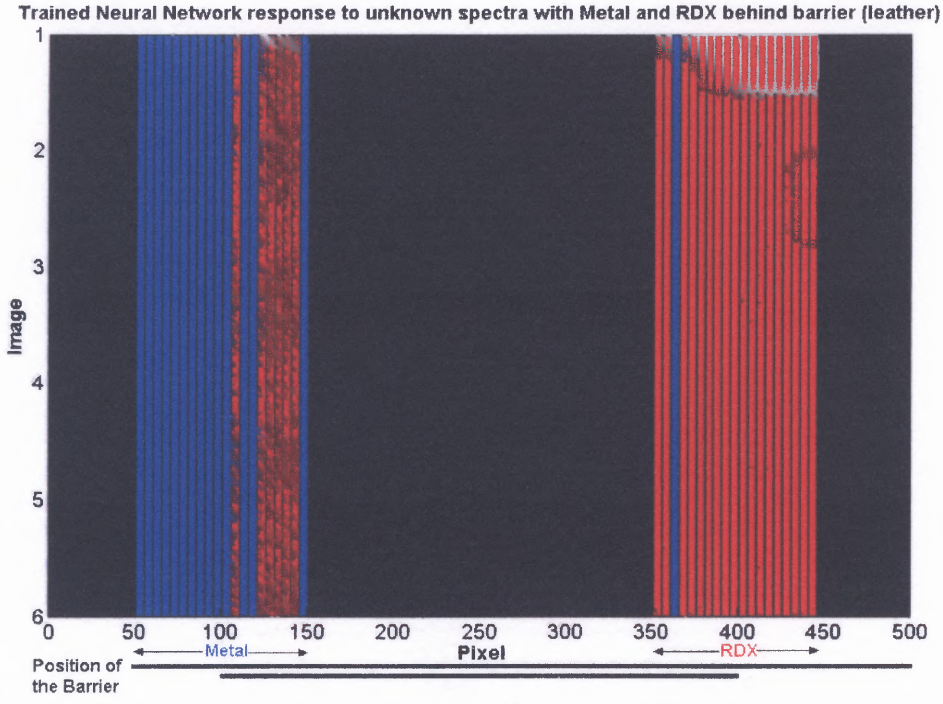

Figure 6.10 The response of a trained MLP network to the unknown input in the Metal-RDX problem behind leather barrier. The position of the multilayer barrier is shown at the bottom of the figure with black solid lines.

As shown in Figure 6.10, the Metal-RDX object was placed behind two layers of leather in the simulation. The normalized reflectance of leather are 0.34 and 0.46 at 0.7 THz and 0.9 THz respectively[228] and therefore the reduction in signal to noise due to the presence of 2 layers of leather is found to be more at 0.9 THz. The MLP network could still effectively classify the two agents and background behind the barrier. For the training of the MLP used in this case, it was found that, its performance is improved when different combinations of barrier materials such as, wool, cotton and leather were used in different spatial positions in the training dataset. One other important

consideration was the fact that both the training and testing set of images have to contain some bare background. In other words, the MLP network has to "see" a portion of the background without any barrier during the training. In this case, we also observe that the effect of boundaries or the edge effect as discussed in Section 6.5.1 is enhanced due to the presence of additional boundaries of the barrier.

6.7 Recent Experimental Results

Only very recently, the THz Spectroscopy and Imaging group at NJIT is able to obtain two-dimensional THz interferometric images for the very first time.

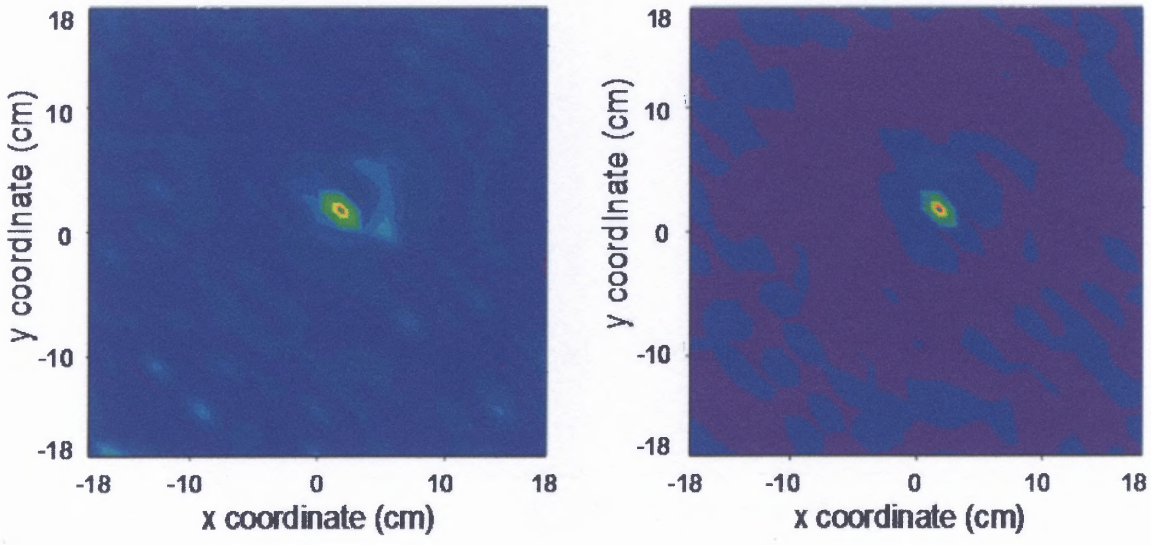

Figure 6.11 Two-dimensional interferometric images of point source obtained with a spiral array of 64 detectors, where (a) shows the image of the point source (with no barrier) and (b) the image of the same hidden behind a book bag.

As shown in Figure 6.11, two-dimensional interferometric images of point source are obtained with a spiral array of 64 detectors, where Figure 6.11 (a) shows the image of the point source (with no barrier) and Figure 6.11 (b) shows the image of the same hidden behind a book bag.

6.8 Conclusions

In this study, a design of a stand-off imaging system in the Terahertz (THz) range is conceived using an interferometric detector array to detect concealed lethal agents. The composite images of simulated objects under THz illumination are analyzed using artificial neural networks to make positive identification of the lethal agent based on their spectral characteristics. It has been shown that a THz imager which allows sufficient signal to noise ratio could be used to image concealed threats. The ongoing research is directed at eliminating the disadvantage of linear imaging in the current experimental set-up which does not allow the reconstruction of the geometrical shape of the target but only its position. Therefore the aim is to produce stand-off two dimensional images of extended objects, especially behind barriers at a faster capturing rate experimentally. Additionally, another direction of improvement is to incorporate the statistical nature of noise and the effect of barriers in the image analysis and subsequent agent classification.

CHAPTER 7

CONCLUSIONS AND FUTURE OUTLOOK

From its inception in 1980s, THz sciences and technology has come a long way. Both THz spectroscopy and THz imaging techniques have evolved into versatile tools for the fundamental study of materials and for the realization of myriad of applications from bio-medical imaging and security imaging to environmental sensing to quality assessment. Yet, in true sense, THz technology is just beginning to come of age. This rapidly improving and changing area is thus poised for great advances as new sources and detectors are developed and new applications are found. Therefore in this dynamic field, as researchers are finding new answers every day, more questions are springing up as well.

As discussed in the beginning of this dissertation, THz radiation propagation, THz device description and different detection architectures are some of the most overlooked areas of THz research. Therefore this dissertation work has made an attempt to answer some of the lingering questions, especially pertaining to the roles of THz scattering, guided THz propagation, THz frequency filtering and presence of barriers on the device performance of an interferometric THz imager. Through experimental studies and analytical results using various modeling and simulations, this work has extended the present understanding of interaction of THz radiation with materials and structures. The work also has demonstrated the effectiveness of an interferometric THz imager under development.

In this concluding chapter, a summary is provided below of some the central questions asked and the answers found in all of the previous chapters of the dissertation.

- In Chapter 3, the question posed was whether any spectroscopic identification of an unknown granular solid in a concealed manner can be made based on the frequency trend of its THz extinction spectra. To answer the same, experimentally obtained (using THz Time Domain Spectroscopy) extinction spectra of granular salt, sugar, flour, chalk and Ammonium Nitrate of different grain sizes between 0.2 to 1.2 THz have been analyzed using Mie scattering theory. It has been shown that the obtained extinction for these non-absorbing materials in the frequency range of study essentially consist of scattering losses and the intrinsic material absorption and scattering losses are separated from the total extinction. Finally, it was found that as the frequency dependence of the extinction of a solid is a function of both its material property, as well as its grain size, an unique identification of an unknown granular solid in a concealed manner cannot be made.

- In Chapter 4, a more general question was asked that whether hollow core cylindrical waveguide structures can be used to guide THz pulse without appreciable loss and dispersion. To answer the same, the experimental study characterized a guided TE_{01} mode which was launched into a straight Cu cladded hollow core waveguide, in terms of signal attenuation and dispersion. However, it was found that the estimation of both the attenuation and dispersion of the waveguide structure is limited by the approximation of n and k values of the metal coating. Therefore for a more direct answer, reliable experimental measurements of n and k are required in THz region. Additionally, the effect of water vapor absorption to the estimation of the attenuation can be minimized by purging of the experimental set-up. For a more practical approach, the scope of the present study is also to be broadened to include the characterization of hollow core waveguides with different bore sizes, different coating materials, outer layers and bent structures with different radii of curvatures.

- Chapter 5 posed a question which sprang from a recent series of activities in terms of THz frequency management through the use of quasi-optic structures. Design of a wavelength-scalable, band reject THz frequency filter using multilayer structure in reflection mode has been proposed. A physical model based on Impedance Matching approach which takes into account of the Fabry-Perot effect was made. Different parametric simulations demonstrated that the experimentally characterized samples of Ferrous Boride as individual layers, shows poor performance in frequency filtering. While the metal grid filters show good performance of frequency filtering but only with a very narrow band (that is, around the resonance frequencies of the grid structures). Further simulative examples suggested that to design a multilayer structure to obtain a featureless, broadband frequency rejection in reflection over a certain frequency range, a

large of number layers with variation in both refractive indices and attenuation coefficients are to be used.

- In Chapter 6 with a design of a stand-off imaging system in the THz range using an interferometric detector array to detect concealed lethal agents, an answer has been made to the ongoing quest of developing a working imaging system in security screening application. However, in this chapter, a number of questions have also emerged in terms of the performance measure of such an imaging system. Through interferometric image simulation, composite images of objects under THz illumination are analyzed using artificial neural networks to make positive identification of the lethal agent based on their spectral characteristics. It has been shown that a THz imager which allows sufficient signal to noise ratio could be used to image concealed threats. As the aim is to produce stand-off two dimensional images of extended objects, especially behind barriers, at a fast capturing rate, there are many future challenges that are need to be addressed. The ongoing experimental research is directed at eliminating the disadvantage of linear imaging in the current set-up which does not allow the reconstruction of the geometrical shape of the target but only its position. From analytical point of view, further improvement is to incorporate the statistical nature of noise and the effect of barriers in the image analysis and subsequent agent classification.

It would not be an understatement to mark the past decade in the development of the THz science as the "era of origination" as various THz sources and detectors are invented, as described in Chapter 2. However, as new THz applications are now rapidly coming up, the bracket of different THz sources and detectors are needed to be extended further. Therefore, a great part of research efforts continue to produce more powerful, intense continuous and broadband THz sources and sensitive and fast THz detectors.

Apart from this continuing core initiative in terms of developing new THz sources/detectors, different commercial THz-TDS systems are currently being developed. Therefore, it can be expected that the availability of such systems (which can be operated by any generally informed researcher) will promote a variety of investigations in different fields of physical, chemical and biological research. Moreover, two distinct areas, that is, THz spectroscopic evaluation of materials and THz spectral imaging will be pursued further in different disciplines of science. With the conjunction of these two techniques,

various industrial applications are conceivable, where spectral and spatial information of concealed objects in THz range opens up new horizons.

Finally in this concluding section, with particular reference to this present dissertation, some open questions are posed below. The aim is to incite future researchers to continue the present quest further in understanding the propagation and detection of THz radiation in the application of THz spectroscopy and imaging.

- How can one incorporate the effect of multiple scattering in explaining the THz interaction with granular solid? Will that resolve the ambiguities in THz extinction spectra of various solids?

- What is the origin of negative THz dispersion in metal cladded hollow core waveguides? Can this be applied to fabricate dispersion compensating structures in THz range by tailoring the material properties of the cladding layer?

- Is it possible to conceive a multilayer THz filtering structure with metamaterials as individual layers and then what would be the physical dimensions and properties of such layers? How convenient would it be from fabrication point of view?

- In what ways will the coherent/incoherent nature of THz radiation affect the THz image quality? How one can simulate such parameters, especially in an interferometric detection set-up?

- Is it possible to come up with a definite threshold (in terms of the power of THz source, sensitivity of the detectors, presence of different barriers, and interspatial distances of different agents in the object field) of detectibility of a THz imager?

REFERENCES

1. D. H. Auston, "Picosecond optoelectronic switching and gating in silicon," *Appl. Phys. Lett.*, **26**, 101 (1975).

2. C. H. Lee, "Picosecond optoelectronic switching in GaAs," *Appl. Phys. Lett.*, **30**, 84 (1977).

3. D. H. Auston, K. P. Cheung, J. A. Valdmanis & D. A. Kleinman, "Cherenkov radiation from femtosecond optical pulses in electro-optic media," *Phys. Rev. Lett.*, **53**, 1555 (1984).

4. K. P. Cheung and D. H. Auston, "A novel technique for measurement of far-infrared absorption and dispersion," *Infrared Phys.*, **26**, 23 (1986).

5. P. R. Smith, D. H. Auston, and M. C. Nuss, "Subpicosecond photoconducting dipole antennas," *IEEE J. Quantum Electron.*, **24**, 255 (1988).

6. C. Fattinger and D. Grischkowsky, "Terahertz beams," *Appl. Phys. Lett.*, **54**, 490 (1989).

7. D. Grischkowsky, S. Keiding, M. van Exter, & C. Fattinger, "Far-infrared time domain spectroscopy with terahertz beams of dielectrics and semiconductors," *J. Opt. Soc. Am. B,* 7, 2006 (1990).

8. J. E. Pedersen and S. R. Keiding, "THz Time-Domain Spectroscopy of Nonpolar Liquids," *IEEE J. Quantum Electron.*, **28**, 2518 (1992).

9. D. M. Mittleman, R. H. Jacobsen, R. Neelamani, R. G. Baraniuk and M. C. Nuss, "Gas sensing using terahertz time-domain spectroscopy," *Appl. Phys. B.*, **67**, 379 (1998).

10. T. Aoki, M. W. Takeda, J. W. Haus, Z. Yuan, M. Tani, K. Sakai, N. Kawai and K. Inoue, "Terahertz time-domain study of a pseudo-simple-cubic photonic lattice," *Phys. Rev. B*, **64**, 045106 (2001).

11. B. B. Hu and M. C. Nuss, "Imaging with terahertz waves," *Opt. Lett.,* **20**, 1716 (1995).

12. D. M. Mittleman, R. H. Jacobson, and M. C. Nuss, "T-ray imaging," *IEEE J. Sel. Topics Quantum Electron.*, **2**, 679 (1996).

13. P. Y. Han, M. Tani, M. Usami, S. Kono, R. Kersting and X. C. Zhang, "A direct comparison between terahertz time-domain spectroscopy and far-infrared Fourier transform spectroscopy," *J. Appl. Phys.*, **89**, 2357 (2001).

14. M. C. Beard, G. M. Turner and C. A. Schmuttenmaer, "Terahertz Spectroscopy," *J. Phys. Chem. B*, **106**, 7146 (2002).

15. T. Globus, D. Woolard, M. Bykhovskaia, B. Gelmont, L. Werbos, and A. Samuels, "THz-frequency spectroscopic sensing of DNA and related biological materials," *Int. J. High Speed Electron. Syst.*, **13**, 903 (2003).

16. P. F. Taday, "Applications of terahertz spectroscopy to pharmaceutical sciences," *Phil. Trans. R. Soc. Lond. A*, **362**, 351 (2004).

17. Y. Chen, H. Liu, Y. Deng, D. Schauki, M. J. Fitch, R. Osiander, C. Dodson, J. B. Spicer, M. Shur, X.C. Zhang, "THz spectroscopic investigation of 2,4-dinitrotoluene," *Chem. Phys. Lett.*, **400**, 357 (2004).

18. P. H. Siegel, "Terahertz Technology," *IEEE Trans. Micro. Th. and Tech.*, **50**, 910 (2002).

19. A. G. Davies, E. H. Linfield and M. B. Johnston, "The development of terahertz sources and their applications," *Phys. Med. Biol.*, **47**, 3679 (2002).

20. B. Ferguson and X. C. Zhang, "Materials for terahertz science and technology," *Nature Materials,* **1**, 26 (2002).

21. D. Dragoman and M. Dragoman, "Terahertz Fields and Applications," *Prog. Quantum. Elect.*, **28**, 1 (2004).

22. D. L. Woolard, E. R. Brown, M. Pepper & M. Kemp, "Terahertz Frequency Sensing and Imaging: A Time of Reckoning Future Applications?", in *Proc. IEEE*, **93**, (2005).

23. G. Gruner, (ed.) Millimeter and Submillimeter Wave Spectroscopy of Solids (Springer, Berlin, 1998).

24. D. M. Mittleman, (ed.) *Sensing with Terahertz Radiation* (Springer, Berlin, 2003).

25. D. Draogoman and M. Dragoman, *Optical Characterization of Solids* (Springer, Berlin, 2002).

26. K. Sakai, (ed.) *Terahertz Optoelectronics* (Springer, Berlin, 2005).

27. E. Budiarto, N. W. Pu, S. Jeong, and J. Bokor, "Near-field propagation of terahertz pulses from a large-aperture antenna," *Opt. Lett.*, **23**, 213 (1998).

28. P. U. Jepsen and S. R. Keiding, "Radiation patterns from lens-coupled terahertz antenna," *Opt. Lett.*, **20**, 807 (1995).

29. O. Mitrofanov, M. Lee, J. W. P. Hsu, L. N. Pfeiffer, K. W. West, J. D. Wynn, and J. F. Federici, "Terahertz pulse propagation through small apertures," *Appl. Phys. Lett.*, **79**, 907 (2001).

30. J. F. Federici, D. Gary, B. Schulkin, F. Huang, H. Altan, R. B. Barat and D. Zimdars, "Terahertz imaging using an interferometric array," *Appl. Phys. Lett.*, **83,** 2477 (2003).

31. Terahertz Systems: Research Application Development Systems from Advanced Photonics, Inc. Retrieved February 17, 2006 from the World Wide Web: http://www.advancedphotonix.com/ap_products/terahertz_research.asp

32. D. L. Woolard, W. R. Loerop and M. S. Shur, (eds.) Terahertz Sensing Technology, Volume 1: Electronic Devices and Advanced Systems Technology (World Scientific, New Jersey, 2003).

33. J. M. Chamberlain, "Where optics meets electronics: recent progress in decreasing the terahertz gap," *Phil. Trans. R. Soc. Lond. A*, **362**, 199 (2004).

34. P. D. Coleman, "Reminiscences on selected millennium highlights in the quest for tunable terahertz-submillimeter wave oscillators," *IEEE J. Sel. Top. Quantum Electron.*, **6**, 1000 (2000).

35. J. F. Federici, O. Mitrofanov, M. Lee, J. W. P. Hsu, I. Brener, R. Harel, J. D. Wynn, L. N. Pfeiffer and K. W. West, "Terahertz near-field imaging," *Phys. Med. Biol,* **47,** 3727 (2002).

36. S. Matsuura , M. Tani , H. Abe , K. Sakai , H. Ozeki and S. Saito, "High-Resolution Terahertz Spectroscopy by a Compact Radiation Source Based on Photomixing with Diode Lasers in a Photoconductive Antenna," *J. Mol. Spectrosc.*, **187**, 97 (1998).

37. M. K. Choi, A. Bettermann and D. W. van der Weide, "Potential for detection of explosive and biological hazards with electronic terahertz systems," *Phil. Trans. R. Soc. Lond. A*, **362**, 337 (2004).

38. D. van der Weide, "Delta-doped Schottky diode nonlinear transmission lines for 480-fs, 3.5-V transients," *Appl. Phys. Lett.* **65**, 881 (1994).

39. J. S. Bostak, D. W. van der Weide, D. M. Bloom and B. A. Auld, "All-electronic terahertz spectroscopy system with terahertz free-space pulses," *J. Opt. Soc. Am. B*, **11**, 2561 (1994).

40. Y. Matsuoka, S. Yamahata, K. Kurishima, and H. Ito, "Ultrahigh-speed InP/InGaAs double-heterostructure bipolar transistors and analysis of their operation," *Jpn. J. Appl. Phys.*, **35**, 5646 (1996).

41. M. J. W. Rodwell, M. Urteaga, T. Mathew, D. Scott, D. Mensa, Q. Lee, J. Guthrie, Y. Betser, S. C. Martin, R. P. Smith, S. Jaganathan, S. Krishnan, S. I. Long, R. Pullela, B. Agarwal, U. Bhattacharya, L. Samoska, and M. Dahlstrom, "Submicron Scaling of HBTs," *IEEE Trans. Electron Devices*, **48**, 2606 (2001).

42. G. Kozlov and A. Volkov, "Coherent source submillimeter wave spectroscopy," in *Millimeter and Submillimeter Wave Spectroscopy of Solids,* G.Gruner (ed.), pp. 51-109 (Springer, Berlin, 1998).

43. H. Eisele, A. Rydberg and G. Haddad, "Recent advances in the performance of InP Gunn devices and GaAs TUNNETT diodes for the 100-300-GHz frequency range and above," *IEEE Trans. Microwave Theory Tech*, **48**, 626 (2000).

44. D. W. van der Weide, "Electronic sources and detectors for wideband sensing in the terahertz regime," in *Sensing with Terahertz Radiation,* D. M. Mittleman (ed.), pp. 317-337 (Springer, Berlin, 2003).

45. X. Orlos and F. Martin, "Analytical solitons in nonlinear transmission lines loaded with heterostructure barrier varactors," *J. Appl. Phys.*, **90**, 2595 (2001).

46. I. Mehdi, "THz local oscillator technology," in *Millimeter and Submillimeter Detectors for Astronomy II* ; J. Zmuidzinas, W.S. Holland, S. Withington, eds., *Proc. SPIE*, **5498**, 103 (2004).

47. D. W. van der Weide, J. Murakowski, and F. Keilmann, "Gas-absorption spectroscopy with electronic terahertz techniques," *IEEE Trans. Microwave Theory Tech*, **48**, 740 (2000).

48. A. Dobroiu, M. Yamashita, Y.N. Ohshima, Y. Morita, C. Otani, and K. Kawase, "Terahertz imaging system based on a backward-wave oscillator," *Appl. Opt.*, **43**, 5637 (2004).

49. T. W. Crowe, J. L. Hesler, R. M. Weikle and S. H. Jones, "GaAs devices and circuits for terahertz applications," *Infrared Physics and Technology*, **40,** 175 (1999).

50. A. V. Muravjov, E. W. Nelson, R. E. Peale, V. N. Shastin and C. J. Fredricksen, "Far-infrared p-Ge laser with variable length cavity," *Infrared Physics and Technology*, **44,** 75 (2003).

51. H. W. Hubers, S. G. Pavlov and V. N. Shastin, "Terahertz lasers based on germanium and silicon," *Semicond. Sci. Technol.*, **20**, S211 (2005).

52. R. Kohler, A. Tredicucci, F. Beltram, H. E. Beere, E. H. Linfield, A. G. Davies, D. A. Ritchie, R. C. Iotti and F. Rossi, "Terahertz semiconductor heterostructure laser," *Nature*, **417,** 156 (2002).

53. R. Kohler, A. Tredicucci, F. Beltram, H. E. Beere, E. H. Linfield, A. G. Davies, D. A. Ritchie, S. S. Dhillon and C. Sirtori, "High-performance continuous-wave operation of superlattice terahertz quantum-cascade lasers," *Appl. Phys. Lett.* **82**, 1518 (2003).

54. S. C. Zerbetto and E. C. C. Vasconcellos, "Far infrared laser lines produced by methanol and its isotopic species: A review," *Int. J. Infrared Millimeter Waves,* **15**, 889 (1994).

55. R. M. Lees, "Giant K doubling in the infrared spectrum of CH_3OH: A sensitive probe for CH_3-rock/CO stretch/OH-bend vibrational coupling,"*Phys. Rev. Lett.* **75,** 3645 (1995).

56. L. Mahler, A. Tredicucci, R. Köhler, F. Beltram, H. E. Beere, E.H. Linfield and D.A. Ritchie, "High-performance operation of single-mode terahertz quantum cascade lasers with metallic gratings," *Appl. Phys. Lett.* **87**, 181101 (2005).

57. B. B Hu, X. C. Zhang, D. H. Auston and P. R. Smith, "Free-space radiation from elctro-optic crystals," *Appl. Phys. Lett.*, **56**, 506 (1990).

58. P. Y. Han, G. C. Cho and X. C. Zhang, "Broadband mid-infrared THz pulse: measurement technique and applications," *J. Nonlinear Opt. Phys. Mater.*, **8**, 89 (1999).

59. J. Shan, A. Nahata and T. F. Heinz, "Terahertz time-domain spectroscopy based on nonlinear optics," *J. Nonlinear Opt. Phys. Mater.*, **11**, 31 (2002).

60. G. P. Williams,"Filling the THz gap high power sources and applications," *Rep. Prog. Phys.*, **69**, 301 (2006).

61. T. Y. Chang, T. J. Bridges and E. G. Burkhardt, "CW submillimeter laser action in optically pumped methyl fluoride, methyl alcohol and vinyl chloride gases," *Appl. Phys. Lett.*, **17**, 249 (1970).

62. F. R. Petersen, K. M. Evenson, D. A. Jennings, J. S. Wells, K Goto and J. J. Jimfinez, "Far infrared frequency synthesis with stabilized CO_2 lasers: Accurate measurements of the water vapor and methyl alcohol laser frequencies,"*IEEE J. Quant. Electron.*, **QE-11**, 838 (1975).

63. M. Usami, M. Yamashita, K. Fukushima, C. Otani and K. Kawase, "Terahertz wideband spectroscopic imaging based on two-dimensional electro-optic sampling technique," *Appl. Phys. Lett.* **86**, 141109 (2005).

64. T. R. Tsai, C. Y. Chen, C. L. Pan, R. P. Pan and X. C. Zhang, "Terahertz time-domain spectroscopy studies of the optical constants of the nematic liquid crystal 5CB," *Appl. Opt.*, **42**, 2372 (2003).

65. M. Hangyo, M. Tani and T. Nagashima, "Terahertz time-domain spectroscopy of solids: A review," *Int. J. Infrared Millimeter Waves*, **26**, 1661 (2005).

66. D. D. Nolte, "Semi-insulating semiconductor heterostructures: Optoelectronic properties and applications," *J. Appl. Phys.*, **85**, 6259 (1999).

67. W. A. Kiitt, W. Albrecht and H. Kurz, "Generation of Coherent Phonons in Condensed Media," *IEEE J. Quant Electron.*, **28**, 2434 (1992).

68. D. H. Auston, K. P. Cheung and P. R. Smith, " Picosecond photoconducting Hertzian dipole,"*Appl. Phys. Lett.*, **45**, 284 (1984).

69. P. R. Smith, D. H. Auston and M. C. Nuss, "Subpicosecond Photoconducting Dipole Antennas," *IEEE J. Quant Electron.*, **24**, 255 (1988).

70. A. P. Defonzo and C. R. Lutz, "Optoelectronic transmission and reception of ultrashort electrical pulses," *Appl. Phys. Lett.*, **51**, 212 (1987).

71. D. R. Dykaar, B. I. Greene, J. F. Federici, A. F. J. Levi, L. N. Pfeiffer and R. F. Kopf, "Log-periodic antennas for pulsed terahertz radiation," *Appl. Phys. Lett.*, **59**, 262 (1991).

72. Y. Cai, I. Brener, J. Lopata, J. Wynn, L. Pfeiffer and J. Federici, "Design and performance of singular electric field terahertz photoconducting antennas," *Appl. Phys. Lett.*, **71**, 2076 (1997).

73. R. Yano, H. Gotoh, Y. Hirayama, S. Miyashita, Y. Kadoya and T. Hattori, "Terahertz wave detection performance of photoconductive antennas: Role of antenna structure and gate pulse intensity," *J. Appl. Phys.*, **97**, 103103 (2005).

74. F. G. Sun, G. A. Wagoner and X. C. Zhang, "Measurement of free-space terahertz pulses via long-lifetime photoconductors," *Appl. Phys. Lett.*, **67**, 1656 (1995).

75. M. Schall and P. U. Jepsen, "Photoexcited GaAs surfaces studied by transient terahertz time-domain spectroscopy," *Opt. Lett.*, **25**, 13 (2000).

76. G. Zhao, R. N. Schouten, N. van der Valk, W. Th. Wenckebach and P. C. M. Planken, "Design and performance of a THz emission and detection setup based on a semi-insulating GaAs emitter," *Rev. Sci. Instrum.*, **73**, 1715 (2002).

77. J. Darmo, T. Muller, W. Parz, J. Kroll, G. Strasser and K. Unterrainer, "Few-cycle terahertz generation and spectroscopy of nanostructures," *Phil. Trans. R. Soc. Lond. A.*, **362**, 251 (2004).

78. X. C. Zhang, J. T. Darrow, B. B. Hu, D. H. Auston, M. T. Schmidt, P. Tham and E. S. Yang, "Optically induced electromagnetic radiation from semiconductor surfaces," *Appl. Phys. Lett.*, **56**, 2228 (1990).

79. T. Dekorsy, H. Auer, C. Waschke, H. J. Bakker, H. G. Roskos, H. Kurz, V. Wagner and P. Grosse, "Emission of Submillimeter Electromagnetic Waves by Coherent Phonons," *Phys. Rev. Lett.*, **74**, 738 (1995).

80. T. Dekorsy, H. Auer, H. J. Bakker, H. G. Roskos and H. Kurz, "THz electromagnetic emission by coherent infrared-active phonons,"*Phys. Rev.B*, **53**, 4005 (1996).

81. E. R. Brown, F. W. Smith and K. A. McIntosh, "Coherent millimeter-wave generation by heterodyne conversion in low-temperature-grown GaAs photoconductors," *J. Appl. Phys.*, **73**, 3, 1480 (1993).

82. S. Verghese, K. A. McIntosh, S. Calawa, W. F. Dinatale, E. K. Duerr and K. A. Molvar, "Generation and detection of coherent terahertz waves using two photomixers," *Appl. Phys. Lett.*, **73**, 3824 (1998).

83. S. Hoffmann, M. Hofmann, E. Brundermann, M. Havenith, M. Matus, J. V. Moloney, A. S. Moskalenko, M. Kira, S. W. Koch, S. Saito and K. Sakai, "Four-wave mixing and direct terahertz emission with two-color semiconductor lasers," *Appl. Phys. Lett.*, **84**, 3585 (2004).

84. K. Kawase, Y. Ogawa and Y. Watanabe, "Non-destructive terahertz imaging of illicit drugs using spectral fingerprints," *Opt. Exp.*, **11**, 2549 (2003).

85. K. Suto and J. Nishizawa, "Widely frequency-tunable terahertz wave generation and spectroscopic application," *Int. J. Infrared Millimeter Waves,* **26**, 937 (2005).

86. S. Verghese, K. A. McIntosh, and E. R. Brown, "Optical and terahertz power limits in the low-temperature-grown GaAs photomixers," *Appl. Phys. Lett.,* **71**, 2743 (1997).

87. T. Pfeifer, H. M. Heiliger, H. G. Roskos and H. Kurz, "Generation and detection of picosecond electric pulses with freely positionable photoconductive probes," *IEEE Trans. Microwave Theory Tech*, **43**, 2856 (1995).

88. A. Nahata, D. H. Auston, T. F. Heinz and C. Wu, "Coherent detection of freely propagating terahertz radiation by electro-optic sampling," *Appl. Phys. Lett.*, **68,** 150 (1996).

89. I. S. Gregory, W. R. Tribea, M. J. Evans, T. D. Drysdale, D. R. S. Cumming and M. Missous, "Multi-channel homodyne detection of continuous-wave terahertz radiation," *Appl. Phys. Lett.*, **87**, 034106 (2005).

90. P. L. Richards, "Bolometers for infrared and millimeter waves," *J. Appl. Phys.*, **76**, 1 (1994).

91. E. Sano and T. Shibata, "Mechanism of subpicosecond electrical pulse generation by asymmetric excitation," *Appl. Phys. Lett.*, **55**, 2748 (1989).

92. J. A. Valdmanis and G. Mourou, "Subpicosecond electrooptic sampling: principles and applications," *IEEE J. Quant Electron.*, **22**, 69 (1986).

93. Y. Cai, I. Brener, J. Lopata, J. Wynn, L. Pfeiffer, J. B. Stark, Q. Wu, X. C. Zhang, J. F. Federici, "Coherent terahertz radiation detection: Direct comparison between free-space electro-optic sampling and antenna detection," *Appl. Phys. Lett.*, **73**, 444 (1998).

94. S. G. Park, M. R. Melloch and A. M. Weiner, "Comparison of terahertz waveforms measured by electro-optic and photoconductive sampling," *Appl. Phys. Lett.*, **73**, 3184 (1998).

95. S. Kono, M. Tani, P. Gu and K. Sakai, "Detection of up to 20 THz with a low-temperature-grown GaAs photoconductive antenna gated with 15 fs light pulses," *Appl. Phys. Lett.*, **77**, 4104 (2000).

96. Y. C. Shen, P. C. Upadhya, H. E. Beere, E. H. Linfield, A. G. Davies, I. S. Gregory, C. Baker, W. R. Tribe and M. J. Evans, "Generation and detection of ultrabroadband terahertz radiation using photoconductive emitters and receivers, *Appl. Phys. Lett.*, **85**, 164 (2004).

97. K. A. McIntosh, E. R. Brown, K. B. Nichols, O. B. McMahon, W. F. Di-Natale and T. M. Lyszczarz, "Terahertz photomixing with diode lasers in low-temperature-grown GaAs," *Appl. Phys. Lett.*, **67**, 3844 (1995).

98. S. Verghese, K. A. McIntosh and E. R. Brown, "Highly tunable fiber-coupled photomixers with coherent terahetz output power," *IEEE Trans. Microwave Theory Tech.*, **45**, 1301 (1997).

99. I. S. Gregory, C. Baker,W. R. Tribe, I. V. Bradley, M. J. Evans, E. H. Linfield, A. G. Davies, and M. Missous, "Optimization of Photomixers and Antennas for Continuous-Wave Terahertz Emission," *IEEE J. Quantum Elec.*, **41**, 717 (2005).

100. S. M. Duffy, S. Verghese and K. A. McIntosh, "Photomixers for Continuous-Wave Terahertz Radiation", in *Sensing with Terahertz Radiation*, D. M. Mittleman (ed.), (Springer, Berlin, 2003).

101. M. Tani, P. Gu, M. Hyodo, K. Sakai and T. Hidaka, "Generation of coherent terahertz radiation by photomixing of dual-mode lasers," *Optical and Quantum Electronics*, **32**, 503 (2000).

102. E. R. Brown, "THz generation by photomixing in ultrafast photoconductors," *International Journal of High Speed Electronics and Systems*, **13**, 497 (2003).

103. S. Verghese, K. A. McIntosh, S. Calawa, W. F. Dinatale, E. K. Duerr and K. A. Molvar, "Generation and detection of coherent terahertz waves using two photomixers," *Appl. Phys. Lett.*, **73**, 3824 (1998).

104. K. J. Siebert, H. Quast, R. Leonhardt, T. Loffler, M. Thomson, T. Bauer, H. G. Roskos and S. Czasch, "Continuous-wave all-optoelectronic terahertz imaging," *Appl. Phys. Lett.*, **80**, 3003 (2002).

105. T. Kleine-Ostmann, P. Knobloch, M. Koch, S. Hoffman, M. Breede, M. Hofmann, G. Hain, K. Pierz, M. Sperling, and K. Donhuijsen, "Continuous-wave THz imaging", *Electron. Lett.*, **37**, 1461 (2001).

106. C. F. Bohren and D. R. Huffman, *Absorption and Scattering of Light by Small Particles* (Wiley, New York, 1983).

107. D. Bhanti, S. Manickavasagam, and M. P. Mengüç, "Identification of non-homogeneous spherical particles from their scattering matrix elements," *J. Quant. Spectrosc. Radiat. Transf.*, **56**, 591 (1996).

108. X. H. Wu, A. Yamilov, H. Noh, H. Cao, E. W. Seelig and R. P. H. Chang, "Random lasing in closely packed resonant scatterers," *J. Opt. Soc. Am. B*, **21**, 159 (2004).

109. F. Borghese, P. Denti, G. Toscano and O. I. Sindoni, "Electromagnetic scattering by a cluster of spheres," *Appl. Opt.*, **18,** 116 (1979).

110. Y. L. Xu, "Electromagnetic scattering by an aggregate of spheres: far field," *Appl Opt.*, **36**, 9496 (1997).

111. L. Kai and P. Massoli, "Scattering of electromagnetic-plane waves by radially inhomogeneous spheres: a finely stratified sphere model," *Appl. Opt.*, **33,** 501 (1994).

112. T. Wriedt and U. Comberg, "Comparison of computational scattering methods," *J. Quant. Spectrosc. Radiat. Transfer*, **60**, 411 (1998).

113. J. C. Auger, B. Stout and V. Martinez, "Scattering efficiency of aggregated clusters of spheres: dependence on configuration and composition," *J. Opt. Soc. Am. A*, **22**, 2700 (2005).

114. H. C. van de Hulst, *Light Scattering by Small Particles* (Dover, New York, 1981).

115. M. Walther, PhD Thesis, "Modern Spectroscopy on Biological Molecules", Albert-Ludwigs Universitat Freiburg, Germany (2003).

116. Terahertz Lenses: Transmission spectra of Polyethylene, Microtech Instruments, Inc. Retrieved February 26, 2006 from the World Wide Web: http://www.mtinstruments.com./thzlenses/index.htm

117. P. H. Siegel, "Terahertz Technology in Biology and Medicine," *IEEE Trans. Microwave Theory Tech*, **52**, 2438 (2004).

118. P. F. Taday, "Applications of terahertz spectroscopy to pharmaceutical sciences," *Phil. Trans. R. Soc. Lond. A.*, **362**, 351 (2004).

119. D. J. Cook, B. K. Decker, G. Maislin and M. G. Allen, "Through Container THz Sensing: Applications for Explosives Screening," in *Terahertz and Gigahertz Electronics and Photonics III*, R. Jennifer Hwu (ed), *Proc. SPIE*, **5354**, pp. 55-62 (2004).

120. A. Sengupta, H. Altan, A. Bandyopadhyay, J. F. Federici, H. Grebel and D. Pham, "Investigation of Defect States of HfO_2 and SiO_2 on p type Silicon using THz Spectroscopy," **FWF1**, *89th OSA Annual Meeting, Tucson, AZ* (2005).

121. C. Kittel, *Solid State Physics*, (John Wiley and Sons, New York, 1998).

122. M. Hangyo, M. Tani and T. Nagashima, "Terahertz time-domain spectroscopy of solids: A review," *Int. J. Infrared Millimeter Waves*, **26**, 1661 (2005).

123. M. Herrmann, M. Tani, M. Watanabe and K. Sakai, "Terahertz imaging of objects in powders," *IEE Proc. Optoelectron.*, **149**, 116 (2002).

124. M. R. Kutteruf, C. M. Brown, L. K. Iwaki, M. B. Campbell, T. M. Korter and E. J. Heilweil, " Terahertz spectroscopy of short chain polypeptides", *Chem. Phys. Lett.*, **375**, 337 (2003).

125. B. Ferguson, S. Wang, H. Zhong, D. Abbott and X. C. Zhang, "Powder detection with T-ray imaging," in *Terahertz for Military and Security Applications,* R. Jennifer Hwu (ed), *Proc. SPIE,* **5070**, 7 (2003).

126. T. L. J. Chan, J. E. Bjarnason, A. W. M. Lee, M. A. Celis and E. R. Brown, "Attenuation contrast between biomolecular and inorganic materials at terahertz frequencies," *Appl. Phys. Lett.*, **85**, 2523 (2004).

127. P. C. Upadhya, Y. C. Shen, A. G. Davies and E. H. Linfield, "Far-infrared vibrational modes of polycrystalline saccharides," *Vibrational Spectroscopy*, **35**, 139 (2004).

128. H. S. Chua, J. Obradovic, A. D. Haigh, P. C. Upadhya, O. Hirsch, D. Crawley, A. A. P. Gibson, L. F. Gladden and E. H. Linfield, "Terahertz Time-Domain Spectroscopy of Crushed Wheat Grain," *IEEE Joint 29th International Conference on Infrared and Millimeter Waves, and 12th International Conference on Terahertz Electronics, 29th IRMMW-2004/12th THz-2004, Germany*, 399 (2004).

129. A. Sengupta, A. Bandyopadhyay, R. B. Barat, D. E. Gary and J. F. Federici, "Study of morphological effects on terahertz spectra using ammonium nitrate in *Optical Terahertz Science and Technology Topical Meeting, Florida, United States on CD ROM* (The Optical Society of America, Washington D.C. 2005) **ME6.**

130. T. M. Korter, R. Balu, M. B. Campbell, M. C. Beard, S. K. Gregurick and E. J. Heilweil, "Terahertz spectroscopy of solid serine and cysteine," *Chem. Phys. Lett.*, **418**, 65 (2006).

131. J. Pearce and D. M. Mittleman, "Using terahertz pulses to study light scattering," *Physica B,* **338**, 92(2003).

132. Z. Jian, J. Pearce and D. M. Mittleman, "Characterizing Individual Scattering Events by Measuring the Amplitude and Phase of the Electric Field Diffusing through a Random Medium," *Phys. Rev. Lett.*, **91**, 039903 (2003).

133. S. Mujumdar, K. J. Chau, and A. Y. Elezzabi, "Experimental and numerical investigation of terahertz transmission through strongly scattering sub-wavelength size spheres," *Appl. Phys. Lett.*, **85**, 6284 (2004).

134. J. F. Federici, B. Schulkin, F. Huang, D. E. Gary, R. B. Barat, F. Oliviera and D. Zimdars, "THz Imaging and Sensing for security applications," *Semiconductor Science and Technology*, **20**, S266 (2005).

135. A. Sengupta, PhD Dissertation, "Characterization of novel materials using terahertz spectroscopic techniques," New Jersey Institute of Technology, USA (2006).

136. D. J. Cook, B. K. Decker, and M. G. Allen, in *Optical Terahertz Science and Technology Topical Meeting, Florida, United States on CD ROM* (The Optical Society of America, Washington D.C. 2005) **MA6.**

137. W. J. Wiscombe, "Improved Mie scattering algorithms," *Appl. Opt.*, **19,** 1505 (1980).

138. V. E. Cachorro and L. L. Salcedo, "New improvements for Mie scattering calculations," *J. Electromagn. Waves. Appl.*, **5,** 913 (1991).

139. H. Du, "Mie-scattering calculation," *Appl. Opt.*, **43,** 1951 (2004).

140. M. Abramowitz, and I. A. Stegun, Handbook of Mathematical Functions, with Formulas, Graphs and Mathematical Tables, (Dover Publications, New York, 1974).

141. M. A. Jarzembski, M. L. Norman, K. A. Fuller, V. Srivastava and D. R. Cutten, "Complex refractive index of ammonium nitrate in the 2-20μm spectral range," *Appl. Opt.* **42,** 922 (2003).

142. C. Dodson, M. J. Fitch, R. Osiander and J. B. Spicer, "Terahertz imaging for anti-personnel mine detection," in *Terahertz for Military and Security Applications III*, R. Jennifer Hwu, (ed), *Proc. SPIE,* **5790**, 85 (2005).

143. D. H. Auston and M. C. Nuss. "Electro-optic generation and detection of femtosecond electrical transients," *IEEE J. Quant. Electron.,* **24**, 255 (1988).

144. G. Gallot, S. P. Jamison, R. W. McGowan and D. Grischkowsky, "Terahertz waveguides." *J. Opt. Soc. Am. B*, **17**, 851 (2000).

145. J. A. Harrington, *Integrated Fibers and Their Applications,* (SPIE Press, Washington, 2004).

146. V. F. Kokorina, "*Glasses for Infrared Optics*" CRC Press, Boca Raton (1996).

147. J. S. Sanghera and I. D. Aggarwal, *Infrared Fiber Optics*, CRC Press, Boca Raton (1998).

148. K. Ohsawa, T. Shibata, K. Nakamura, and M. Kimura, "Light scattering in Fluorozirconate Glasses," *Proc. 1st Intern. Symp. on Halide Glasses,* Cambridge,U.K., 1982.

149. S. Zembutsu and S. Fukunishi, "Waveguiding properties of (Se,S)-based chalcogenide glass films and some applications to optical waveguide devices," *Appl. Opt.*, **18**, 393 (1979).

150. Y. Mimura and C. Ota, "Transmission of CO_2 laser power by single-crystal CsBr fibers," *Appl. Phys. Lett.*, **40**, 773 (1982).

151. D. A. Pinnow, A. L. Gentile, A. G. Standlee, A. J. Timper and L. M. Hobrock, "Polycrystalline fiber optical waveguides for infrared transmission," *Appl. Phys. Lett.*, **33**, 28 (1978).

152. E. Garmire, T. McMahon and M. Bass, "Flexible infrared waveguides for high-power transmission," *IEEE J. Quantum Electron*, **16**, 23 (1980).

153. G. N. Merberg, "Current status of infrared fiber optics for medical laser power delivery," Lasers Surg. Med. **13,** 572 (1993).

154. B. Temelkuran, S. D. Hart, G. Benoit, J. D. Joannopoulos and Y. Fink, "Wavelength-scalable hollow optical fibers with large photonics bandgaps for CO_2 laser transmission." Nature, **420**, 650 (2002).

155. H. Han, H. Park, M. Cho and J. Kim, "Terahertz pulse propagation in a plastic photonic crystal fiber." Appl. Phys. Lett., **80**, 2634 (2002).

156. K. Wang and D. M. Mittleman, "Metal wires for terahertz wave guiding," Nature, **432**, 376 (2004).

157. J. A. Harrington, R. George, P. Pedersen and E. Mueller, "Hollow polycarbonate waveguides with inner Cu coatings for delivery of terahertz radiation." *Opt. Exp.* **12**, 5263 (2004).

158. C. M. Smith, N. Venkataraman, M. T. Gallagher, D. Muller, J. A. West, N. F. Borrelli, D. C. Allan and K. W. Koch, "Low-loss hollow-core silica/air photonic bandgap fibre," *Nature*, **424**, 657 (2003).

159. K. Saitoh and M. Koshiba, "Leakage loss and group velocity dispersion in air-core photonic bandgap fibers," *Opt. Exp.*, **11**, 3100 (2003).

160. H. Nishihara, T. Inoue and J. Koyama, "Low-loss parallel-plate waveguide at 10.6 μm," *Appl. Phys. Lett.*, **25**, 391 (1974).

161. A. J. Gatesman, R. H. Giles, and J. Waldman, "High-precision reflectometer for submillimeter wavelengths," *J. Opt. Soc. Am. B.* **12,** 212 (1995).

162. R. George and J. A. Harrington, "New coatings for metal-dielectric hollow waveguides" in *Optical Fibers and Sensors for Medical Applications II*, I. Gannot, ed., *Proc. SPIE*, **4616**, 129 (2002).

163. E. A .J. Marcatili and R.A. Schmeltzer, "Hollow metallic and dielectric waveguides for long distance optical transmission and lasers," *Bell Syst. Tech. J.*, **43**, 1783 (1964).

164. M. Miyagi, A. Hongo and S. Kawakami, "Transmission Characteristics of Dielectric-Coated Metallic Waveguide for Infrared Transmission: Slab Waveguide Model," *IEEE J. Quant. Electron.*, **QE-19**, 136 (1983).

165. A. Hongo, K. I. Morosawa, T. Shiota, Y. Matsuura and M. Miyagi, "Transmission Characteristics of Germanium Thin-Film-Coated Metallic Hollow Waveguides for High-powered CO_2 Laser Light," *IEEE J. Quant. Electron.*, **26**, 1510 (1990).

166. J. A. Stratton, *Electromagnetic Theory*, (McGraw Hill Book Company, New York 1941).

167. A. Ghatak and K. Thyagarajan, *An Introduction to Fiber Optics* (Cambridge University Press, Cambridge, 1999).

168. M. A. Ordal, L. L. Long, R. J. Bell, S. E. Bell, R. R. Bell, R. W. Alexander, Jr. and C. A. Ward, "Optical properties of the metals Al, Co, Cu, Au, Fe, Pb, Ni, Pd, Pt, Ag, Ti, and W in the infrared and far infrared," *Appl. Opt.*, **22**, 1099 (1983).

169. M. A. Ordal, R. J. Bell, R. W. Alexander, Jr., L. L. Long and M. R. Querry, "Optical properties of fourteen metals in the infrared and far infrared: Al, Co, Cu, Au, Fe, Pb, Mo, Ni, Pd, Pt, Ag, Ti, V, and W," *Appl. Opt.*, **24**, 4493 (1985).

170. C. L. Nagendra and J. L. Lamb, "Optical properties of semiconductor-metal composite thin films in the infrared region," *Appl. Opt.*, **34**, 3702 (1995).

171. D. Qu, D. Grischkowsky and W. Zhang, "Terahertz transmission properties of thin, subwavelength metallic hole arrays," *Opt. Lett.*, **29**, 896 (2004).

172. J. Cunningham, C. Wood, A. G. Davies, C. K. Tiang, P. Tosch, D. A. Evans, E. H. Linfield, I. C. Hunter and M. Missous, "Multiple-frequency terahertz pulsed sensing of dielectric films," *Appl. Phys. Lett.*, **88**, 071112 (2006).

173. I. S. Gregory, W. R. Tribe, M. J. Evans, T. D. Drysdale, D. R. S. Cumming and M. Missous, "Multi-channel homodyne detection of continuous-wave terahertz radiation," *Appl. Phys. Lett.*, **87**, 034106 (2005).

174. S. R. Keiding and D. Grischkowsky, "Measurements of the phase shift and reshaping of terahertz pulses due to total internal reflection," *Opt. Lett.*, **15**, 48 (1990).

175. R. Kersting, G. Strasser and K. Unterrainer, "Terahertz phase modulator," *Electron. Lett.*, **36**, 1156 (2000).

176. C. Y. Chen, C. F. Hsieh, Y. F. Lin, R. P. Pan and C. L. Pan, "Magnetically tunable room-temperature 2π liquid crystal terahertz phase shifter," *Opt. Exp.*, **12**, 2630 (2004).

177. J. M. Lourtioz, A. de Lustrac, F. Gadot, S. Rowson, A. Chelnokov, T. Brillat, A. Ammouche, J. Danglot, O. Vanbesien and D. Lippens, "Toward Controllable Photonic Crystals for Centimeter- and Millimeter-Wave Devices," *J. Lightwave Tech.*, **17**, 2025 (1999).

178. J. W. Lee, M. A. Seo, D. J. Park, D. S. Kim, S. C. Jeoung, C. Lienau and Q. H. Park, "Shape resonance omni-directional terahertz filters with near-unity transmittance," *Opt. Exp.*, **14**, 1253 (2006).

179. M. E. MacDonald, A. Alexanian, R. A. York, Z. Popovic and E. N. Grossman, "Spectral Transmittance of Lossy Printed Resonant-Grid Terahertz Bandpass Filters," IEEE Trans. Microwave Theory Tech, 48, 712 (2000).

180. H. A. Smith, M. Rebbert and O. Sternberg, "Designer infrared filters using stacked metal lattices," *Appl. Phys. Lett.*, **82**, 3605 (2003).

181. D. Wu, N. Fang, Cheng Sun, X. Zhang, W. J. Padilla, D. N. Basov, D. R. Smith and S. Schultz, "Terahertz plasmonic high pass filter," *Appl. Phys. Lett.*, **83**, 201 (2003).

182. J. W. Lee, M. A. Seo, J. Y. Sohn, Y. H. Ahn, D. S. Kim, S. C. Jeoung, C. Lienau and Q. H. Park, "Invisible plasmonic meta-materials through impedance matching to vacuum," *Opt. Exp.*, **13**, 10681 (2005).

183. I. H. Libon, S. Baumgartner, M. Hempel, N. E. Hecker, J. Feldmann, M. Koch and P. Dawson, "An optically controllable terahertz filter," *Appl. Phys. Lett.*, **76**, 2821 (2000).

184. T. Kleine-Ostmann, M. Koch and P. Dawson, "Modulation of THz radiation by semiconductor nanostructures", *Micro. Opt. Tech. Lett.*, **35**, 343 (2002).

185. B. Temelkuran, M. Bayindir, E. Ozbay, J. P. Kavanaugh, M. M. Sigalas and G. Tuttle, "Quasimetallic silicon micromachined photonic crystals," *Appl. Phys. Lett.*, **78**, 264 (2001).

186. T. D. Drysdale, R. J. Blaikie, D. R. S. Cumming, "Calculated and measured transmittance of a tunable metallic photonic crystal filter for terahertz frequencies," *Appl. Phys. Lett.*, **83**, 5362 (2003).

187. H. Nemec, L. Duvillaret, F. Garet, P. Kuzel, P. Xavier, J. Richard and D. Rauly, "Thermally tunable filter for terahertz range based on a one-dimensional photonic crystal with a defect," *Appl. Phys. Lett.*, **96**, 4072 (2004).

188. H. Nemec, P. Kuzel, L. Duvillaret, A. Pashkin, M. Dressel, M. T. Sebastian, "Highly tunable photonic crystal filter for the terahertz range," *Opt. Lett.*, **30**, 549 (2005).

189. C.Winnewisser, F. T. Lewen, M. Schall, M. Walther and H. Helm, "Characterization and Application of Dichroic Filters in the 0.1–3-THz Region," *IEEE Trans. Microwave Theory Tech*, **48**, 744 (2000).

190. J. Cunningham, C. Wood, A. G. Davies, I. Hunter, E. H. Linfield and H. E. Beere, "Terahertz frequency range band-stop filters," *Appl. Phys. Lett.*, **86**, 213503 (2005).

191. C. Y. Chen, C. L. Pana, C. F. Hsieh, Y. F. Lin and R. P. Pan, "Liquid-crystal-based terahertz tunable Lyot filter," *Appl. Phys. Lett.*, **88**, 101107 (2006).

192. D. R. Smith, J. B. Pendry and M. C. K. Wiltshire, "Metamaterials and Negative Refractive Index," *Science,* **305**, 788 (2004).

193. S. Zhang, W. Fan, N. C. Panoiu, K. J. Malloy, R. M. Osgood and S. R. J. Brueck, "Experimental demonstration of near-infrared negative-index metamaterials," *Phys. Rev. Lett.*, **95**, 137404 (2005).

194. W. J. Padilla, D. R. Smith and D. N. Basov, "Spectroscopy of metamaterials from infrared to optical frequencies," *J. Opt. Soc. Am. B*, **23**, 404 (2006).

195. Davies C.C., "*Lasers and Electro-Optics*," Cambridge University Press, Cambridge, UK (1996).

196. Ramo S., Whinnery J.R. and Van Duzer R., "*Fields and Waves in Communication Electronics*," (Wiley, New York, NY 1993).

197. M. Born and E. Wolf, "*Principles of Optics,*" (Cambridge University Press, London UK, 1999).

198. Karl D. Moeller, personal communication dated March 22, 2006.

199. A. Bandyopadhyay, A. Stepanov, B. Schulkin, M Federici, A. Sengupta, D. Gary, J. Federici, R. Barat, Z. H. Michalopoulou, D. Zimders, "Terahertz interferometric and synthetic aperture imaging," *J. Opt. Soc. Am. A* (in press).

200. D. J Cook, B. K. Decker, G. Maislin, & M. G. Allen, "Through container THz sensing: applications for explosives screening," in *Terahertz and Gigahertz Electronics and Photonics III*, R. J. Hwu, eds., Proc. SPIE., **5354**, 55 (2004).

201. K. Kawase, Y. Ogawa & Y. Watanabe, "Non-destructive terahertz imaging of illicit drugs using spectral fingerprints," *Opt. Exp.*, **11,** 2549 (2003).

202. D. A. Zimdars & J.S. White, "Terahertz reflection imaging for package and personnel inspection," in *Terahertz for Military and Security Applications II*, R. J. Hwu & D. L. Woolard, eds., *Proc. SPIE.*, **5411**, 78 (2004).

203. W. R. Tribe, D. A. Newnham, P. F. Taday & M. C. Kemp, "Hidden object detection: Security applications of terahertz technology," in *Terahertz and Gigahertz Electronics and Photonics III*, R. J. Hwu, ed., *Proc. SPIE,* **5354**, 44 (2004).

204. Y. C. Shen, P. F. Taday & M. C. Kemp, "Terahertz spectroscopy of explosive materials," in *Passive Millimetre-Wave and Terahertz Imaging and Technology;* R. Appleby, J. M. Chamberlain, K. A. Krapels; eds. *Proc. SPIE,* **5619**, 82 (2004).

205. M. C. Kemp, P. F. Taday, B. E. Cole, J. A. Cluff, A. J. Fitzgerald & W. R. Tribe, " Security applications of terahertz technology," in *Terahertz for Military and Security Applications*, R. J. Hwu & D. L. Woolard, eds., *Proc. SPIE.* **5070**, 44 (2003).

206. M. K. Choi, A. Bettermann, & D. W. Van der Wiede, "Potential for detection of explosive and biological hazards with electronic terahertz systems" *Phil. Trans. R. Soc. Lond. A*, **362**, 337 (2004).

207. D. M. Mittleman, M. Gupta, R. Neelamani, R. G. Baraniuk, J. V. Rudd & M. Koch, "Recent advances in terahertz imaging," *Appl. Phys. B.*, **68**, 1085 (1999).

208. A. R. Thompson, J. M. Moran & G. W. Swenson, "*Interferometry and Synthesis in Radio Astronomy, 2nd ed.*," (Wiley Interscience, New York, 2001).

209. J. Federici, D. Gary, B. Schulkin, F. Huang, H. Altan, R. Barat & D. Zimdars, " Terahertz imaging using an interferometric array. Appl. Phys. Let., **83**, 2477 (2003).

210. K. P. Walsh, B. Schulkin, D. Gary, J. F. Federici, R. Barat & D. Zimdars, "Terahertz near-field interferometric and synthetic aperture imaging," in *Terahertz for Military and Security Applications*, R. J. Hwu & D. L. Woolard, eds., *Proc. SPIE.* **5411**, 9 (2004).

211. A. Bandyopadhyay, A. M. Sinyukov, A. Sengupta, R. B. Barat, D. E. Gary, Z. H. Michalopoulou & J. F. Federici, "Interferometric terahertz imaging for detection of lethal agents using artificial neural network analyses," in *Proc. IEEE Sarnoff Symposium 2006* (in press).

212. A. Sengupta, A. Bandyopadhyay, R. B. Barat, D. E. Gary & J. F. Federici, " THz reflection spectroscopy of Composition C 4 and its detection through interferometric imaging," in *THz and GHz Electronics and Photonics V,* R. J. Hwu ed., *Proc. SPIE.,* **6120,** 61200A, 2006.

213. K. Yamamoto, M. Yamaguchi, F. Miyamaru, M. Tani, M. Hangyo, T. Ikeda, A. Matsushita, K. Koide, M. Tatsuno, and Y. Minami, "Noninvasive inspection of C-4 explosive in mails by terahertz time-domain spectroscopy", *Jpn. J. Appl. Phys.,* **43**, L414 (2004).

214. H. B. Liu, Y. Chen, G. J. Bastiaans, and X. C. Zhang, "Detection and identification of explosive RDX by THz diffuse reflection spectroscopy", *Opt. Exp.*, **14**, 415 (2006).

215. J. C. Principe, N. R. Euliano & W. C. Lefebvre, "*Neural and Adaptive Systems*," (John Wiley & Sons, New York, 2000).

216. F. Kozato & G. A. Ringwood, "How slow processes can think fast in concurrent logic," in *Fast Learning and Invariant Object Recognition: The Sixth-Generation Breakthrough*, B. Soucek & the Iris Group, eds. (John Wiley & Sons, New York, 1992), pp. 47-60.

217. B. Widrow, D. E. Rumelhart & M. A. Lehr, "Neural Networks: Applications in industry, business and science," *Communication of the ACM*, **37**, 93 (1994)

218. P. M. Shea & V. Lin, "Detection of explosives in checked airline baggage using an artificial neural system," in *Proceedings of IEEE International Joint Conference on Neural Networks* (Institute of Electrical and Electronics Engineers, New York, 1989), pp. 31-34.

219. K. Fukunaga, "*Introduction to Statistical Pattern Recognition*," (Academic Press, San Diego, 1990)

220. G. J. McLachlan, "Discriminant Analysis and Statistical Pattern Recognition," (John Wiley & Sons, New York, 2004)

221. J. E. Dayhoff. Neural Network Architectures: An Introduction (Van Norstrand Reinhold, New York, 1990)

222. C. T. Leondes, eds. Image Processing and Pattern Recognition (Academic Press, San Diego, 1998)

223. The MathWorks, Inc. http://www.mathworks.com

224. The NeuroDimension, Inc. http://www.nd.com

225. G. J. Awcock & R. Thomas, "*Applied Image Processing*," (McGraw-Hill Inc., New York, 1996)

226. T. Kohonen, G. Bama, and R. Chrisley, "Statistical Pattern Recognition with Neural Networks: Benchmarking Studies," *Proc. IEEE International Conference on Neural Networks*, **1**, 1 (1988).

227. J. Kangas, T. Kohonen, J. Laaksonen, O. Simula and O. Venta, "Variants of self-organizing maps," *Proc. IEEE International Joint Conference on Neural Networks*, **2**, 517 (1989).

228. D. J Cook, B. K. Decker, G. Dadusc, & M. G. Allen, "Through-container THz sensing: applications for biodetection," in Chemical and Biological Standoff Detection, J.O. Jensen and J.M. Theriault, eds., *Proc. SPIE*,. **5628**, 36 (2003).